Parametric Amplification in Spinor Bose-Einstein Condensates

Von der Fakultät für Mathematik und Physik
der Gottfried Wilhelm Leibniz Universität Hannover
zur Erlangung des Grades

Doktor der Naturwissenschaften
- Dr. rer. nat. -

genehmigte Dissertation von

M. Sc. Gebremedhn Gebreyesus Hagoss

geboren am 30. Dezember 1975 in Adigrat, Äthiopien

Institut für Theoretische Physik
Gottfried Wilhelm Leibniz Universität Hannover

2010

Zusammenfassung

Die ersten Experimente mit atomaren Bose-Einstein Kondensaten (BEK) wurden in magnetischen Fallen durchgeführt. Das Magnetfeld dieser Fallen führt zu einer Polarisierung der atomaren Spins und somit zu einem Einfrieren des Spinfreiheitsgrades. Optische Dipolfallen erlauben hingegen beliebige Spinorientierungen. Der Spinfreiheitsgrad von quantenentarteten Spinorgasen führt zu unzähligen neuen physikalischen Phänomenen. Das Hauptmerkmal von ultrakalten Spinorgasen sind spinändernde Zweiteilchenstöße, bei denen sich die z-Komponente der Einteilchenspins ändert, während die z-Komponente des Zweiteilchenspins erhalten bleibt. Das Wechselspiel dieser spinändernden Stöße mit dem Zeemaneffekt und dem inhomogenen Fallenpotential führt zu einer Reihe neuartiger Phänomene im Hinblick auf die Struktur des Grundzustandes, der Ausbildung von Spinstrukturen und Domänenwänden, sowie der kohärenten Spindynamik. Erst kürzlich wurde gezeigt, dass Spinor BEK die Beobachtung makroskopischer Quantenphänomene erlauben, welche der aus der Quantenoptik bekannten parametrischen Verstärkung sehr ähnlich sind. Die Untersuchung dieses Effekts ist der Schwerpunkt dieser Arbeit.

In dieser Dissertation wird die Spindynamik von atomaren ^{87}Rb BEK mit Spin 1 oder 2 untersucht, welche im Spin-Anfangszustand $|m = 0\rangle$ präpariert wurden. Ein charakteristisches Merkmal der Dynamik ist die stoßinduzierte Erzeugung korrelierter Atompaare in den Spin-Zuständen $|m = \pm 1\rangle$. Dieser Prozess ist auf das Engste mit der parametrischen Verstärkung verwandt, welche aus der Quantenoptik bekannt ist. Ich zeige, dass die Spindynamik eine faszinierende multiresonante Magnetfeldabhängigkeit aufweist, welche durch die Inhomogenität der Falle induziert wird. Diese Magnetfeldabhängigkeit ist direkt verknüpft mit der Instabilität der Spin-Bogoliubov-Moden des BEK im Spin-Anfangszustand $|m = 0\rangle$. Die genaue Analyse der Magnetfeldabhängigkeit der Instabilität der Spin-Bogoliubov-Moden zeigt, dass das optische Fallenpotential einen entscheidenden Einfluss auf die Effizienz der Paarerzeugung hat. Ich untersuche außerdem im Detail den Auslösemechanismus der Spindynamik, welcher durch die unvermeidbare Präsenz störender Saatatome und durch Quantenfluktuationen gegeben ist. Es lässt sich aber zeigen, dass der Einfluss von Saatatomen auf das System unter bestimmten Bedingungen vernachlässigbar ist, wodurch die Dynamik ausschließlich durch Quantenfluktuationen ausgelöst wird.

Es wird weiterhin gezeigt, dass magnetische Dipol-Dipol-Wechselwirkungen einen entscheidenden Einfluss auf die Dynamik von Spin-1 ^{87}Rb BEK haben, obwohl diese in Alkaligasen typischerweise sehr schwach sind. Allerdings ist die Stärke der spinändernden Stöße in Spin-1 ^{87}Rb ebenfalls sehr schwach und dadurch von vergleichbarer Größenordnung. Wir zeigen, dass magnetische Dipol-Dipol-Wechselwirkungen zu einer starken Abhängigkeit der Verstärkungsdynamik vom Winkel zwischen der Achse der zigarrenförmigen Falle und dem angelegten Magnetfeld führen. Wir

untersuchen außerdem den wichtigen Einfluss von Magnetfeldgradienten auf den Verstärkungsprozess, welcher von vergleichbarer Größenordnung sein kann. Für den zweifelsfreien Nachweis des Einflusses der magnetischen Dipol-Dipol-Wechselwirkung ist deshalb in zukünftigen Experimenten eine genaue Kontrolle der Magnetfeldgradienten unerlässlich.

Ich zeige schließlich, dass in einer axialsymmetrischen Falle sowohl die räumliche als auch die Spinsymmetrie des Hamiltonians während der parametrischen Verstärkung der Quantenfluktuationen spontan gebrochen sein kann. Die axiale Symmetrie ist immer dann gebrochen, wenn entartete Fallenmoden maximal verstärkt werden, während in diesen Fällen die Spinsymmetrie erhalten bleibt. Wenn hingegen Fallenmoden mit unterschiedlichen Energien gleich stark verstärkt werden, führt Quanteninterferenz zur Ausbildung räumlicher Spinstrukturen und somit zu einer spontanen Brechung der lokalen Magnetisierung.

Alle Ergebnisse dieser Dissertation werden mit den an der Leibniz Universität Hannover durchgeführten Experimenten verglichen.

Schlagwörter: Spinor Bose-Einstein Kondensation, Parametrische Verstärkung, Vakuumfluktuationen

Abstract

Early experiments on atomic Bose-Einstein condensates (BECs) were carried out in magnetic traps, where the atomic spin is polarized by external magnetic fields, and hence the atomic spin degree of freedom is frozen. However, the atoms get their spin degree of freedom back when they are trapped in an optical dipole traps. The liberated spin degree of freedom of ultracold atoms leads to a wealth of new physics in quantum degenerate spinor gases. The key feature of these gases are spin-changing collisions, which may change the z-component of the individual atomic spins while the total spin of the atomic pair is conserved during a collison. The competition between spin-dependent interatomic interactions, Zeeman effect, and inhomogeneous trapping induces a rich physics in these gaseous spinor condensates, both in what concerns their ground state properies, spin textures and domains formations and the coherent spin dynamics. More recently, spinor BECs have been shown to offer the fascinating possibility of studying macroscopic effects directly stemming from purely quantum phenomena like the ones resembling parametric amplification in quantum optics. The study of this effect constitutes the main focus of this Thesis.

In this thesis we analyze the spinor dynamics of ^{87}Rb spin-2 and spin-1 condensates initially prepared in the $|0\rangle$ Zeeman sublevel. We show that this dynamics, characterized by the creation of correlated atomic pairs into $|\pm 1\rangle$ states, which closely resembles parametric amplification in quantum optics, presents an intriguing multiresonant magnetic field dependence induced by the trap inhomogeneity. This dependence is directly linked to the most unstable Bogoliubov spin excitations of the initial $|0\rangle$ condensate, showing that, in general, even a qualitative understanding of the pair-creation efficiency in a spinor condensate requires a careful consideration of the confinement. We analyze also in detail the triggering mechanisms of this multi-resonant magnetic field dependent pair creation efficiency and show that under proper conditions the system is basically insensitive against spurious seeding, being purely driven by quantum spin fluctuations.

The magnetic dipole-dipole interactions, although typically very weak in alkaline atoms, are shown to play a very relevant role in the amplification dynamics of spin-1 ^{87}Rb due low energy scale of the spin changing interactions. We show that these interactions may lead to a strong dependence of the amplification dynamics on the angle between the trap axis and the magnetic field orientation. We analyze as well the important role played by magnetic fiel gradients, which modify also strongly the amplification process. Magnetic field gradients must be hence carefully controlled in future experiments, in order to observe clearly the effects of the dipolar interactions in the amplification dynamics.

We also show a twofold spontaneous breaking of spatial and $+1$ and -1 spin symmetries during the amplification of quantum spin fluctuations. When degenerate spin modes are maximally amplified, we show that the cylindrical spatial symmetry is spontaneously broken, but phase squeezing prevents spin-symmetry breaking. If, however, nondegenerate spin modes contribute to the amplification, quantum in-

terferences lead to spin-dependent density profiles and hence spontaneously formed patterns in the longitudinal magnetization.

Throughout the thesis we compare our results with the experimental ones performed at the Leibniz University of Hannover.

Keywords: Spinor Bose-Einstein Condensation, Parametric Amplification, Vacuum Fluctuations.

Contents

List of Figures

Introduction

Ultracold atoms have been one of the most active research areas in physics since more than two decades. In this time, the progress has been outstanding both experimentally and theoretically. New trapping and cooling techniques have been developed since the 1970s, which have resulted in the discovery of laser-based techniques like laser cooling and magneto-optical trapping [1, 2], leading in the mid 1990s to the experimental realization of the *Bose-Einstein condensation* (BEC) in alkaline gases. As a result of these remarkable developments, the community of ultracold gases has been awarded several Nobel prizes during the last few years [1].

One of the most fascinating features of the physics of ultracold atoms is given by its inherent cross-disciplinar character. A close link to condensed-matter physics and solid-state physics is provided by the physics of ultracold atoms in optical lattices and low-dimensional geometries, as highlighted by the milestone realization of the superfluid to Mott-insulator phase transition [3, 4] and the Tonks-Girardeau gas [5, 6]. The non-linearity originating in BECs as a consequence of the interparticle interactions provides an ideal platform for studying non-linear phenomena traditionally investigated in non-linear optics, as e.g. solitons [7–11]. Ultracold gases have also attracted the interest of other disparate areas of physics including quantum information and molecular physics.

Additionally, ultracold atoms provide interesting applications, in particular in what concerns precision measurements. Atom interferometry [12] has been employed for very precise measurements of the gravitational constant G, the gravitational acceleration g, the Planck constant h and the fine structure constant α [13–15]. Atomic gyroscopes based on the Sagnac effect [16] are particularly relevant for the study of the variations in the rotation of the Earth, general relativity effects [17], for navigation and even for oil exploration.

A major feature of the physics of ultracold atoms is provided by their internal structure, potentially much richer than that of e.g. electrons. The spin degree of freedom allows for the exceedingly rich physics of spinor gases, and more specifically of spinor condensates, part of which will be considered in this Thesis.

---

[1]Wolfgang Paul recieved the Nobel prize in 1989 for his studies on ion traps; Steven Chu, Claude Cohen-Tannoudji and William D. Phillips for their work on laser cooling in 1997; Eric A. Cornell, Wolfgang Ketterle and Carl E Wieman got the Nobel prize for the experiments on BEC in 2001

A spinor BEC is a condensate consisting of atoms with spin F, where F is the sum of electron and nuclear spin. Such a BEC has $2F + 1$ internal states $|F, m_F\rangle$ where $m_F = -F, ..., F$. In a magnetic field, the degeneracy of these components is lifted due to the Zeeman effect. Magneto-optical traps use this Zeeman splitting to prevent the laser cooled atoms from leaving the trap, but only certain Zeeman substates are trapped suppressing any spinor dynamics since the energy difference between two substates is too high for the atoms to change their m_F by scattering with other atoms. The first attempt to create a spinor BEC was performed in 1998 using a magnetic trap to confine simultaneously two Zeeman substates of different hyperfine spin states of rubidium, $|F = 1, m_F = -1\rangle$ and $|F = 2, m_F = 1\rangle$, which present exactly the same Zeeman shift [18].

The breakthrough for spinor condensates came however with the development of optical dipole traps, capable of confining simultaneously all spin components of a spin-F BEC. The first optically trapped spinor BEC, created in 1998, was a spin-1 sodium condensate [19]. Subsequently, spinor condensates of ^{87}Rb with spin-1 [20, 21] and with spin-2 [21–24] were created. Spin-3 condensates are potentially possible in Chromium experiments [25].

Spinor BECs have attracted as well an impressive amount of theoretical efforts, which have addressed a wealth of topics, including ground state properties [26–28], coherent spin mixing [29–34], spinor vortices [26, 35], spin textures and domains [36, 37], spin squeezing and entanglement [38, 39].

Spinor condensates offer as well the fascinating possibility of studying macroscopic (or at least mesoscopic) effects directly stemming from purely quantum phenomena. These effects, resembling parametric amplification in quantum optics, constitute the main focus of this Thesis.

1.1   Bose-Einstein Condensation

1.1.1   The realization of Bose-Einstein condensates

Bose-Einstein condensation was predicted by Albert Einstein in 1925 [40] using the photon-statistics developed by Satyendra Nath Bose [41]. This remarkable phenomenon consists in that below a critical temperature T_c a macroscopic number of bosons occupy the lowest single particle state with the rest distributed over excited states [42].

Condensation occurs when a collection of identical bosons is cooled down to a very low temperature, such that the corresponding thermal de Broglie wavelength of the particles ($\lambda_{db} = h/(2\pi m k_B T)^{1/2}$, with m the atom mass, k_B the Bolzmann constant, and T the temperature) becomes larger than the mean inter-particle separation (i.e. the particles overlap with each other). More precisely, condensation sets in when the dimensionless phase-space density,

$\rho_{ps} \equiv n\lambda_{db}^3$ is larger than 2.612, with $n = N/V$ the atom density.

Although condensation was known to be a fundamental phenomenon, connected to superfluidity in liquid Helium and superconductivity in metals, it was only experimentally observed for the first time in 1995 using magnetically trapped rubidium [43] and sodium [44] gases. Since then BEC has been realised in a variety of species including ^{7}Li [45], Hydrogen [46], ^{85}Rb [47], ^{41}K [48], ^{133}Cs [49], Chromium [25, 50], Calcium [51] [2], ^{84}Sr [52], ytterbium [53] and in molecules of ^{87}Rb$_2$ [54], ^{40}K$_2$ [55], ^{133}Cs$_2$ [56], ^{6}Li$_2$ [57, 58], and ^{23}Na$_2$ [59].

In addition to dilute quantum gases of ultracold atoms, condensation has been also observed in other system, including excitons [3] [60], microcavity exciton polaritons [4] [61, 62], and magnons [5] [63].

1.1.2 Order parameter

The concept of condensation may be defined in terms of the single-particle density matrix [64]

$$\rho^{(1)}(\vec{r}', \vec{r}, t) = \langle \hat{\Psi}^\dagger(\vec{r}', t)\hat{\Psi}(\vec{r}, t)\rangle, \tag{1.1}$$

where $\hat{\Psi}(\vec{r}, t)$ and $\hat{\Psi}^\dagger(\vec{r}, t)$ are the creation and annihilation scalar boson field operators for a particle at the position $\vec{r}$ and time t. When one of the eigenvalues of the density-matrix is macroscopic (i.e. of the order of the total number of particles N), while the sum of all other eigenvalues is of the order of 1, then this eigenvalue defines the number of particles N_0 in the BEC. On the contrary, BEC is absent when all eigenvalues of $\rho^{(1)}(\vec{r}', \vec{r}, t)$ are of the same order.

The above definition can be easily generalised to bosons with internal spin degrees of freedom labeled as above by an index m_F. Here the scalar boson field operator in Eq. (1.1) becomes a vector boson field operator with components $\hat{\Psi}_{m_F}(\vec{r}, t)$, and hence the single particle density matrix takes the form [65]

$$\rho^{(1)}(\vec{r}', m_F'; \vec{r}, m_F; t) = \langle \hat{\Psi}^\dagger_{m_F'}(\vec{r}', t)\hat{\Psi}_{m_F}(\vec{r}, t)\rangle. \tag{1.2}$$

An alternative (and closely related) definition of condensation in quantum many-body systems is based on the concept of off-diagonal long-range order (ODLRO) [66]. Instead of diagonalizing $\rho^{(1)}(\vec{r}', \vec{r}, t)$, in ODLRO one is interested in the limit $|\vec{r}' - \vec{r}| \to \infty$. If the density matrix is finite in this limit,

---

[2]The first experimentally produced BEC of alkaline earth atoms

[3]Electron-hole pair in a semiconductor.

[4]Polaritons are quasiparticles resulting from the coupling of photons with an excitation in the material. Exciton polariton is due to the coupling of visible light with an exciton.

[5]A quantum of a spin wave.

particles far away from each other are still correlated (coherent) and can be expressed by a macroscopic wave-function $\Psi(\vec{r}, t)$ via

$$\lim_{|\vec{r}'-\vec{r}|} \rho^{(1)}(\vec{r}', \vec{r}, t) = \Psi^*(\vec{r}', t)\Psi(\vec{r}, t). \tag{1.3}$$

This wave function $\Psi(\vec{r}, t)$ can be identified as a scalar order parameter characterizing the BEC. The concept of order parameters appears in the context of phase transitions in ordered media and spontaneous symmetry breaking. Note that cooling below T_C can be considered as a phase-transition from the normal phase to the BEC phase, where the $U(1)$ gauge symmetry of the energy-functional is spontaneously broken [67, 68], i.e. the BEC "chooses" a certain phase.

1.1.3 Dimensionality

Dimensionality plays a crucial role in the concept of condensation. An ideal Bose gas with no external trap exhibits BEC only in 3D, and not in 2D (at finite T) and 1D (at any T). This may be understood by considering the corresponding density of states, $\rho(E)$. For an ideal untrapped Bose gas the density of states is $\rho(E) \propto E^{(d-2)/2}$, where d is the dimensionality in space. In 3D, the number of excited states close to the ground state ($E = 0$) is zero since $\lim_{E \to 0} \rho(E) = 0$, and as a consequence thermal or quantum fluctuations do not destroy the BEC. On the contrary, in 2D and 1D, the thermal population

$$N_T = \int_0^\infty \frac{\rho(E)dE}{\exp(\beta E) - 1} \tag{1.4}$$

diverges in the thermodynamic limit, and hence the BEC is destabilized at finite T. However, with an additional harmonic trap the density of states modifies as $\rho(E) \propto E^{d-1}$ and, consequently the integral (1.4) converges in 2D. In 1D, BEC cannot occur even in the presence of harmonic confinement because of the logarithmic divergence in the integral (1.4).

The presence of interactions changes the picture even further. Inter-atomic interactions play a crucial role in the BEC physics. The interactions may be typically considered as isotropic and short-ranged (although dipole-dipole interactions may play an important role as discussed in Chapter 5 of this Thesis), being determined at low energies by a single parameter, namely the s-wave scattering length a_s [69]. The scattering length can be tuned experimentally via Feshbach resonances by sweeping the static magnetic field [70, 71]. If $a_s > 0$, the interatomic interaction is purely repulsive and the BEC is stable in all dimensions, for any trap configurations and for any number of atoms. If the interaction is attractive, i.e. $a_s < 0$, the homogeneous (not trapped) BECs are unstable against local collapses in 2D and 3D. The presence of a trap guarantees stability below a critical number of atoms, above which the BEC undergoes a global collapse in 2D and 3D [72–74].

1.1.4 The Gross-Pitaevskii equation

The Gross-Pitaevskii equation (GPE), developed in the early 1960s by Pitaevskii [75] and Gross [76, 77], describes sucessfully most of the BEC properties at very low temperatures. In the following we briefly discussed the derivation of this important equation.

The many-body Hamiltonian describing N weakly interacting spinless bosons confined by an external potential $V_{ext}(\vec{r})$ is given by [69]

$$\hat{H} = \int d\vec{r}\hat{\Psi}^\dagger(\vec{r}, t) \left[-\frac{\hbar^2}{2M}\nabla^2 + V_{ext}(\vec{r}) \right] \hat{\Psi}(\vec{r}, t)$$
$$+\frac{1}{2} \int d\vec{r} \int d\vec{r}'\hat{\Psi}^\dagger(\vec{r}, t)\hat{\Psi}^\dagger(\vec{r}', t)V(\vec{r} - \vec{r}')\hat{\Psi}(r\,', t)\hat{\Psi}(\vec{r}, t), \qquad (1.5)$$

where $\hat{\Psi}(\vec{r}, t)$ and $\hat{\Psi}^\dagger(\vec{r}', t)$ are the scalar boson field operators, and $V(\vec{r} - \vec{r}')$ is the two-body interatomic potential, with M is the atom mass. One applies the so-called *Bogoliubov approximation* [78], first formulated by Bogoliubov in 1947 [78], to separate the condensate contribution from the bosonic field operator. Accordingly, the Bose field operator can be decomposed into $\hat{\Psi}(\vec{r}, t) = \sum_i \Psi_i(\vec{r}, t)\hat{a}_i$ with single-particle wave-functions $\Psi_i(\vec{r}, t)$ and annihilation operators $\hat{a}_i$. In the presence of a condensate the expectation value of the ground-state is macroscopic ($N \to \infty$) and hence [78]

$$\langle\hat{a}_0^\dagger\hat{a}_0\rangle_0 = N_0 \simeq (N_0 + 1) = \langle\hat{a}_0\hat{a}_0^\dagger\rangle_0. \qquad (1.6)$$

This means that $\hat{a}_0$ and $\hat{a}_0^\dagger$ commute and can be treated as c-numbers $\hat{a}_0 \simeq \hat{a}_0^\dagger \simeq \sqrt{N_0}$. Thus the condensate is described by a macroscopically occupied complex wave function (recall the discussion above). On the contrary the particles in the excited states still require an operator treatment. As a result the Bose field operator may be decomposed into

$$\hat{\Psi}(\vec{r}, t) = \Psi(\vec{r}, t) + \hat{\Psi}'(\vec{r}, t), \qquad (1.7)$$

where $\Psi(\vec{r}, t) \equiv \langle\hat{\Psi}(\vec{r}, t)\rangle$, is known as the macroscopic wavefunction of the condensate, while $\hat{\Psi}'(\vec{r}, t)$ describes the non-condensed part (or excitations on the condensate).

The time evolution of the Bose field operator is obtained using the Heisenberg equation,

$$i\hbar\frac{\partial}{\partial t}\hat{\Psi}(\vec{r}, t) = \left[\hat{\Psi}(\vec{r}, t), \hat{H}\right] = \left[-\frac{\hbar^2}{2M}\nabla^2 + V_{ext}(\vec{r})\right] \hat{\Psi}(\vec{r}, t)$$
$$+ \int d\vec{r}'\hat{\Psi}^\dagger(\vec{r}', t)V(\vec{r}' - \vec{r})\hat{\Psi}(\vec{r}', t)\hat{\Psi}(\vec{r}, t). \qquad (1.8)$$

We consider the case of a dilute ultracold gas, in which only binary collisions at low energy are relevant. As mentioned above these collisions are characterized

by a single parameter, the s-wave scattering length a_s, independently of the details of the two-body potential. Hence the interatomic potential can be replaced by an effective delta-function pseudo-potential [69, 78–81] of the form $V(\vec{r}' - \vec{r}) = g\delta(\vec{r}' - \vec{r})$, where the coupling constant $g = 4\pi\hbar^2 a_s/M$. Inserting the pseudo-potential into Eq. (1.8), and upon replacing the field operator $\hat{\Psi}(\vec{r}, t)$ with the classical field $\Psi(\vec{r}, t)$, we obtain

$$i\hbar\frac{\partial}{\partial t}\Psi(\vec{r}, t) = \left[-\frac{\hbar^2}{2M}\nabla^2 + V_{ext}(\vec{r}) + g|\Psi(\vec{r}, t)|^2\right]\Psi(\vec{r}, t). \qquad (1.9)$$

This equation is known as the Gross-Pitaevskii equation (GPE) [75–77], which remains valid if a_s is much smaller than the average inter-particle distance and if the number of condensed atoms $N_c \gg 1$, such that the product $N_c a_s$ is fixed [82]. In addition, we demand that the wave function $\Psi(\vec{r}, t)$ satisfies the constraint

$$\int |\Psi(\vec{r}, t)|^2 d\vec{r} = N, \qquad (1.10)$$

that defines the conservation of total number of particles, N.

Note that the GPE has actually the form of a non-linear Schrödinger (NLS) equation, (the non-linearity coming from the mean-field term, proportional to the particle density $n(\vec{r}) = |\Psi(\vec{r})|^2$). NLS equation is a key model appearing in a variety of physical contexts, ranging from Kerr media in non-linear optics to fluid dynamics and plasma physics [83]. As already mentioned, this resemblance has attracted a large interest of the nonlinear community onto the BEC physics.

Note that $\Psi(\vec{r}, t) = \langle\hat{\Psi}(\vec{r}, t)\rangle$ actually means $\langle N - 1|\hat{\Psi}(\vec{r}, t)|N\rangle$ since the Bose-field operator $\hat{\Psi}(\vec{r}, t)$ destroys one particle. Hence the condensate wavefunction $\hat{\Psi}(\vec{r}, t)$ oscillates at a frequency corresponding to the chemical potential $\mu = \frac{\partial E}{\partial N} \simeq E(N) - E(N - 1)$, given by with the energy change associated to the removal of one particle [84]. Hence the time-dependence of the ground-state condensate is given by $\Psi(\vec{r}, t) = \Psi(\vec{r})\exp(-i\mu t/\hbar)$, leading to the time-independent GPE

$$\mu\Psi(\vec{r}) = \left[-\frac{\hbar^2}{2M}\nabla^2 + V_{ext}(\vec{r}) + g|\Psi(\vec{r})|^2\right]\Psi(\vec{r}). \qquad (1.11)$$

Note that the chemical potential μ acts as a Lagrange multiplier for the minimization of the free energy $F = E - \mu N$ at small temperatures, associated with the conservation of the total particle number. Here the energy functional, E, consisting of kinetic energy, potential energy and interaction energy is given by

$$E = \int d\vec{r}\left[\frac{\hbar^2}{2M}|\nabla\Psi|^2 + V_{ext}(\vec{r})|\Psi(\vec{r})|^2 + \frac{1}{2}g|\Psi(\vec{r})|^4\right]. \qquad (1.12)$$

Alternatively, one may also derive the time-independent GPE from this energy functional using a variational method,

$$i\hbar \frac{\partial}{\partial t} \Psi(\vec{r}, t) = \frac{\partial E}{\partial \Psi^*(\vec{r}, t)}. \tag{1.13}$$

1.2 Spinor Bose-Einstein Condensation

As already mentioned above, spinor condensates are formed by particles with more than one available internal degree of freedom (spin), and hence the scalar order parameter that describes a scalar condensate becomes a vector order parameter in a spinor BEC $\vec{\Psi}(\vec{r}, t) = [\Psi_F, ..., \Psi_{-F}]^T$ with $2F + 1$ components. Spinor condensates constitute indeed an ideal scenario to investigate the interplay between internal and external degrees of freedom in a multi-component superfluid. The fascinating physics of spinor condensates stems from the competition between various energy scales, including short range interactions, dipole-dipole interactions, and Zeeman effect. In the following we discuss these energy scales.

1.2.1 Short-range interactions in spinor condensates

We consider first the short-range interactions in spinor condensates, which for the extremely low energies relevant in ultra-cold gases are dominated by two-body s-wave collisions. The microscopic picture of an ultracold collision of two identical bosonic spinors is illustrated in Fig. (1.1) . When two atoms approach each other, their spins will temporarily couple together to form a total spin, and the two atomic spins precess around this total spin during the collision. After the collision, the two spins decouple and the atoms move away from each other. For two identical spin-f particles, the total spin is given by $\vec{F} = \vec{f_1} + \vec{f_2}$, and the allowed total spins are $F = 2f, 2f - 1, ..., 0$. However, due to the symmetry (anti-symmetry) required by identical bosons (fermions), for integer f only F even (odd) channels are allowed for bosons (fermions), when the total spatial wavefunction of the two atoms is symmetric (as it is the case in s-wave collisions). The short-range interaction conserves the total spin F. Here we focus on the particular case of spin $f = 2$ condensates, thus the allowed collisional channels are $F = 4, 2, 0$. Hence three parameters are required to describe the interactions, namely the s-wave scattering lengths $a_{F=4}$, $a_{F=2}$, and $a_{F=0}$.

An important feature of the short-range interactions is that due to their isotropy, they do not modify the spin projection of the pair along the quantization axis. This means that if the in-coming pair has spins $m_{F,1}$ and $m_{F,2}$, and the out-going one $m_{F,3}$ and $m_{F,4}$, then $m_{F,1} + m_{F,2} = m_{F,3} + m_{F,4}$ (conservation of the magnetization). Note that, crucially, this may be realized in two

non-equivalent ways. One way is given by the so-called spin-preserving colli-
sions, for which $m_{F,1} = m_{F,3}$ ($m_{F,1} = m_{F,4}$) and $m_{F,2} = m_{F,4}$ ($m_{F,2} = m_{F,3}$).
Interestingly, there is an alternative way in which the population of the differ-
ent components is re-distributed, but the conservation of the magnetization
is preserved. These are the so-called spin-changing collisions, which play a
crucial role in the following discussion and in this Thesis in general.
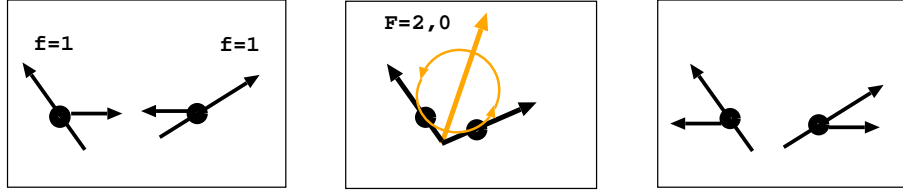
FIGURE 1.1: Intuitive picture of atomic interactions in spinor condensates: binary
collision of spin-1 bosons. (Left) Two spin-1 bosons approach each other. (Center)
The atomic spin of two bosons couple to form a total spin, and then the bosons
precess around this total spin during the collisions. The total spin can be $F = 2, 0$.
(right) Two bosons break apart after collision is finished

The short-range interaction between two particles 1 and 2 may be decom-
posed into contributions from the different channels in the form:

$$\hat{V}_{sr}(\vec{r}_1 - \vec{r}_2) = \delta(\vec{r}_1 - \vec{r}_2) \sum_{F=0}^{2f} g_F \hat{P}_F, \tag{1.14}$$

where $g_F = 4\pi\hbar^2 a_F/M$ is the coupling strength for the F-channel (with M
the atomic mass) and $\hat{P}_F$ is the projection operator onto a two-particle state
with total spin-F:

$$\hat{P}_F = \sum_{m_F=-F}^{F} |F, m_F\rangle\langle F, m_F|. \tag{1.15}$$

For identical bosons, the projection operators satisfy the following closure
relationship:

$$\mathbf{1} = \sum_{F=0,2}^{2F} \hat{P}_F. \tag{1.16}$$

On the other hand, since $\hat{\vec{f}}_1 \cdot \hat{\vec{f}}_2 = (\hat{\vec{F}}^2 - \hat{\vec{f}}_1^2 - \hat{\vec{f}}_2^2)/2$, then

$$\hat{\vec{f}}_1 \cdot \hat{\vec{f}}_2 = \sum_F \lambda_F \hat{P}_F, \tag{1.17}$$

where $\lambda_F \equiv \frac{\hat{F}(\hat{F}+1) - 2\vec{f}(\vec{f}+1)}{2}$.

For spin-2 condensates, Eq. (1.16) and Eq. (1.17) lead to

$$\mathbf{1} = \hat{P}_0 + \hat{P}_2 + \hat{P}_4, \tag{1.18}$$

$$\hat{\vec{f}}_1 \cdot \hat{\vec{f}}_2 = -10\hat{P}_0 - 7\hat{P}_2 + 4 \tag{1.19}$$

respectively. Employing the above two identities, Eq. (1.14) takes the form

$$\hat{V}_{sr}(\vec{r}_1 - \vec{r}_2) = \delta(\vec{r}_1 - \vec{r}_2)(c_0 + c_1\hat{\vec{f}}_1 \cdot \hat{\vec{f}}_2 + c_2\hat{P}_0). \tag{1.20}$$

Where c_0, c_1, c_2 are coupling constants given by

$$c_0 = \frac{4g_2 + 3g_4}{7}, \tag{1.21a}$$

$$c_1 = \frac{g_4 - g_2}{7}, \tag{1.21b}$$

$$c_2 = \frac{7g_0 - 10g_2 + 3g_4}{7}. \tag{1.21c}$$

Note that c_0 acts as a coupling constant for spin-independent interactions, and hence it is related with spin-preserving collisions. Note that if all a_F are similar to each other (which turns out to be the typical case in experiments), then $c_0 \simeq \bar{a}$, where $\bar{a}$ is the average scattering length.

On the contrary c_1 and c_2 are coupling constants for spin-dependent interactions, being related to the above mentioned spin-changing collisions. Note that $c_{1,2}$ vanish if all a_F are exactly equal, i.e. there are no spin-changing collisions in exact SU(2F+1) systems. Since the scattering lengths are not exactly equal, spin-changing collisions are generally present, although their energy scale is typically much smaller than that of the spin-preserving collisions. This makes spin-changing collisions sensitive against other small energy scales, as e.g. dipole-dipole interactions, as discussed next.

1.2.2 Dipole-dipole interactions in spinor condensates

The atomic spins have an associated magnetic dipole moment, and hence interact via a magnetic dipole-dipole interaction of the form

$$V_{\mathrm{dd}}(\vec{r} - \vec{r}') = \frac{c_{dd}}{|\vec{r} - \vec{r}'|^3}\left[\vec{f}_1 \cdot \vec{f}_2 - 3\left(\vec{f}_1 \cdot \vec{u}_r\right)\left(\vec{f}_2 \cdot \vec{u}_r\right)\right] \tag{1.22}$$

where $c_{dd} = \frac{\mu_0(g_s m u_B)^2}{4\pi}$ denotes the coupling constant associated to the dipolar interaction (with μ_0 the vacuum magnetic permeability, μ_B the Bohr magneton and g_s the gyromagnetic factor), and $\vec{u}_r = \frac{\vec{r} - \vec{r}'}{|\vec{r} - \vec{r}'|}$ is the unit vector along the relative interparticle distance.

Dipole-dipole interactions are typically very weak in alkaline gases, due to the very low magnetic dipole moment. However, as mentioned above, spin-changing collisions are also very weak, and hence (especially for ^{87}Rb $F = 1$)

the dipole-dipole interactions may play a relevant role in the spinor dynamics. At this point we shall not comment further on dipolar effects, which will be discussed in details in Chapter 5.

1.2.3   Spinors In Magnetic Fields

The associated magnetic moment of the spins couples with any external magnetic field, leading to a Zeeman energy shift. This spin-dependent energy shift is crucial for the physics of spinor condensates, and hence it will be discussed in detail at this point.

We note that (in absence of orbital angular momentum) the spin $\vec{f}$ results from the composition of nuclear spin $\vec{i}$ and electron spin $\vec{s}$. For ^{87}Rb and ^{23}Na atoms, the nuclear spin is $i = 3/2$ and the electron spin is $s = 1/2$, thus the total spin becomes $f = 1$ or $f = 2$. Both spins interact with each other and with the external magnetic field and hence the Zeeman Hamiltonian:

$$H_Z = g_e \mu_B B s_z - g_n \mu_n B i_z + C_{\mathrm{hfs}} \vec{s} \cdot \vec{i}. \qquad (1.23)$$

Here, $g_e \approx 2$ is the electron g-factor, g_n is the nuclear g-factor, μ_n is the nuclear magneton, C_{hfs} is the hyperfine constant, and $\vec{s} = (s_x, s_y, s_z)$ and $\vec{i} = (i_x, i_y, i_z)$ are the dimensionless spin-1/2 and spin-3/2 matrices respectively. We can safely neglect the second term of Eq. (1.23) since $g_n \mu_n / g_e \mu_B \approx 10^{-11}$, and H_Z can be easily diagonalized analytically (its energy spectrum is plotted in Fig. 1.2).

At zero magnetic field H_Z consists only of the spin-spin coupling which is diagonal in the basis of total spin. Using

$$\vec{f}^2 = (\vec{s} + \vec{i})^2 = \vec{s}^2 + \vec{i}^2 + 2\vec{s} \cdot \vec{i} \quad \Rightarrow \quad \vec{s} \cdot \vec{i} = \vec{f}^2/2 - 9/4 \qquad (1.24)$$

we obtain the hyperfine shifts

$$C_{\mathrm{hfs}} \vec{s} \cdot \vec{i} |f = 1, m_f\rangle = -5/4 C_{\mathrm{hfs}} |f = 1, m_f\rangle$$
$$C_{\mathrm{hfs}} \vec{s} \cdot \vec{i} |f = 2, m_f\rangle = +3/4 C_{\mathrm{hfs}} |f = 2, m_f\rangle.$$

The energy shifts are drawn as blue arrows leftmost in Fig. 1.2. Thus all $f = 2$ states are shifted upwards by $E_Z = +3/4 C_{\mathrm{hfs}}$ and all $f = 1$ states are shifted downwards by $E_Z = -5/4 C_{\mathrm{hfs}}$.

For small magnetic fields it is often sufficiently accurate to approximate the real eigenstates by $\vec{f}^2$ eigenstates (f and m_f are 'good' quantum numbers). By using Eq. (1.24) and the Wigner-Eckart theorem [85]

$$P_f s_z P_f = \frac{\langle \vec{s} \cdot \vec{f} \rangle_f}{\langle \vec{f}^2 \rangle_f} P_f f_z P_f$$
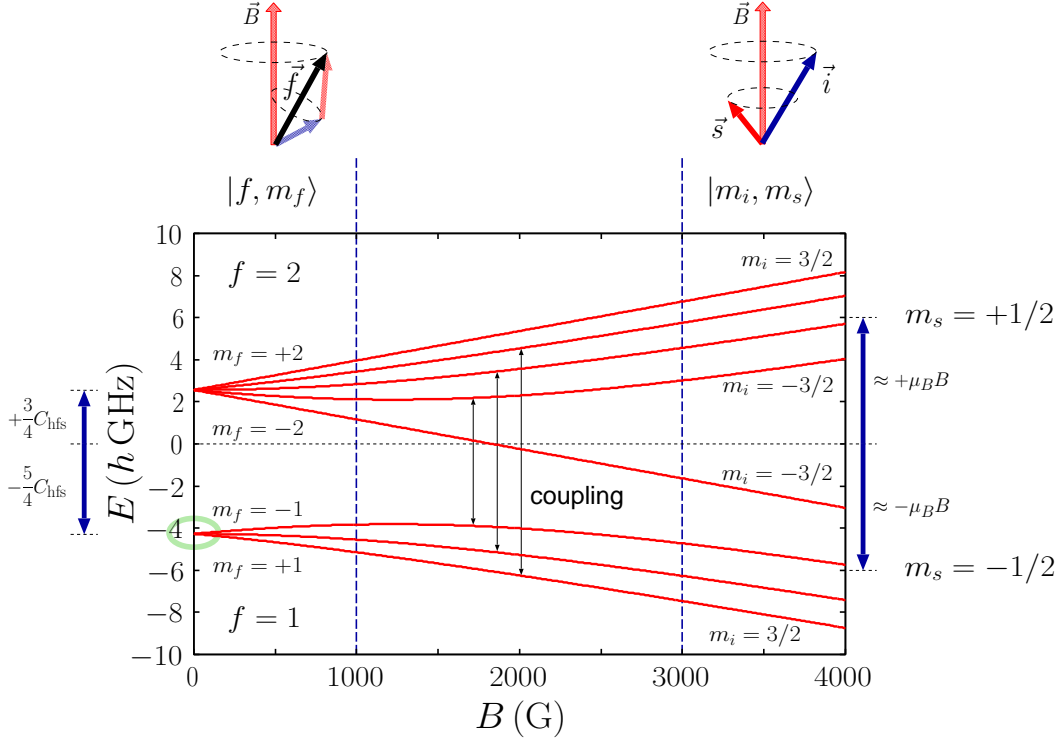
FIGURE 1.2: Zeeman energy of ^{87}Rb atoms in dependence of the magnetic field $|\vec{B}|$. For small $|\vec{B}|$ the nuclear spin $\vec{i}$ and the electron spin $\vec{s}$ couple to the total spin $\vec{f}$ which precesses around the magnetic field axis. For large $|\vec{B}|$ both spins $\vec{i}$ and $\vec{s}$ precess independently around $\vec{B}$. Although the experiments are performed at very low magnetic fields (green circle) the nonlinear behavior of the energy due to the coupling between $f = 1$ and $f = 2$ states is not negligible.

(P_f is the projection operator onto the Hilbert space with spin f and the expectation values have to be calculated with states from this subspace) we obtain the first-order approximation of the Zeeman energy

$$E_Z \approx \langle f, m_f | H_Z | f, m_f \rangle = \underbrace{\left[g_e \frac{f(f+1) - 3}{2f(f+1)} \right]}_{=:g_f \,(\text{Landé factor})} \mu_B B m_f + C_{\text{hfs}} \left[f(f+1)/2 - 9/4 \right].$$

The Landé factor for $f = 1$ states is $g_1 = -1/2$ and for $f = 2$ states is $g_2 = 1/2$ (for an illustrative calculation of the Landé factor see Ref. [86]). The first-order low-$|\vec{B}|$ result is thus given by

$$
\begin{aligned}
E_Z(f = 1) &\approx -5/4 C_{\text{hfs}} - \mu_B B m_f / 2, &\quad (1.25) \\
E_Z(f = 2) &\approx +3/4 C_{\text{hfs}} + \mu_B B m_f / 2. &\quad (1.26)
\end{aligned}
$$

This behavior can be seen in Fig. 1.2 in the region $B < 1000\,\text{G}$. Note that for $f = 2$ the state with $m_f = 2$ has highest energy whereas for $f = 1$ the

state with $m_f = -1$ has highest energy due to the negative sign of the Landé factor.

Let us now consider the other extreme case of large magnetic fields $2\mu_B B \gg C_{\text{hfs}}$. Here we use $\{\langle m_s, m_i \rangle\}$ eigenstates. Employing the relations

$$\vec{s} \cdot \vec{i} = i_z \otimes s_z + \frac{1}{2}(i_+ \otimes s_- + i_- \otimes s_+) \qquad (1.27)$$

with $i_\pm \equiv i_x \pm \mathrm{i} i_y$ (and analog for $s_\pm$) and

$$i_\pm |i, m_i\rangle = \sqrt{i(i+1) - m_i(m_i \pm 1)} |i, m_i \pm 1\rangle, \qquad (1.28)$$

and analog for $s_\pm$, we obtain the first-order approximation of the Zeeman energy in the region of large magnetic fields

$$E_Z \approx \langle m_i, m_s | H_Z | m_i, m_s \rangle = 2\mu_B B m_s + C_{\text{hfs}} m_i m_s. \qquad (1.29)$$

Thus in the region $B > 3000\,\text{G}$ we observe two multiplets which are shifted by an average energy of $\Delta E \approx \pm\mu_B B$ (see the blue arrows rightmost of Fig. 1.2). The average spacing between the four states of each multiplet is $\Delta E \approx C_{\text{hfs}}/2$. Note again that the ordering within the lower multiplet is inverted since $m_s = -1/2$.

In the intermediate region $1000\,\text{G} < B < 3000\,\text{G}$ the energy depends non-linearly on B (except for the fully stretched states) and the coupling between states with the same m_f $\left(|1, m_f\rangle \leftrightarrow |2, m_f\rangle, m_f = -1, 0, 1\right)$ continuously rotates $\vec{f}^{\,2}$ into (i_z, s_z) eigenstates, i.e. the eigenstates are intermediate between the states $|F, m_f\rangle$ and $|m_s, m_f\rangle$. Note that the energy of the fully stretched states $\left(|2, 2\rangle = |3/2, 1/2\rangle$ and $|2, -2\rangle = |-3/2, -1/2\rangle\right)$ depends linearly on B for all magnetic fields since they are not coupled to other states. Thus, they are eigenstates of H_Z for all magnetic fields and their energy is exactly given by Eqs. (1.25) or (1.29). The energy of the other states for all magnetic fields can be obtained by diagonalizing the 8×8 matrix of H_Z [86] and it turns out to be

$$E_Z = -\frac{C_{\text{hfs}}}{4} + (-1)^f \left[C_{\text{hfs}} + \frac{\mu_B B}{2} m_f + \frac{\mu_B^2 B^2}{2 C_{\text{hfs}}} \left(1 - \frac{m_f^2}{4} \right) \right]. \qquad (1.30)$$

In current experiments all the atoms are initially prepared in spin state $f = 2$ or $f = 1$ and the magnetic field strength is of the order of a few Gauss, which is indicated by the green circle in Fig. 1.2. Hence one can neglect the constant hyperfine shift and the small admixture $|f = 2, m_f\rangle$ and $|f = 1, m_f\rangle$ of Eq.(1.30),

$$E_Z = p m_f + q m_f^2. \qquad (1.31)$$

Here $p = \frac{(-1)^f \mu_B B}{2}$ is the linear Zeeman effect and $q = (-1)^{f+1} \frac{\mu_B^2 B^2}{8 C_{\text{hfs}}}$ is the quadratic Zeeman effect, which is $q < 0$ for $f = 2$ and $q > 0$ for $f = 1$.

Note, however, that the value for q (and even its sign) may be also externally modified (independently of p) using optical or micro-wave dressing [87, 88].

Finally, let us mention that up to this point we have just considered homogeneous magnetic fields, but typical experiments may present also non-negligible magnetic field gradients $\nabla B \cdot \vec{r}$. Since the magnitude of such gradients is typically small, the quadratic term contribution can be neglected. The corresponding linear term leads to an energy shift $m_f \nabla p \cdot \vec{r}$, which may play a relevant role in the spinor dynamics, as discussed in detail in Chapter 5.

Summarizing, the Zeeman Hamiltonian together with the magnetic gradient effect becomes of the form

$$E_Z = pm_f + m_f \nabla p \cdot \vec{r} + qm_f^2. \tag{1.32}$$

Note that short-range interactions preserve magnetization. In addition, although the dipole-dipole interactions may in principle violate the conservation of magnetization, this violation is typically forbidden due to Larmor precession (which constitutes a large energy scale even at very low magnetic fields). As a result, the system dynamics is characterized by a conserved magnetization and hence the linear Zeeman energy has no effect on the dynamics. However, the quadratic Zeeman energy plays a crucial role in the spinor dynamics, and in the results of this Thesis. As mentioned above also the magnetic field gradients may be relevant, as discussed in Chapter 5.

1.3 Second Quantized Hamiltonian

In the previous section we analyzed the most relevant energy scales in the spinor system. In this section we sum up these energy scales into a second-quantized Hamiltonian. In the following we consider an optically-trapped spin-2 ^{87}Rb BEC in an external magnetic field oriented along the z-axis. The second-quantized single-particle Hamiltonian is given by

$$\hat{H}_0 = \sum_{m_f} \int d^3r \, \hat{\psi}_{m_f}^\dagger(\vec{r}) \left[-\frac{\hbar^2}{2M}\Delta + V(\vec{r}) + E_Z \right] \hat{\psi}_{m_f}(\vec{r}), \tag{1.33}$$

where we may recognize the kinetic energy, the optical trapping, $V(\vec{r})$, which is the same for all Zeeman sublevels, and the Zeeman energy, which is given by Eq. (1.32). Here the summation index runs over all Zeeman sublevels $m_f = 2, 1, 0, -1, -2$. The bosonic field annihilation operator has hence five components $\hat{\psi}_2(\vec{r}), \hat{\psi}_1(\vec{r}), \hat{\psi}_0(\vec{r}), \hat{\psi}_{-1}(\vec{r}), \hat{\psi}_{-2}(\vec{r})$. For simplicity, we use m instead of m_f in the rest of the thesis.

The second-quantized two-particle Hamiltonian that describes short-range interactions is of the form

$$\hat{H}_{\text{sr}} = \frac{1}{2} \int d^3\vec{r} \sum_{\vec{m}} U_{\vec{m}} \hat{\psi}_{m_4}^\dagger(\vec{r}) \hat{\psi}_{m_3}^\dagger(\vec{r}) \hat{\psi}_{m_2}(\vec{r}) \hat{\psi}_{m_1}(\vec{r}), \tag{1.34}$$

where

$$U_{\vec{m}} = \sum_{F} \sum_{M=-F}^{F} g_F \langle m_1, m_2 | F, M \rangle \langle F, M | m_3, m_4 \rangle \quad (1.35)$$

are the coupling constants for the collisional channels $\{m_1, m_2\} \to \{m_3, m_4\}$ ($\vec{m} \equiv (m_1, m_2, m_3, m_4)$), where $\langle m_1, m_2 | F, M \rangle$ are the Clebsch-Gordan coefficients.

The above second-quantized short-range interaction Hamiltonian can be obtained from the second-quantized form of Eq. (1.20) and reduced to

$$\hat{H}_{\text{sr}} = \frac{c_0}{2} \int d^3\vec{r} \sum_{mm'} \hat{\psi}_{m'}^\dagger(\vec{r}) \hat{\psi}_m^\dagger(\vec{r}) \hat{\psi}_{m'}(\vec{r}) \hat{\psi}_m(\vec{r})$$

$$+ \frac{c_1}{2} \int d^3\vec{r} \sum_{\vec{m}} \hat{\psi}_{m_4}^\dagger(\vec{r}) \hat{\psi}_{m_3}^\dagger(\vec{r}) \hat{\vec{F}}_{m_3 m_2} \cdot \hat{\vec{F}}_{m_4 m_1} \hat{\psi}_{m_2}(\vec{r}) \hat{\psi}_{m_1}(\vec{r})$$

$$+ \frac{c_2}{2} \int d^3\vec{r} \sum_{\vec{m}} \hat{\psi}_{m_4}^\dagger(\vec{r}) \hat{\psi}_{m_3}^\dagger(\vec{r}) \langle m_4; m_3 | 0, 0 \rangle \langle 0, 0 | m_2; m_1 \rangle \hat{\psi}_{m_2}(\vec{r}) \hat{\psi}_{m_1}(\vec{r}),$$

$$(1.36)$$

where $c_{0,1,2}$ are defined in Eqs. (1.21), and $\hat{\vec{F}}_{m_3 m_2} \cdot \hat{\vec{F}}_{m_4 m_1} = (\hat{F}_\alpha)_{m_3 m_2} (\hat{F}_\alpha)_{m_4 m_1}$, where $(\hat{F}_\alpha)_{m_3 m_2}$ are the matrix elements for the Cartesian traceless spin $F = 2$ Pauli matrices,

$$\hat{F}_x = \frac{1}{2} \begin{pmatrix} 0 & 2 & 0 & 0 & 0 \\ 2 & 0 & \sqrt{6} & 0 & 0 \\ 0 & \sqrt{6} & 0 & \sqrt{6} & 0 \\ 0 & 0 & \sqrt{6} & 0 & 2 \\ 0 & 0 & 0 & 2 & 0 \end{pmatrix}, \quad \hat{F}_y = \frac{\mathrm{i}}{2} \begin{pmatrix} 0 & -2 & 0 & 0 & 0 \\ 2 & 0 & -\sqrt{6} & 0 & 0 \\ 0 & \sqrt{6} & 0 & -\sqrt{6} & 0 \\ 0 & 0 & \sqrt{6} & 0 & -2 \\ 0 & 0 & 0 & 2 & 0 \end{pmatrix}$$

and

$$\hat{F}_z = \begin{pmatrix} 2 & 0 & 0 & 0 & 0 \\ 0 & 1 & 0 & 0 & 0 \\ 0 & 0 & 0 & 0 & 0 \\ 0 & 0 & 0 & -1 & 0 \\ 0 & 0 & 0 & 0 & -2 \end{pmatrix},$$

with z the quantization axis.

Re-writing the state $|0, 0\rangle$ in terms of the five Zeeman sublevels (see Appendix A), the short-range interaction Hamiltonian may be re-written in the

form

$$
\begin{aligned}
\hat{H}_{\text{sr}} = {} & \frac{c_0}{2} \int d^3\vec{r} \sum_{mm'} \hat{\psi}^\dagger_{m'}(\vec{r}) \hat{\psi}^\dagger_m(\vec{r}) \hat{\psi}_{m'}(\vec{r}) \hat{\psi}_m(\vec{r}) \\
& + \frac{c_1}{2} \int d^3\vec{r} \sum_{\vec{m}} \hat{\psi}^\dagger_{m_4}(\vec{r}) \hat{\psi}^\dagger_{m_3}(\vec{r}) \hat{\vec{F}}_{m_3 m_2} \cdot \hat{\vec{F}}_{m_4 m_1} \hat{\psi}_{m_2}(\vec{r}) \hat{\psi}_{m_1}(\vec{r}) \\
& + \frac{c_2}{10} \int d^3\vec{r} \sum_{m,n} (-1)^{m+n} \hat{\psi}^\dagger_m(\vec{r}) \hat{\psi}^\dagger_{-m}(\vec{r}) \hat{\psi}_n(\vec{r}) \hat{\psi}_{-n}(\vec{r}). \quad (1.37)
\end{aligned}
$$

In this short-range interaction Hamiltonian, the first term represents the intra-state collisions, or the self-scattering, and the next two terms represent the inter-state collisions and the spin-changing collisions. As already mentioned, the short-range interaction Hamiltonian leaves the total spin projection invariant ($m_1 + m_2 = m_3 + m_4$). The coupling strength coefficients of all possible collisions in the system are tabulated in Table 1.3.

U_{m_1,m_2,m_1,m_2}	2	1	0	-1	-2
2	$c_0 + 4c_1$	$\frac{c_0+4c_1}{2}$	$\frac{c_0}{2}$	$\frac{c_0}{2} - c_1$	$\frac{c_2}{5} + c_0 - 2c_1$
1	$\frac{c_0+4c_1}{2}$	$c_0 + c_1$	$\frac{c_0+3c_1}{2}$	$\frac{c_2}{5} + \frac{c_0-c_1}{2}$	$\frac{c_0}{2} - c_1$
0	$\frac{c_0}{2}$	$\frac{c_0+3c_1}{2}$	$\frac{c_2}{5} + c_0$	$\frac{c_0+3c_1}{2}$	$\frac{c_0}{2}$
-1	$\frac{c_0}{2} - c_1$	$\frac{c_2}{5} + \frac{c_0-c_1}{2}$	$\frac{c_0+3c_1}{2}$	$c_0 + c_1$	$\frac{c_0+4c_1}{2}$
-2	$\frac{c_2}{5} + c_0 - 2c_1$	$\frac{c_0}{2} - c_1$	$\frac{c_0}{2}$	$\frac{c_0+4c_1}{2}$	$c_0 + 4c_1$

$U_{2,-2,0,0}$	$\frac{c_2}{5}$
$U_{1,-1,0,0}$	$-\frac{c_2}{5} + 3c_1$
$U_{2,-2,1,-1}$	$-\frac{c_2}{5} + c_1$
$U_{2,0,1,1}$	$\sqrt{6}c_1$
$U_{2,-1,1,0}$	$\frac{\sqrt{6}c_1}{2}$
$U_{1,-2,-1,0}$	$\frac{\sqrt{6}c_1}{2}$
$U_{-2,0,-1,-1}$	$\sqrt{6}c_1$

TABLE 1.1: Table of two-body interaction strengths. Upper table lists the intra- and inter-state particle exchange collisions. Lower table lists the spin changing or spin mixing collisions

In addition, the contribution of the magnetic dipole-dipole interactions is given by the second-quantized form of Eq. (1.22):

$$
\begin{aligned}
\hat{H}_{\text{dd}} = {} & \frac{c_{dd}}{2} \sum_{\vec{m}} \int d^3r \, d^3r' \, \hat{\psi}^\dagger_{m_1}(\vec{r}) \hat{\psi}^\dagger_{m_2}(\vec{r}') \frac{1}{|\vec{r}-\vec{r}'|^3} \times \left[\hat{\vec{F}}_{m_1 m_3} \cdot \hat{\vec{F}}_{m_2 m_4} \right. \\
& \left. -3 \left(\hat{\vec{F}}_{m_1 m_3} \cdot \vec{u}_r \right) \left(\hat{\vec{F}}_{m_2 m_4} \cdot \vec{u}_r \right) \right] \hat{\psi}_{m_4}(\vec{r}') \hat{\psi}_{m_3}(\vec{r}), \quad (1.38)
\end{aligned}
$$

where the coupling c_{dd} and the unit vector $\vec{u}_r$ are defined in Eq. (1.22).

The total Hamiltonian of the system is then given by the sum $\hat{H} = \hat{H}_0 + \hat{H}_{\mathrm{sr}} + \hat{H}_{\mathrm{dd}}$, and takes the final form

$$
\begin{aligned}
\hat{H} = &\sum_m \int d^3r\, \hat{\psi}_m^\dagger(\vec{r}) \left[-\frac{\hbar^2}{2M}\Delta + V(\vec{r}) + pm + m\nabla p \cdot \vec{r} + qm^2 \right] \hat{\psi}_m(\vec{r}) \\
&+ \frac{c_0}{2} \int d^3\vec{r} \sum_{mm'} \hat{\psi}_{m'}^\dagger(\vec{r})\hat{\psi}_m^\dagger(\vec{r})\hat{\psi}_{m'}(\vec{r})\hat{\psi}_m(\vec{r}) \\
&+ \frac{c_1}{2} \int d^3\vec{r} \sum_{\vec{m}} \hat{\psi}_{m_4}^\dagger(\vec{r})\hat{\psi}_{m_3}^\dagger(\vec{r})\hat{\vec{F}}_{m_3 m_2} \cdot \hat{\vec{F}}_{m_4 m_1}\hat{\psi}_{m_2}(\vec{r})\hat{\psi}_{m_1}(\vec{r}) \\
&+ \frac{c_2}{10} \int d^3\vec{r} \sum_{m,n} (-1)^{m+n}\hat{\psi}_m^\dagger(\vec{r})\hat{\psi}_{-m}^\dagger(\vec{r})\hat{\psi}_n(\vec{r})\hat{\psi}_{-n}(\vec{r}) \\
&+ \frac{c_{dd}}{2} \sum_{\vec{m}} \int d^3r\, d^3r'\, \hat{\psi}_{m_1}^\dagger(\vec{r})\hat{\psi}_{m_2}^\dagger(\vec{r}')\frac{1}{|\vec{r}-\vec{r}'|^3} \\
&\times \left[\hat{\vec{F}}_{m_1 m_3} \cdot \hat{\vec{F}}_{m_2 m_4} - 3\left(\hat{\vec{F}}_{m_1 m_3} \cdot \vec{u}_r\right)\left(\hat{\vec{F}}_{m_2 m_4} \cdot \vec{u}_r\right) \right] \hat{\psi}_{m_4}(\vec{r}')\hat{\psi}_{m_3}(\vec{r}), \quad (1.39)
\end{aligned}
$$

1.4 Coupled Gross-Pitaevskii equations

The mean-field dynamics of a spin-2 BEC is governed by a set of coupled GPEs for the five Zeeman sublevels. As in our derivation of the scalar GPE, these coupled equations of motion may be obtained by means of the Heisenberg equations of motion,

$$
i\hbar \frac{\partial \hat{\psi}_m(\vec{r},t)}{\partial t} = [\hat{\psi}_m(\vec{r},t), \hat{H}]. \tag{1.40}
$$

Using Eq. (1.39) and Eq. (1.40) for the field operators and taking into account the mean-field approach, similar to the procedure for the scalar GPE, one obtains a set of five coupled GPEs of the form:

$$
\begin{aligned}
i\hbar \frac{\partial \psi_m(\vec{r},t)}{\partial t} =& \left[-\frac{\hbar^2}{2M}\Delta + V(\vec{r}) + m\nabla p \cdot \vec{r} + qm^2 \right] \psi_m(\vec{r},t) \\
&+ N(c_0 n + m(c_1 f_z + c_{dd}A_0)\psi_m(\vec{r},t) \\
&+ \frac{N}{2}\left[\left(c_1 f_- + 2c_{dd}A_-\right)S_{m,m-1}^+ \psi_{m-1}(\vec{r},t) \right. \\
&\left. + \left(c_1 f_+ + 2c_{dd}A_+\right)S_{m,m+1}^- \psi_{m+1}(\vec{r},t) \right] \\
&+ \frac{2Nc_2}{5}(-1)^m S_- \psi_{-m}^*(\vec{r},t) \tag{1.41}
\end{aligned}
$$

Where $f_{\pm}(\vec{r}) = \sum_{mn} \psi_m^* S_{mn}^{\pm} \psi_n$ is the spin density, $S_{m,m\mp1}^{\pm} = \sqrt{6 - m(m \mp 1)}$ and $S_- = \frac{1}{2} \sum_n (-1)^n \psi_n \psi_{-n}$ is the singlet-pair amplitude. The terms $A_0 = \int d^3\vec{r}' \frac{(1 - 3\cos^3\theta_{rr'})}{2|\vec{r} - \vec{r}'|^3} f_z(\vec{r}')$ and $A_{\pm} = \int d^3r' \frac{(3\cos^3\theta_{rr'} - 1)}{2|\vec{r} - \vec{r}'|^3} f_{\pm}(\vec{r}')$ characterize the dipole dipole interaction. In deriving these terms, we consider a sufficient large magnetic field along z-axis (the quantization axis) and hence we neglect collisions which do not conserve the total spin [89].

In Eq. (1.41) we find various spin-changing processes, which result in transfer of atoms among the different Zeeman sublevels. These spin changing processes are governed by the parameters c_1, which includes all couplings of states with $\Delta m_F = \pm 1$ (e.g $|0\rangle + |0\rangle \leftrightarrow |1\rangle + |-1\rangle$), c_2 that includes the only possible coupling with $\Delta m_F = \pm 2$ (e.g $|0\rangle + |0\rangle \leftrightarrow |2\rangle + |-2\rangle$), and c_{dd}, that regularizes the spin dynamics depending on the geometry of the trap, dimensionality, and orientation with respect to the magnetic field. The magnitude of these couplings provides the time scales for the spinor dynamics, and their relative strengths indicate the initially dominant channels (e.g. for ^{87}Rb $c_1 > c_2$). The above GPEs hence provide a rich physics given by the interplay between internal and external degrees of freedom.

1.5   Overview

This thesis is organized as follows:

In chapter 2 we analyze the first stages of the spinor dynamics (linear regime), focusing on the properties of the Bogolibov spectrum of spin excitations of the initial condensate in the $|0\rangle$ Zeeman sublevel for both spin-1 and spin-2 ^{87}Rb spinor BECs. This spectrum is particularly interesting to understand the instability associated to the spinor dynamics that are characterized by the correlated pair creation into $|\pm 1\rangle$ from the BEC in $|0\rangle$, which closely resembles the parametric amplification in quantum optics. We consider a homogeneous case and derive the Hamiltonian in the linear regime, without considering dipolar or magnetic gradient effects. We determine the Bogoliubov spectrum for different quadratic Zeeman effect q and show that the different stability and instability regimes of the BEC in $|0\rangle$. In particular, we focus on the unstable regime and determine the instability rate, which is obtained from the most unstable Bogoliubov spin excitation mode.

In chapter 3 we continue the investigation of the first stages of the spinor dynamics (linear regime), but now for trapped spin-1 and spin-2 spinor BECs. As in the previous chapter, we analyze the Bogoliubov spectrum and determine the instability rate as a function of the applied magnetic field. This instabilty rate shows an intriguing non-monotonous character which is crucially determined by the trap inhomogeneity and cannot be explained from the physics of homogeneous spinor BEC discussed in chapter 2. We then analyze the pair creation dynamics, which is characterized by the exponential

growth of the most unstable spin excitations of the initial BEC in $|0\rangle$. This pair creation efficiency (from $|0\rangle$ to $|\pm 1\rangle$) presents a striking multi-resonant magnetic field dependence, which maps the instability rate. We also calculate the population growth in $|\pm 1\rangle$ using the mean-field coupled GPEs, however, this result fails to reproduce the high magnetic field resonance resulting from the exact quantum calculations in the linear regime. In the final part of the chapter, we compare our results to the experiments performed in Hannover, showing an excellent agreement between theory and experiment.

In chapter 4 we study the triggering mechanism of the amplification. We show that the classical seed, very few spurious atoms in $|\pm 1\rangle$, plays only a relevant role at sufficiently low magnetic fields, where the amplified spin excitation mode has a large overlap with the original BEC. However, at larger magnetic fields the amplified spin excitations show pronounced spatial structures and lack a substantial overlap. As a result, our results show that the amplification is dominantly triggered by vacuum fluctuations. In the final part of the chapter, We directly compare our results with the experimental ones in Hannover university and show pretty good agreement.

In chapter 5 we analyze the sensitivity of the amplification to the magnetic dipole-dipole interactions. We show that the amplification is largely modified when changing the relative orientation between the applied magnetic field and the trap axis. If these directions are perpendicular to each other the amplification dynamics is much faster than for the parallel configuration. We also analyze in detail the effects of magnetic field gradients in the amplification dynamics. We show that these gradients modify also largely the amplification process and must be carefully controlled, since uncontrolled gradients may obscure the expected DDI effects. Finally we comment on experimental requirements for observing the magnetic dipole-dipole interaction effects on the amplification dynamics.

Chapter 6 is devoted to the study of the nature of the symmetry breaking during the amplification of quantum spin fluctuations, studied in Ch. 4. Interestingly, a twofold spontaneous breaking of spatial and $+1$ and -1 spin symmetries may occur. On one hand, we show that quantum fluctuations of the relative phase between amplified degenerate spin modes may break the cylindrical symmetry imposed by the trap. On the other hand, the density profiles in $|+1\rangle$ and $|-1\rangle$ may differ from each other, leading to spontaneously formed longitudinal magnetization patterns only if various nondegenerate spin modes are significantly amplified. We show that this novel type of spin-symmetry breaking is linked to quantum interferences occurring during the amplification process. In the final part of the chapter, we show that our results are in qualitative agreement with the experiments in Hannover university.

Bogoliubov Analysis

A particularly interesting scenario for spinor condensates is provided by BECs initially prepared in the $m = 0$ Zeeman sublevel ($|0\rangle$), since spin-changing collisions acting upon this level may induce, as throughly discussed in this Thesis, the equivalent of parametric down conversion into $m = \pm 1$ sublevels ($\pm 1\rangle$). In this chapter we analyze the first stages of this spinor dynamics (linear regime), focusing on the properties of the Bogoliubov spectrum of spin excitations of the initial condensate in the $|0\rangle$ Zeeman sublevel for both spin-1 and spin-2 ^{87}Rb spinor BECs. This spectrum is particularly interesting to understand the instability associated to the spinor dynamics leading to the discussed parametric amplification. We concentrate in this chapter on the relatively simple homogeneous case, leaving the (experimentally relevant) discussion of the trapped case to the following chapter. We first derive the Hamiltonian in the linear regime (without considering dipolar or gradient effects, which are left to Chapter 5). We then diagonalize the linear Hamiltonian to obtain the corresponding Bogoliubov spectrum for different quadratic Zeeman energies, and finally analyze the different stability and instability regimes.

2.1   Linear Regime Hamiltonian

In the following we are interested in the first stages (linear regime) of the spinor dynamics of a spin-2 BEC initially prepared in the $|0\rangle$ sublevel, after quenching q into a possibly unstable regime. The initial scalar wavefunction $\psi_0(\vec{r})$ of the condensate and the corresponding chemical potential μ may be obtained using the time-independent Gross-Pitaevskii equation Eq. (1.11):

$$\left[-\frac{\hbar^2}{2M}\Delta + V(\vec{r}) + \left(c_0 + \frac{c_2}{5} \right) n_0(\vec{r}) \right] \psi_0(\vec{r}) = \mu \psi_0(\vec{r}), \qquad (2.1)$$

with $n_0(\vec{r}) = |\psi_0(\vec{r})|^2$, $\int d^3r |\psi_0(\vec{r})|^2 = N$ and N is the total number of particles.

The free energy of the spinor system is described by $\hat{K} = \hat{H} - \mu\hat{N}$, where $\hat{N} = \sum_m \int d^3r \hat{\psi}_m^\dagger(\vec{r})\hat{\psi}_m(\vec{r})$ is the total number operator of the system. Inserting Eq. (1.39) (without dipole-dipole interaction or magnetic field gradients)

we obtain

$$\hat{K} = \int d^3\vec{r} \sum_m \hat{\psi}_m^\dagger(\vec{r}) \left(-\frac{\hbar^2\nabla^2}{2M} + V(\vec{r}) + qm^2 - \mu \right) \hat{\psi}_m(\vec{r})$$

$$+ \frac{c_0}{2} \int d^3\vec{r} \sum_{mm'} \hat{\psi}_{m'}^\dagger(\vec{r}) \hat{\psi}_m^\dagger(\vec{r}) \hat{\psi}_{m'}(\vec{r}) \hat{\psi}_m(\vec{r})$$

$$+ \frac{c_1}{2} \int d^3\vec{r} \sum_{\vec{m}} \hat{\psi}_{m_4}^\dagger(\vec{r}) \hat{\psi}_{m_3}^\dagger(\vec{r}) \hat{\vec{F}}_{m_3 m_2} \cdot \hat{\vec{F}}_{m_4 m_1} \hat{\psi}_{m_2}(\vec{r}) \hat{\psi}_{m_1}(\vec{r})$$

$$+ \frac{c_2}{10} \int d^3\vec{r} \sum_{m,n} (-1)^{m+n} \hat{\psi}_m^\dagger(\vec{r}) \hat{\psi}_{-m}^\dagger(\vec{r}) \hat{\psi}_n(\vec{r}) \hat{\psi}_{-n}(\vec{r}). \qquad (2.2)$$

The first stages of the spinor dynamics of the spin-2 system initially prepared in $|0\rangle$ Zeeman sublevel may be described by means of a Bogoliubov approximation:

$$[\hat{\psi}_2(\vec{r},t), \hat{\psi}_1(\vec{r},t), \hat{\psi}_0(\vec{r},t), \hat{\psi}_{-1}(\vec{r},t), \hat{\psi}_{-2}(\vec{r},t)]^T = \left[(\boldsymbol{\Psi}_0(\vec{r}) + \delta\hat{\boldsymbol{\Psi}}(\vec{r},t))^T \right] e^{-i\mu t}.$$
$$(2.3)$$

where $\delta\hat{\boldsymbol{\Psi}}(\vec{r},t)^T = (\delta\hat{\psi}_2(\vec{r},t), \delta\hat{\psi}_1(\vec{r},t), \delta\hat{\psi}_0(\vec{r},t), \delta\hat{\psi}_{-1}(\vec{r},t), \delta\hat{\psi}_{-2}(\vec{r},t))^T$ are small fluctuations of the spinor field operator and $\boldsymbol{\Psi}_0(\vec{r})^T = (0, 0, \psi_0(\vec{r}), 0, 0)^T$ is the initial state of the condensate.

In this first stages of the spin evolution time, we may perform the following approximations:

- Small population in $|\pm 1\rangle$ components, such that the density of the fluctuations is much smaller than the density of the condensate, $n_0(\vec{r}) = |\psi_0(\vec{r})|^2 \gg \langle \delta\hat{\psi}_m^\dagger(\vec{r}) \hat{\psi}_m(\vec{r}) \rangle$.

- Keep terms up to the second order in $\delta\hat{\psi}_m(\vec{r})$, which means that we neglect the spin-collisions that involve only atoms in $|\pm 1\rangle$ Zeeman sublevels.

- When the above conditions are fulfilled, then there is no transfer of atoms from $|\pm 1\rangle$ in to $|\pm 2\rangle$, whereas the transfer rate from $|0\rangle$ in to $|\pm 2\rangle$ is much smaller that from $|0\rangle$ in to $|\pm 1\rangle$ (see Table 1.3). Therefore, we may neglect the transfer of atoms into $|\pm 2\rangle$ Zeeman sublevels during the first stages of the dynamics.

Employing these approximations, Eq. (2.2) takes the form

$$
\begin{aligned}
\hat{K} =& \int d^3\vec{r}\bigg\{(\psi_0 + \delta\hat{\psi}_0^\dagger)(-\frac{\hbar^2}{2M}\nabla^2 + V(\vec{r}) - \mu)(\psi_0 + \delta\hat{\psi}_0) \\
+& \delta\hat{\psi}_1^\dagger(-\frac{\hbar^2}{2M}\nabla^2 + V(\vec{r}) + q - \mu)\delta\hat{\psi}_1 + \delta\hat{\psi}_{-1}^\dagger(-\frac{\hbar^2}{2M}\nabla^2 + V(\vec{r}) + q - \mu)\delta\hat{\psi}_{-1}\bigg\} \\
+& \frac{c_0}{2}\int d^3\vec{r}\big\{4(\psi_0^* + \delta\hat{\psi}_0^\dagger)\delta\hat{\psi}_1^\dagger(\psi_0 + \delta\hat{\psi}_0)\delta\hat{\psi}_1 + 4(\psi_0^* + \delta\hat{\psi}_0^\dagger)\delta\hat{\psi}_{-1}^\dagger(\psi_0 + \delta\hat{\psi}_0)\delta\hat{\psi}_{-1} \\
+& (\psi_0^* + \delta\hat{\psi}_0^\dagger)(\psi_0^* + \delta\hat{\psi}_0^\dagger)(\psi_0 + \delta\hat{\psi}_0)(\psi_0 + \delta\hat{\psi}_0)\big\} \\
+& \frac{c_1}{2}\int d^3\vec{r}\bigg\{4(\psi_0^* + \delta\hat{\psi}_0^\dagger)\hat{\vec{F}}_{10}\cdot\hat{\vec{F}}_{01}\delta\hat{\psi}_1^\dagger(\psi_0 + \delta\hat{\psi}_0)\delta\hat{\psi}_1 + 4(\psi_0^* + \delta\hat{\psi}_0^\dagger)\delta\hat{\psi}_{-1}^\dagger \\
\times& \hat{\vec{F}}_{-10}\cdot\hat{\vec{F}}_{0-1}(\psi_0 + \delta\hat{\psi}_0)\delta\hat{\psi}_{-1} + (\psi_0^* + \delta\hat{\psi}_0^\dagger)(\psi_0^* + \delta\hat{\psi}_0^\dagger)\hat{\vec{F}}_{00}\cdot\hat{\vec{F}}_{00} \\
\times& (\psi_0 + \delta\hat{\psi}_0)(\psi_0 + \delta\hat{\psi}_0) + 2(\psi_0^* + \delta\hat{\psi}_0^\dagger)(\psi_0^* + \delta\hat{\psi}_0^\dagger)\hat{\vec{F}}_{01}\cdot\hat{\vec{F}}_{0-1}\delta\hat{\psi}_1\delta\hat{\psi}_{-1} \\
+& 2\delta\hat{\psi}_1^\dagger\delta\hat{\psi}_{-1}^\dagger\hat{\vec{F}}_{10}\cdot\hat{\vec{F}}_{-10}(\psi_0 + \delta\hat{\psi}_0)(\psi_0 + \delta\hat{\psi}_0)\bigg\} \\
+& \frac{c_2}{10}\int d^3\vec{r}\big\{-(\psi_0^* + \delta\hat{\psi}_0^\dagger)(\psi_0^* + \delta\hat{\psi}_0^\dagger)\delta\hat{\psi}_1\delta\hat{\psi}_1 - \delta\hat{\psi}_1^\dagger\delta\hat{\psi}_{-1}^\dagger(\psi_0 + \delta\hat{\psi}_0)(\psi_0 + \delta\hat{\psi}_0) \\
+& (\psi_0^* + \delta\hat{\psi}_0^\dagger)(\psi_0^* + \delta\hat{\psi}_0^\dagger)(\psi_0 + \delta\hat{\psi}_0)(\psi_0 + \delta\hat{\psi}_0)\big\}.
\end{aligned}
\tag{2.4}
$$

Using the values of $\hat{\vec{F}}_{m_3 m_2}\cdot\hat{\vec{F}}_{m_4 m_1}$ (see Appendix B) in Eq. (2.4), and after some calculation, we get

$$
\begin{aligned}
\hat{K} =& \int d^3\vec{r}\bigg\{\psi_0^*(-\frac{\hbar^2}{2M}\nabla^2 + V(\vec{r}) + \frac{1}{2}(c_0 + \frac{c_2}{5})n_0 - \mu)\psi_0 \\
+& \delta\hat{\psi}_0^\dagger(-\frac{\hbar^2}{2M}\nabla^2 + V(\vec{r}) + (c_0 + \frac{c_2}{5}) - \mu)\delta\hat{\psi}_0 + (\frac{c_0}{2} + \frac{c_2}{10})n_0(\delta\hat{\psi}_0^\dagger\delta\hat{\psi}_0^\dagger + \delta\hat{\psi}_0\delta\hat{\psi}_0) \\
+& \psi_0^*(-\frac{\hbar^2}{2M}\nabla^2 + V(\vec{r}) + (c_0 + \frac{c_2}{5})n_0 - \mu)\delta\hat{\psi}_0 \\
+& \delta\hat{\psi}_0^\dagger(-\frac{\hbar^2}{2M}\nabla^2 + V(\vec{r}) + (c_0 + \frac{c_2}{5})n_0 - \mu)\psi_0\bigg\} \\
+& \int d^3\vec{r}\bigg\{\sum_{m=\pm 1}\delta\hat{\psi}_m^\dagger(-\frac{\hbar^2}{2M}\nabla^2 + V(\vec{r}) + (c_0 + 3c_1)n_0 + q - \mu)\delta\hat{\psi}_m \\
& (3c_1 - \frac{c_2}{5})n_0(\delta\hat{\psi}_{-1}^\dagger\delta\hat{\psi}_1^\dagger + \delta\hat{\psi}_1\delta\hat{\psi}_{-1})\bigg\}.
\end{aligned}
\tag{2.5}
$$

In the above equation, the third and the fourth terms vanish due to the time-independent GPE (2.1). The first term of Eq. (2.5) is a constant, which is the free energy of the initial BEC. The second term describes the dynamics of the density and phase fluctuations $\delta\hat{\psi}_0(\vec{r})$ of the $|0\rangle$ BEC. Note that these fluctuations are decoupled from the spin fluctuations $\delta\hat{\psi}_{\pm 1}(\vec{r})$ in the linear

regime. The two last terms govern the dynamics of the spin fluctuations in $|\pm 1\rangle$, being the relevant terms in our further discussion. Note in particular that the last term clearly describes pair creation into $|\pm 1\rangle$.

Therefore, the effective Hamiltonian that describes pair creation of atoms into $|\pm 1\rangle$ Zeeman sublevels acquires the form:

$$
\hat{H}_{\pm 1} = \int d^3 \vec{r} \bigg\{ \sum_{m=\pm 1} \delta\hat{\psi}_m^\dagger(\vec{r}) \left[\hat{H}_{eff}(\vec{r}) + q \right] \delta\hat{\psi}_m(\vec{r})
$$
$$
+ U_{1-1} n_0(\vec{r}) \left[\delta\hat{\psi}_{-1}^\dagger(\vec{r}) \delta\hat{\psi}_1^\dagger(\vec{r}) + \delta\hat{\psi}_1(\vec{r}) \delta\hat{\psi}_{-1}(\vec{r}) \right] \bigg\}
\tag{2.6}
$$

with

$$
\hat{H}_{eff}(\vec{r}) = -\frac{\hbar^2}{2M} \nabla^2 + V_{eff}(\vec{r})
\tag{2.7}
$$

where $V_{eff}(\vec{r}) = V(\vec{r}) + (U_{00} + U_{1-1}) n_0(\vec{r}) - \mu$, with $U_{00} = c_0 + c_2/5$ and $U_{1-1} = 3c_1 - c_2/5$. Note that $V_{eff}(\vec{r})$ acts as an effective trapping potential for the $|\pm 1\rangle$ atoms on the top of the the condensate in the $|0\rangle$ Zeeman sublevel. Besides the optical trap and the chemical potential of the system, this effective trap contains the mean-field potential $(U_{00} + U_{1-1}) n_0(\vec{r})$, which originates from spin-preserving collisions of atoms in $|\pm 1\rangle$ with $|0\rangle$ atoms. Note that in the Thomas-Fermi regime $\mu = V(\vec{r}) + U_{00} n_0(\vec{r})$. In that regime, $V_{eff}(\vec{r}) = U_{1-1} n_0(\vec{r})$ within the BEC region, and $V_{eff}(\vec{r}) = V(\vec{r}) - \mu$ outside.

The second term of the Hamiltonian in Eq. (2.6) originates from spin-changing collisions, which convert atoms in the $|0\rangle$ BEC into pairs of atoms in $|\pm 1\rangle$ and vice-versa. Interestingly, this process resembles parametric down conversion in optical parametric amplifiers. Indeed, as it will be discussed below, if the condensate in $|0\rangle$ is unstable after the quench of the quadratic Zeeman energy q, then the spin-changing collisions lead to an exponential amplification of the population in the $|\pm 1\rangle$ Zeeman sublevels.

Note that the effective Hamiltonian of Eq. (2.6) can also describe the dynamics of spin-1 systems by using the appropriate coupling constants $U_{00} = (g_0 + 2g_2)/3$ and $U_{1-1} = (g_2 - g_0)/3$. Hence, in the remaining part of this chapter, our results are equally valid for both spin-1 and spin-2 ^{87}Rb.

2.2 Bogoliubov spin excitations

To develop a basic understanding of the spinor dynamics after quenching q, we consider small perturbations about the inital $|0\rangle$ BEC. In particular, we are interested in determining whether a given perturbation to the condensate will be stable or unstable, *i.e.*, whether it will evolve by simply accruing a phase over time, or by becoming exponentially amplified or de-amplified. This distinction is dictated by the properties of the spectrum of spin excitations of

the original condenstate, which we determine at this point. In the following, and for simplicity of our discussion at this point, we consider a homogeneous (i.e. non-trapped) case. In a homogenous system, whereby $V_{eff}(\vec{r})$ and $n_0(\vec{r})$ are constants and $\mu = U_{00}n_0$, it is natural to work in a momentum $(\vec{k})$ basis.

We express the effective Hamiltonian (2.6) in terms of $\hat{\Phi}_{\pm}(\vec{r}) = \frac{1}{\sqrt{2}}[\delta\hat{\psi}_1(\vec{r}) \pm \delta\hat{\psi}_{-1}(\vec{r})]$. It takes then the form $\hat{H}_{\pm 1} = \hat{H}_+ + \hat{H}_-$, where

$$\hat{H}_{\pm} = \int d^3\vec{r}\left\{\hat{\Phi}_{\pm}^{\dagger}(\vec{r})[\hat{H}_{eff} + q]\hat{\Phi}_{\pm}(\vec{r}) + \frac{\epsilon U_{1-1}n_0(\vec{r})}{2}[\hat{\Phi}_{\pm}^{\dagger}(\vec{r})\hat{\Phi}_{\pm}^{\dagger}(\vec{r}) + \hat{\Phi}_{\pm}(\vec{r})\hat{\Phi}_{\pm}(\vec{r})]\right\},$$
$$(2.8)$$

with $\epsilon = \pm$. The expressions for $\hat{H}_+$ and $\hat{H}_-$ has the same form except the value of ϵ. Thus, it is the same to solve either $\hat{H}_+$ or $\hat{H}_-$, and hence we drop the $\pm$ subindex in the remaining part of this discussion.

We may introduce the Fourier transform $\hat{\Phi}(\vec{r}) = \int \frac{d^3\vec{k}}{(2\pi)^{3/2}}e^{i\vec{k}\cdot\vec{r}}\hat{\Phi}(\vec{k})$, which allows us to write Eq. (2.8), in the simplified form:

$$\hat{H}_{\pm 1} = \int \frac{d^3\vec{k}}{(2\pi)^3}(\varepsilon_{\vec{k}} + q - q_{cr})\hat{\Phi}^{\dagger}(\vec{k})\hat{\Phi}(\vec{k})$$
$$- \frac{\epsilon q_{cr}}{2}\int \frac{d^3\vec{k}}{(2\pi)^3}[\hat{\Phi}^{\dagger}(\vec{k})\hat{\Phi}^{\dagger}(-\vec{k}) + \hat{\Phi}(\vec{k})\hat{\Phi}(-\vec{k}))],$$
$$(2.9)$$

where $q_{cr} = -U_{1-1}n_0$ is constant and $\varepsilon_k = \frac{\hbar^2 k^2}{2M}$. Note that for spin-1 and spin-2 ^{87}Rb $U_{1-1} > 0$ and $U_{1-1} < 0$, and hence $q_{cr} > 0$ and $q_{cr} < 0$, respectively.

The Hamiltonian for each $\vec{k}$ mode takes the form

$$\hat{H}_{\pm 1}(\vec{k}) = (\varepsilon_{\vec{k}} + q - q_{cr})\hat{\Phi}^{\dagger}(\vec{k})\hat{\Phi}(\vec{k}) - \frac{\epsilon q_{cr}}{2}[\hat{\Phi}^{\dagger}(\vec{k})\hat{\Phi}^{\dagger}(-\vec{k}) + \hat{\Phi}(\vec{k})\hat{\Phi}(-\vec{k})].\quad (2.10)$$

This Hamiltonian may be easily diagonalized using the Bogoliubov transformation

$$\hat{O}(\vec{k}) = u_{\vec{k}}\Phi(\vec{k}) + v_{\vec{k}}\Phi^{\dagger}(-\vec{k}),\quad (2.11)$$

such that

$$\xi_{\vec{k}}\hat{O}(\vec{k}) = [\hat{O}(\vec{k}), \hat{H}_{\pm 1}(\vec{k})],\quad (2.12)$$

where $\xi_{\vec{k}}$ are the excitation energies. Using the Heisenberg equation along with the above commutation relation, it is easy to show that

$$i\hbar\frac{\partial\hat{O}(\vec{k})}{\partial t} = [\hat{O}(\vec{k}), \hat{H}_{\pm 1}(\vec{k})]$$
$$= \xi_{\vec{k}}u_{\vec{k}}\Phi(\vec{k}) + \xi_{\vec{k}}v_{\vec{k}}\Phi^{\dagger}(-\vec{k})$$
$$= (\varepsilon_k + q - q_{cr})[u_k\hat{\Phi}(\vec{k}) - v_k\hat{\Phi}^{\dagger}(-\vec{k})]$$
$$- \epsilon q_{cr}[u_k\hat{\Phi}^{\dagger}(-\vec{k}) - v_k\hat{\Phi}(\vec{k})].$$
$$(2.13)$$

One hence obtains the so-called Bogoliubov-de Gennes equations:

$$\begin{aligned}
\xi_{\vec{k}} u_{\vec{k}} &= (\varepsilon_{\vec{k}} + q - q_{cr}) u_{\vec{k}} + \epsilon q_{cr} v_{\vec{k}} \\
\xi_{\vec{k}} v_{\vec{k}} &= -(\varepsilon_{\vec{k}} + q - q_{cr}) v_{\vec{k}} - \epsilon q_{cr} u_{\vec{k}},
\end{aligned} \tag{2.14}$$

which may be expressed in the matrix form:

$$\begin{pmatrix} \varepsilon_{\vec{k}} + q - q_{cr} & \epsilon q_{cr} \\ -\epsilon q_{cr} & -(\varepsilon_{\vec{k}} + q - q_{cr}) \end{pmatrix} \begin{pmatrix} u_{\vec{k}} \\ v_{\vec{k}} \end{pmatrix} = \xi_{\vec{k}} \begin{pmatrix} u_{\vec{k}} \\ v_{\vec{k}} \end{pmatrix}. \tag{2.15}$$

We may hence calculate the eigenenergies and eigenstates of the spin excitations [90, 91]. After diagonalizing the above matrix, one obtains

$$\xi_{\vec{k}}^2 = (\varepsilon_{\vec{k}} + q - q_{cr})^2 - q_{cr}^2. \tag{2.16}$$

Note that the eigenenergies and eigenstates fulfill the condition:

$$(\xi_{\vec{k}} - \xi_{\vec{k}}^*)[|u_{\vec{k}}|^2 - |v_{\vec{k}}|^2] = 0, \tag{2.17}$$

which is particularly important in the following discussion.

Note that the eigenenergies may become imaginary, leading to the on-set of dynamical instability against an exponential amplification of the population in $|\pm 1\rangle$. Whether there is instability or not depends to a large extent on the quadratic Zeeman energy q. We focus at this point on this important issue.

2.2.1 Real eigenenergies

Real eigenvalues occur when when $(\varepsilon_{\vec{k}} + q - q_{cr}) > q_{cr}$. In that case one may proceed as for usual stable scalar condensates [69]. The quasi-particle operator $\hat{O}(\vec{k})$ is a bosonic operator; consequently the operator $\hat{O}(\vec{k})$ and $\hat{O}^\dagger(\vec{k})$ satisfy the Bose commutation relation, *i.e.*

$$[\hat{O}(\vec{k}), \hat{O}^\dagger(\vec{k})] = 1. \tag{2.18}$$

By imposing the above commutation rule, one finds that the amplitudes $u_{\vec{k}}$ and $v_{\vec{k}}$ must obey the normalization condition:

$$|u_{\vec{k}}|^2 - |v_{\vec{k}}|^2 = 1. \tag{2.19}$$

We can then choose one solution with amplitudes $u_{\vec{k}} = \cosh \frac{\gamma_{\vec{k}}}{2}$ and $v_{\vec{k}} = \sinh \frac{\gamma_{\vec{k}}}{2}$, such that

$$\tanh \gamma_{\vec{k}} = \frac{q_{cr}}{(\varepsilon_{\vec{k}} + q - q_{cr})}. \tag{2.20}$$

The eigenenergies corresponding to this state is given by

$$\xi_{\vec{k}} = \sqrt{(\varepsilon_{\vec{k}} + q - q_{cr})^2 - q_{cr}^2}. \tag{2.21}$$

The other possible eigenstate is $\begin{pmatrix} v^*_{\vec{k}} \\ u^*_{\vec{k}} \end{pmatrix}$ with eigenenergy $-\xi_{\vec{k}}$. Hence the Bogoliubov transformation for the above two possible solution is expressed as

$$
\begin{aligned}
\hat{O}_1(\vec{k}) &= u_{\vec{k}}\hat{\Phi}(k) + v_{\vec{k}}\hat{\Phi}^\dagger(-\vec{k}) = \hat{O}(\vec{k}) \\
\hat{O}_2(\vec{k}) &= v^*_{\vec{k}}\hat{\Phi}(\vec{k}) + u^*_{\vec{k}}\hat{\Phi}(-\vec{k}).
\end{aligned}
\tag{2.22}
$$

However, the operator $\hat{O}_2(\vec{k})$ does not fulfill the commutation relation, since

$$
[\hat{O}_2(\vec{k}), \hat{O}^\dagger_2(\vec{k})] = |v_{\vec{k}}|^2 - |u_{\vec{k}}|^2 = -1.
\tag{2.23}
$$

This is because the operator $\hat{O}_2(\vec{k})$ is actually the Hermitian conjugate of $u_{\vec{k}}\hat{\Phi}(-\vec{k}) + v_{\vec{k}}\hat{\Phi}^\dagger(\vec{k})$, which is the same as $\hat{O}_1(\vec{k})$ but in $-\vec{k}$. Therefore, we have

$$
\begin{aligned}
\hat{O}(\vec{k}) &= u_{\vec{k}}\hat{\Phi}(\vec{k}) + v_{\vec{k}}\hat{\Phi}^\dagger(-\vec{k}) \\
\hat{O}_2(\vec{k}) &= \hat{O}^\dagger(-\vec{k}).
\end{aligned}
\tag{2.24}
$$

Hence, using these bosonic operators the effective Hamiltonian, Eq. (2.9) becomes

$$
\begin{aligned}
\hat{H}_{\pm 1} = \int \frac{d^3\vec{k}}{(2\pi)^3} \Big\{ &[(\varepsilon_{\vec{k}} + q - q_{cr})^2 - q^2_{cr}]^{1/2}\hat{O}^\dagger(\vec{k})\hat{O}(\vec{k}) \\
&- \frac{1}{2}\big[\varepsilon_{\vec{k}} + q - q_{cr} - [(\varepsilon_{\vec{k}} + q - q_{cr})^2 - q^2_{cr}]^{1/2}\big] \Big\}
\end{aligned}
\tag{2.25}
$$

2.2.2   Imaginary eigenenergies

When $(\varepsilon_{\vec{k}} + q - q_{cr}) < q_{cr}$, the eigenenergies become imaginary. Hence, from Eq. (2.17) it follows that $|u_{\vec{k}}|^2 = |v_{\vec{k}}|^2$ and the operator $\hat{O}(\vec{k})$ cannot be a bosonic operator, but it has actually the form:

$$
\hat{O}(\vec{k}) = \bar{u}_{\vec{k}}[e^{iS_{\vec{k}}}\hat{\Phi}(\vec{k}) + e^{-iS_{\vec{k}}}\hat{\Phi}^\dagger(-\vec{k})]
\tag{2.26}
$$

with $u_{\vec{k}} = \bar{u}_{\vec{k}}e^{iS_{\vec{k}}}$ and $v_{\vec{k}} = \bar{u}_{\vec{k}}e^{-iS_{\vec{k}}}$, such that the amplitudes fulfills $|u_{\vec{k}}|^2 = |v_{\vec{k}}|^2$. The quantity $S_{\vec{k}}$ is a phase, which we evaluate in the following. Employing Eq. (2.26) into one of the equations of (2.14), we obtain

$$
\pm i|\xi_{\vec{k}}| = (\varepsilon_{\vec{k}} + q - q_{cr}) + \epsilon q_{cr}e^{-2iS_{\vec{k}}}
\tag{2.27}
$$

Thus, the phase $S_{\vec{k}}$, which will be discussed in more detail in Chapter 6, becomes

$$
\begin{aligned}
\sin 2S_{\vec{k}} &= \frac{\mp|\xi_{\vec{k}}|}{\epsilon q_{cr}} \\
\cos 2S_{\vec{k}} &= \frac{-(\varepsilon_{\vec{k}} + q - q_{cr})}{\epsilon q_{cr}}.
\end{aligned}
\tag{2.28}
$$

The Bogoliubov transformation for the possible energy eigenvalues of $\pm|\xi_{\vec{k}}|$ can be expressed as

$$\hat{O}_+(\vec{k}) = \bar{u}_{\vec{k}}[e^{iS_{\vec{k}}}\hat{\Phi}(\vec{k}) + e^{-iS_{\vec{k}}}\hat{\Phi}^\dagger(-\vec{k})]$$
$$\hat{O}_- = \bar{\bar{u}}_{\vec{k}}[e^{-iS_{\vec{k}}}\hat{\Phi}(\vec{k}) + e^{iS_{\vec{k}}}\hat{\Phi}^\dagger(-\vec{k})]. \tag{2.29}$$

Here one can easily see that the operators $\hat{O}_\pm(\vec{k})$ are not bosonic operators, rather they are quadratures that obey the following commutation relation:

$$[\hat{O}_+(\vec{k}), \hat{O}_-(\vec{k})] = i \tag{2.30}$$

with $\bar{u}_{\vec{k}} = \bar{\bar{u}}_{\vec{k}} = \frac{1}{\sqrt{2\sin 2S_{\vec{k}}}}$. We obtain hence the final form of the quadrature operators:

$$\hat{O}_+(\vec{k}) = \hat{\chi}(\vec{k}) = \frac{1}{\sqrt{2\sin 2S_{\vec{k}}}}[e^{iS_{\vec{k}}}\hat{\Phi}(\vec{k}) + e^{-iS_{\vec{k}}}\hat{\Phi}^\dagger(-\vec{k})]$$

$$\hat{O}_-(\vec{k}) = \hat{\wp}(\vec{k}) = \frac{1}{\sqrt{2\sin 2S_{\vec{k}}}}[e^{-iS_{\vec{k}}}\hat{\Phi}(\vec{k}) + e^{iS_{\vec{k}}}\hat{\Phi}^\dagger(-\vec{k})]. \tag{2.31}$$

The effective Hamiltonian, Eq. (2.9) takes thus the form

$$\hat{H}_{\pm 1} = \int \frac{d^3\vec{k}}{(2\pi)^3} \left(|\xi_{\vec{k}}| \left(\hat{\chi}(\vec{k})\hat{\wp}(\vec{k}) + \hat{\wp}(\vec{k})\hat{\chi}(\vec{k}) \right) - (\varepsilon_{\vec{k}} + q - q_{cr}) \right). \tag{2.32}$$

2.3 Magnetic field dependence of the instability rate

Whether the condensate in the $|0\rangle$ Zeeman sublevel is stable or unstable depends upon whether $\xi_{\vec{k}}$ is real or imaginary. If the imaginary part of $\xi_{\vec{k}}$ is positive for some $\vec{k}$, then the condensate in the $|0\rangle$ Zeeman sublevel is dynamically unstable and pair production to the $|\pm 1\rangle$ Zeeman sublevel occurs, as we shall discuss in the next chapter.

From Eq. (2.16) one may distinguish three different regimes as a function of q:

- If $q > q_{cr} + |q_{cr}|$ then $\xi_{\vec{k}}^2 > 0$ and $\xi_{\vec{k}}$ is real and hence the $|0\rangle$ condensate is stable.

- If $q_{cr} < q < q_{cr} + |q_{cr}|$ then $\xi_{\vec{k}}$ is imaginary, and the $|0\rangle$ BEC becomes dynamically unstable. The most unstable mode is characterized by $\vec{k}_{max} = 0$. The instability rate of the most unstable mode (which provides the amplification rate, as discussed in the following chapter) is given by $\Lambda(q) = \frac{|\xi_{\vec{k}_{max}=0}|}{h} = \sqrt{(q_{cr}^2 - (q - q_{cr})^2)}/h$, which is zero at $q = q_{cr} + |q_{cr}|$ and acquires its maximal value, $\frac{|\xi_{\vec{k}_{max}=0}|}{h}| = \frac{|q_{cr}|}{h}$ at $q = q_{cr}$, as shown in Fig. (2.1).

- If $q < q_{cr}$ the $|0\rangle$ BEC is also unstable, but the most unstable mode is characterized by a non-zero $\vec{k}$. The minimum value of $\xi^2_{\vec{k}_{max}} = -q^2_{cr}$ for a fixed value of q is obtained at $\varepsilon_{\vec{k}_{max}} = q_{cr} - q$, where $k_{max} = \sqrt{\frac{2M}{\hbar}(q_{cr} - q)}$ characterizes the most unstable mode. The corresponding instability rate is $\Lambda(q) = \frac{\xi_{k_{max}}}{h} = \frac{|q_{cr}|}{h}$, which remains constant (this will change in the presence of a trap as discussed in the following chapter).
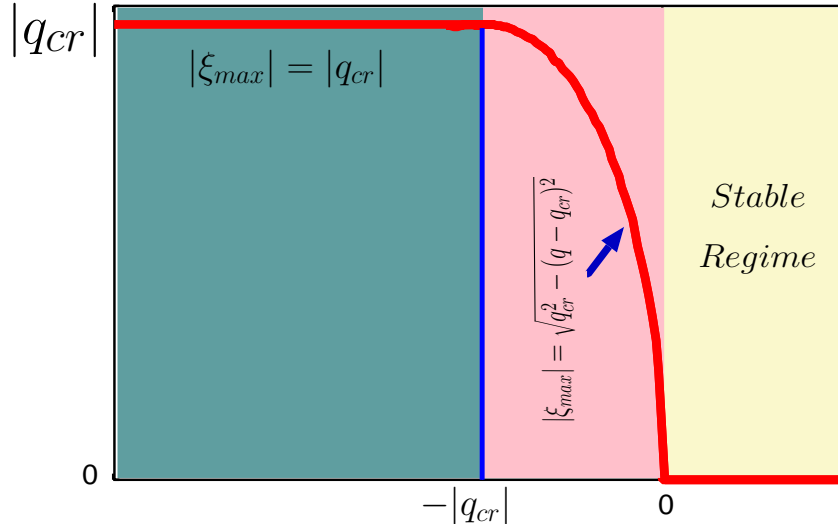
FIGURE 2.1: The largest instability rate of the homogenous system as a function of the quadratic Zeeman energy q. Note that for spin-2, since $U_{1-1} > 0$ then $q_{cr} < 0$. On the contrary for spin-1 $U_{1-1} < 0$, and $q_{cr} > 0$.

Multi-resonant parametric amplification in trapped spinor condensates

Spinor BECs provide exciting perspectives as novel sources of non-classical states of matter. In this sense, condensates initially prepared in the $|0\rangle$ Zeeman sublevel are especially fascinating [20, 21, 92, 93]. As mentioned in the previous chapter, the creation of correlated pairs results in the growth of macroscopic populations in the $|\pm 1\rangle$ Zeeman sublevel in a process which closely resembles parametric amplification in optical parametric down conversion [94], opening exciting new routes for matter-wave squeezing and atomic Einstein-Podolsky-Rosen entanglement experiments [38, 39].

Correlated pair creation, and in general any spinor dynamics, demands a significant rate of spin-changing collisions. In typical experiments these collisions are suppressed by the quadratic Zeeman effect (QZE) already in the presence of moderate magnetic fields [20]. However, the influence of the QZE at low fields is far from trivial [34, 92, 95–97]. In particular, spin-mixing can reach a pronounced maximum for low but finite fields [96]. This resonance, contrary to those discussed below, has a non-linear character and has been explained in terms of phase matching [96].

As we show in this chapter, the pair-creation efficiency reflects the confinement induced magnetic field dependence of the most unstable Bogoliubov spin excitations of the trapped condensate. In the first part of this chapter, we analyze the Bogoliubov spectrum along similar reasonings as those of the previous chapter, but introducing the crucial effects induced by the trapping potential. We determine the most unstable Bogoliubov mode, which provides the instability rate. This instability is shown to present an intriguing non-monotonous character which is crucially determined by the trap inhomogeneity and cannot be explained from the physics of homogeneous spinor BEC discussed in the previous chapter. In the second part of the chapter, we analyze the pair creation dynamics, which is characterized by the exponential growth of the most unstable spin excitations of the initial $|0\rangle$ BEC. As discussed below, the creation efficiency presents an striking multi-resonant magnetic field dependence. In the last part, we present mean-field results based on the coupled GPEs discussed in the introductory chapter, comparing the results with the exact quantum calculations in the linear regime.

3.1 Instability rate of Trapped system

Although the homogenous picture discussed in the previous chapter offers important insights, the actual q-dependence of the spinor dynamics in trapped condensates is strikingly different, showing that the confinement must be considered to obtain even a qualitative understanding. In the following two subsections, we first consider a box model to undestand the impact of the a finite confinement, and then we discuss the effects of the trap inhomogeneity for the experimentally relevant case of a harmonic trap.

3.1.1 Box potential trap

We consider at this point the simplified case of a spin-1 or spin-2 condensate in a box potential $V(\vec{r}) = 0$ for $r < R$, and $V(\vec{r}) = \infty$ otherwise. In the Thomas-Fermi regime the density n_0 of the condensate in the $|0\rangle$ Zeeman sublevel is approximately constant for $r < R$.

The analysis of the spinor dynamics is significantly simplified by considering the eigenfunctions and eigenenergies of $H_{eff}(\vec{r})$ in Eq. (2.7), $H_{eff}(\vec{r})\phi_n(\vec{r}) = \epsilon_n\phi_n(\vec{r})$. After projecting the bosonic field operator, $\delta\hat{\psi}_m(\vec{r})$, in the basis of these eigenstates:

$$\delta\hat{\psi}_m(\vec{r}) = \sum_n \phi_n(\vec{r})\hat{a}_{n,m}, \tag{3.1}$$

the effective Hamiltonian (2.6) for the pair creation of atoms in $|\pm 1\rangle$ Zeeman sublevels takes the form

$$\hat{H}_{\pm 1} = \sum_n (\epsilon_n + q)\big(\hat{a}_{n1}^\dagger\hat{a}_{n1} + \hat{a}_{n-1}^\dagger\hat{a}_{n-1}\big) + \sum_{nn'} A_{nn'}\big(\hat{a}_{n1}^\dagger\hat{a}_{n'-1}^\dagger + \hat{a}_{n1}\hat{a}_{n'-1}\big) \tag{3.2}$$

where $A_{nn'} = U_{1-1}\int d^3r\, n_0(\vec{r})\phi_n(\vec{r})\phi_{n'}(\vec{r})$ characterizes the effects of the short-range spin-changing collisions.

We may diagonalize the above Hamiltonian, Eq. (3.2), by applying the multimode Bogoliubov transformation:

$$\hat{\alpha}_\nu^\pm = \sum_n \big(u_{\nu n}^\pm\hat{a}_{n1} + v_{\nu n}^\pm\hat{a}_{n-1}^\dagger\big). \tag{3.3}$$

Using the notation $(\hat{a}_{n1}, \hat{a}_{n-1}^\dagger)^T := (\hat{a}_{11}, \hat{a}_{21}, ..., \hat{a}_{1-1}^\dagger, \hat{a}_{1-1}^\dagger, ...)^T$, we may rewrite Eq. (3.3) in a matrix form by means of a transformation matrix $\mathbf{M}$, which transforms the operators $(\hat{a}_{n1}, \hat{a}_{n-1}^\dagger)^T$ into $(\hat{\alpha}_\nu^+, \hat{\alpha}_\nu^-)^T$,

$$\begin{pmatrix} \hat{\alpha}_\nu^+ \\ \hat{\alpha}_\nu^- \end{pmatrix} = \underbrace{\begin{pmatrix} u_{\nu n}^+ & v_{\nu n}^+ \\ u_{\nu n}^- & v_{\nu n}^- \end{pmatrix}}_{\mathbf{M}} \begin{pmatrix} \hat{a}_{n1} \\ \hat{a}_{n-1}^\dagger \end{pmatrix}. \tag{3.4}$$

Where operator $\hat{\alpha}_\nu^\pm$ satisfy

$$\left[\hat{\alpha}_\nu^\pm, \hat{H}_{\pm 1}\right] = \lambda_\nu^\pm \hat{\alpha}_\nu^\pm. \tag{3.5}$$

Using the Heisenberg equation along with the above relation, we obtain

$$
\begin{aligned}
i\hbar \frac{\partial \hat{\alpha}_\nu^\pm}{\partial t} &= [\hat{\alpha}_\nu^\pm, \hat{H}_{\pm 1}] \\
&= \lambda_\nu^\pm u_{\nu n}^\pm \hat{a}_{n1} + \lambda_\nu^\pm v_{\nu n}^\pm \hat{a}_{n-1}^\dagger \\
&= \sum_{n'} \left\{ (\varepsilon_n + q)\delta_{nn'} \left[u_{\nu n}^\pm \hat{a}_{n'1} - v_{\nu n}^\pm \hat{a}_{n'-1}^\dagger \right] + A_{nn'} \left[u_{\nu n}^\pm \hat{a}_{n'-1}^\dagger - v_{\nu n}^\pm \hat{a}_{n'1} \right] \right\}.
\end{aligned}
\tag{3.6}
$$

This leads to the Bogoliubov-de Gennes equations

$$
\begin{aligned}
\lambda_\nu^\pm u_{\nu n}^\pm &= (\varepsilon_n + q)u_{\nu n}^\pm - \sum_{n'} A_{nn'} v_{\nu n'}^\pm \\
\lambda_\nu^\pm v_{\nu n}^\pm &= -(\varepsilon_n + q)v_{\nu n}^\pm + \sum_{n'} A_{nn'} u_{\nu n'}^\pm.
\end{aligned}
\tag{3.7}
$$

Note that in the Thomas-Fermi regime, the density n_0 and the chemical potential $\mu = U_{00}n_0$ are constants. As a consequence the effective trap $V_{eff} = U_{1-1}n_0 + V$ becomes a box shifted by $U_{1-1}n_0$. The eigenfunctions, $\phi_n(\vec{r})$, and eigenenergies, ε_n, are the usual eigenfunctions and eigenenergies of a box shifted by $U_{1-1}n_0$, i.e. $\varepsilon_n = U_{1-1}n_0 + \varepsilon'_n$ with ε'_n the energy of the nth-level of the box trap. In addition there is no coupling between different levels of the effective trap, i.e. $A_{nn'} = U_{1-1}n_0\delta_{nn'}$. Hence Eqs.(3.7) reduce to a 2×2 eigenproblem, which may be solved independently for each box level, leading to the eigenvalues

$$\lambda_n^2(q) = \left[(\varepsilon'_n - q_{cr} + q)^2 - q_{cr}^2 \right], \tag{3.8}$$

with $q_{cr} = -U_{1-1}n_0$, as in the previous chapter. Once more, if the imaginary part of the above eigenenergies is positive, $\text{Im}(\lambda_n(q)) > 0$, then the condensate in the $|0\rangle$ is dynamically unstable resulting into the correlated pair creation of atoms in the $|\pm 1\rangle$ Zeeman sublevels.

These energy eigenvalues are similar to the energy eigenvalues of the homogenous case (Eq. (2.16) in the previous chapter) except that not all the valus of $\vec{k}$ are possible. Note that the energy for the possible discrete set is given by the energy of the box potential $\varepsilon'_n = \frac{\hbar^2 k_0^2 n^2}{2M}$ with $n^2 = n_x^2 + n_y^2 + n_z^2$.

As for the case of the homogenous system, we obtain three different regimes that are classified according to the value of the q:

- If $q > q_{cr} + |q_{cr}|$ then the eigenenergies are real, $\lambda_n(q) > 0$, and hence the condensate in the $|0\rangle$ Zeeman sublevel is stable.

- If $q_{cr} < q < q_{cr} + |q_{cr}|$, the BEC is unstable and the most unstable mode is the ground state of the box trap ($n^2 = 3$). Similar to the homogenous case, the instability rate of this most unstable mode is given by

$$\Lambda(q) = \frac{|\lambda_n|}{h} = \frac{\sqrt{q_{cr}^2 - (q - q_{cr} + \varepsilon_0')^2}}{h}, \tag{3.9}$$

with ε_0' the ground-state energy of the box trap. This instability rate reaches its maximum, $\Lambda(q) = |q_{cr}|$, when $q = q_{cr} - \varepsilon_0'$ (see Fig. 3.1).

- If $q < q_{cr}$, the most unstable mode can be determined by the derivative of the energy eigenvalues (3.8). For clarity, let's introduce a parameter α^2, such that the energy eigenvalue is written as

$$\lambda_n^2(q) = \left[\left(\frac{\hbar^2 k_0^2 n^2}{2M} - \frac{\hbar^2 k_0^2 \alpha^2}{2M} \right)^2 - q_{cr}^2 \right], \tag{3.10}$$

with $q_{cr} - q = \hbar^2 k_0^2 \alpha^2 / 2M$. The condition for the minimal energy eigenvalues $\lambda_n^2(q)$ (i.e. the maximally unstable mode), is obtained from

$$\frac{\partial \lambda_n^2(q)}{\partial n^2} = 2 \left(\frac{\hbar^2 k_0^2}{2M} \right) (n^2 - \alpha^2) = 0 \tag{3.11}$$

This equation holds true when $n^2 = \alpha^2$. Since n^2 may only take some integer values, it then follows that the maximum instability rate occurs when $n_{min}^2 = [\alpha^2]$, where $[\alpha^2]$ is the closest integer to α^2 from the n^2 series. Therefore, the instability rate is given by

$$\Lambda(q) = \frac{\sqrt{q_{cr}^2 - \left(\frac{\hbar^2 k_0^2}{2M} \right)^2 \left([\alpha^2] - \alpha^2 \right)}}{h}. \tag{3.12}$$

This instability rate shows pronounced maxima and minima as in Fig. 3.1, reaching its maximum value, $\Lambda_{max}(q) = |q_{cr}|$, only when q is in resonance with the levels of the effective trap potential.
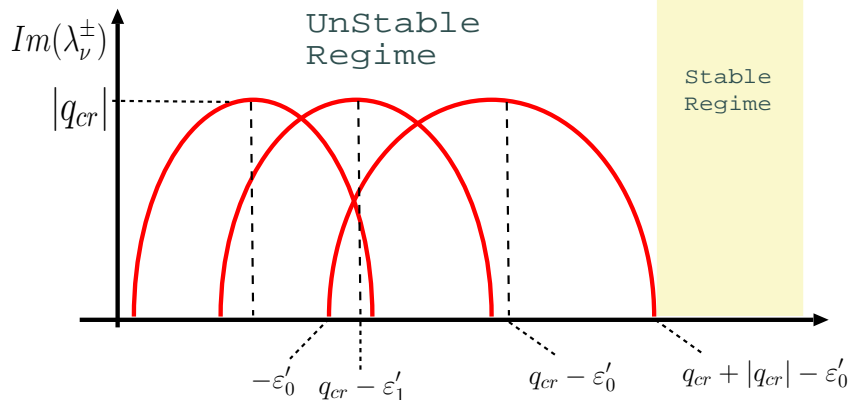
FIGURE 3.1: The imaginary part of the unstable modes for spin-1 and spin-2 ^{87}Rb with $q_{cr} > 0$ and $q > 0$ for spin-1 and $q_{cr} < 0$ and $q < 0$ for spin-2 respectively.

Fig. (3.2) shows the maximum instability rate depending on the quadratic Zeeman energy energy q. For low q, the two regimes are similar to the homogenous case. However, the growth of the instability rate is not followed by a constant value for large quadratic zeeman energy $|q|$. On the contrary, $\Lambda(q)$ shows, as mentioned above, pronounced maxima for the values of $|q|$ resonant with the effective trap levels.
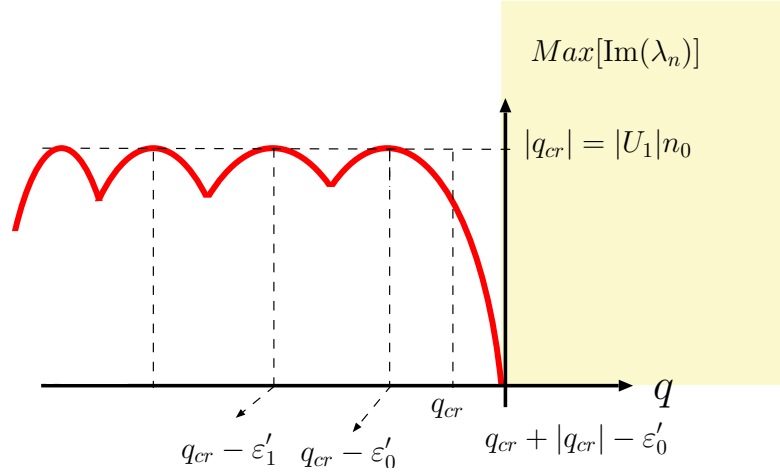
FIGURE 3.2: Maximal instability rate as a function of the quadratic Zeeman energy for spin-1 and spin-2 ^{87}Rb in a box trap. Unlike the homogenous case, this instability rate shows a pronounced maxima and minima.

3.1.2 Harmonic trap

For the actual experimental conditions not only the finite confinement but also the inhomogeneity of the potential and the related inhomogeneous Thomas-Fermi density profile $n_0(\vec{r})$ contribute to the instability properties. This in-

homogeneity of the potential trap and the inhomogeneity of the density $n_0(\vec{r})$ play actually a double role. First, the effective trap $V_{eff}(\vec{r})$ presents a non-trivial Mexican-hat-like form as shown in Fig. 3.3 (for spin-2 Rubidium, with $U_{1-1} > 0$). Second, contrary to the simplified box potential, there is a significant coupling ($A_{nn'}$) between the different trap levels, induced by the inhomogeneity of the density $n_0(\vec{r})$.
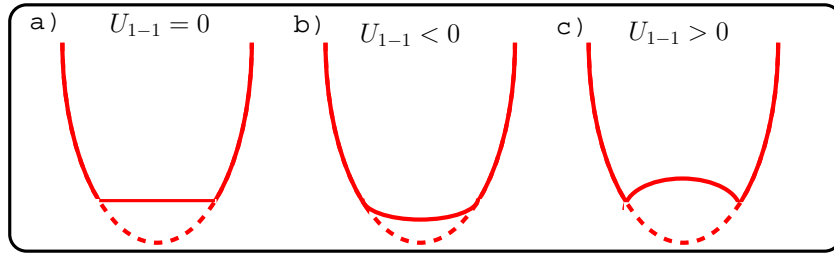
FIGURE 3.3:   a)- c) One-dimensional schematic representation of the effective potential $V_{eff}(\vec{r})$ for various interaction terms U_{1-1}
.

After diagonalizing Eq. (3.7) numerically, we obtain the spin Bogoliubov modes $\lambda_\nu(q)$. Figure (3.4), shows the magnetic-field dependence of the maximal instability rate $\Lambda(q) = \text{Max}|\text{Im}(\lambda_\nu(q))|/h$ for the experimental parameters of spin-2 ^{87}Rb with trap frequencies $(\omega_x, \omega_y, \omega_z) = 2\pi \times (176, 132, 46)$ Hz and atom number $N = 5 \times 10^4$. In the unstable regime with low $|q|$ we may approximate (following the discussion of the preceeding chapter) the maximal instability rate by $\Lambda(q) \simeq \sqrt{\bar{q}_{cr}^2 - (q - \bar{q}_{cr})^2}/h$ with an effective $\bar{q}_{cr}(\simeq -30$ Hz in Fig. (3.4)). However, as expected from the discussion above, this growth is not followed by a constant instability rate for large $|q|$. On the contrary, $\Lambda(q)$ shows pronounced maxima and minima.

This picture is rather general and may be applied to any other experiment on spinor condensates. In particular, Fig. (3.5) shows the maximum instability rate for recent experiments with spin-1 ^{87}Rb at Berkeley [93]. In the unstable regime, $q_{cr} < q < q_{cr} + |q_{cr}|$ (here $q_{cr} = 6Hz$), the maximal instability rate may be approximated by $\Lambda(q) \simeq \sqrt{q_{cr}^2 - (q - q_{cr})^2}/h$. This instability rate becomes constant for $0 < q < q_{cr}$. However, contrary to what may be expected from the simplified homogenous approximation, this instability rate does not remain constant, but rather it clearly decays for $q < 0$, in excellent agreement with the reported results in Ref. [93].
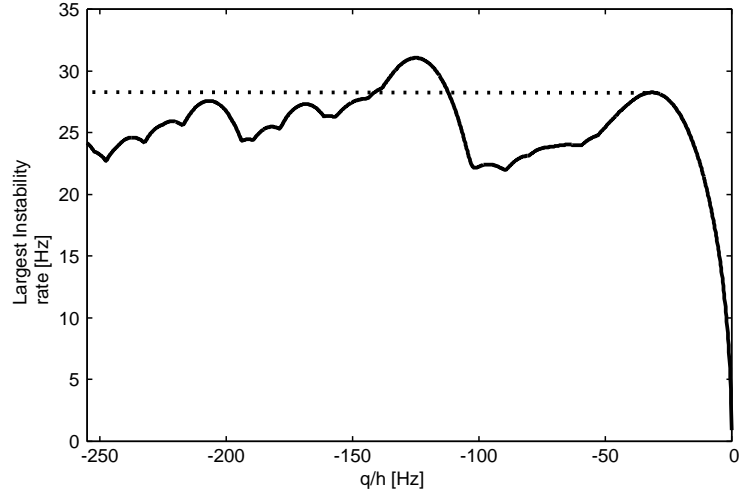
FIGURE 3.4: Instability rate as a function of the quadratic Zeeman energy q, given by the imaginary part of the most unstable spin Bogoliubov mode, corresponding to the trap frequencies $2\pi \times (176, 132, 46)$ Hz and $N = 5 \times 10^4$ particles. The maximal instability rate for an effective homogenous case (dashed line) lacks any resonant features

.
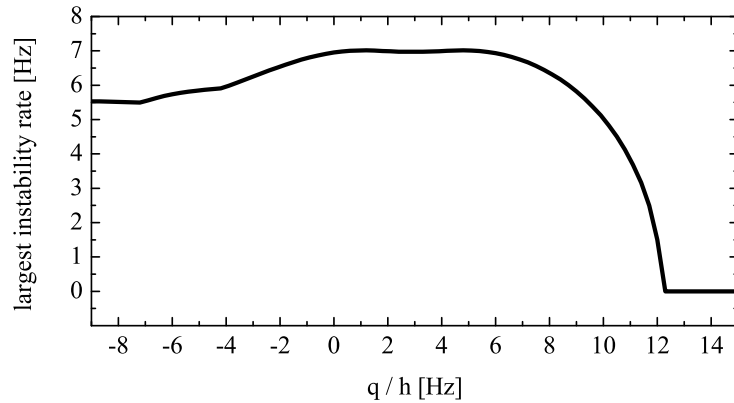
FIGURE 3.5: Instability rate as a function of the quadratic Zeeman energy for the parameters of Ref. [93], $(\omega_x, \omega_y, \omega_z) = 2\pi \times (440, 39, 4.2)$ Hz and $N = 2 \times 10^6$ atoms. A constant maximal instability rate for $0 < q < 6$ Hz is followed by a significant decay of the conversion efficiency for $q < 0$.

The maxima and minima of the instability rate depend on the non-trivial interplay between the quadratic Zeeman energy q, the spin changing collisions, and the finiteness and inhomogeneity of both the trapping potential and the atomic density of the condensate in the $|0\rangle$ Zeeman sublevel. Fig. (3.6) shows how the nontrivial interplay between the different energy scales changes the maximal instability rate by considering different possible experimental parameters of spin-2. This change is sensitive to the details of the trap frequencies,

the atomic number and the scattering lengths. In Fig. (3.6b) we consider two different sets of scattering lengths of $a_0 = 87.685a_B$ (with a_B the Bohr radius), $a_2 = 91.049a_B$, and $a_4 = 99.197a_B$ [1], and $a_0 = 89.4a_B$, $a_2 = 94.5a_B$, and $a_4 = 106.0a_B$ [2]. Although the difference in the spin-changing interaction energies between these two sets of scattering lengths is rather small, it leads to a small change in the potential bump of the effective trap, leading to different instability rates and a quite different pair creation efficiency at the resonances.
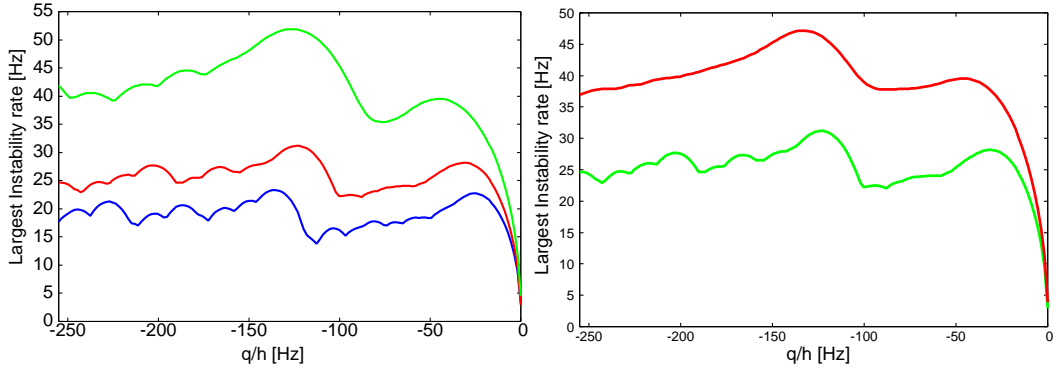
(A) instability rate for possible different trap frequencies and number of particles

(B) instability rate for different scattering lengths with the same number of particles and trap frequency

FIGURE 3.6: Instability rate as a function of the quadratic Zeeman energy for different experimental parameters. Fig. (3.6a) corresponds to $N = 5 \times 10^4$ number of particles with two different trap frequencies of $2\pi \times (176, 132, 46)$ Hz (red curve) and $2\pi \times (179, 179, 85)$ Hz (green curve) and the blue one corresponds to $N = 3 \times 10^4$ particles with trap frequencies of $2\pi \times (176, 132, 46)$ Hz. In both cases the scattering lengths are $a_0 = 87.685a_B, a_2 = 91.049a_B, a_4 = 99.197a_B$. Fig. (3.6b) corresponds to the trap frequency of $2\pi \times (176, 132, 46)$ Hz , $N = 5 \times 10^4$ number of particles with two different set of scattering lengths: $a_0 = 89.4a_B, a_2 = 94.5a_B, a_4 = 106.0a_B$ (red curve) and $a_0 = 87.685a_B, a_2 = 91.049a_B, a_4 = 99.197a_B$ (green curve).

3.2 Transfer of atoms into $|\pm 1\rangle$ Zeeman sublevel

In this section we study the dynamics of the exponential population growth in $|\pm 1\rangle$, i.e. we are interested in the time evolution of $\delta\hat{\psi}_{\pm 1}(\vec{r}, t)$. To this end, we follow a similar reasoning as that employed for obtaining the instability rates, i.e. we diagonalize the effective Hamiltonian (3.2) using the multimode Bogoliubov transformation (3.3). The time evolution of the quasi-particle

---

[1] Recent estimation of Prof. E. Tiemann, private communication.

[2] PhD Thesis of Holger Schmaljohann, Univ. Hamburg 2004

operators $\hat{\alpha}_\nu^\pm(t)$ is hence given by the Heisenberg equation

$$i\hbar \frac{d}{dt} \hat{\alpha}_\nu^\pm = \left[\hat{\alpha}_\nu^\pm, \hat{H}_{\pm 1} \right], \tag{3.13}$$

which using Eq. (3.5) leads to

$$\hat{\alpha}_\nu^\pm(t) = \hat{\alpha}_\nu^\pm(0) e^{-i\lambda_\nu^\pm t/\hbar}. \tag{3.14}$$

Hence, when the imaginary part of the energies $\lambda_\nu^\pm$ is positive, $\mathrm{Im}(\lambda_\nu^\pm) > 0$, the amplitude of the quasiparticles grows exponentially, leading to the exponential population growth in $|\pm 1\rangle$.

Using Eqs. (3.4) and (3.14) we obtain

$$\begin{bmatrix} \hat{a}_{n1}(t) \\ \hat{a}_{n-1}^\dagger(t) \end{bmatrix} = \mathbf{U}(t) \begin{bmatrix} \hat{a}_{n1}(0) \\ \hat{a}_{n-1}^\dagger(0) \end{bmatrix}, \tag{3.15}$$

with $\mathbf{U}(t) = \mathbf{M}^{-1} e^{-i\mathbf{\Lambda} t/\hbar} \mathbf{M}$ where $\mathbf{\Lambda} = \mathrm{diag}(\lambda_1^+, \lambda_2^+, ..., \lambda_1^-, \lambda_2^-, ...)$ is a diagonal matrix with the eigenenergies $\lambda_\nu^\pm$ in the diagonal, and $\mathbf{M}$ is defined in Eq. (3.4).

As mentioned above, the atoms are initially prepared in the $|0\rangle$ Zeeman sublevel. However, a slightly imperfect preparation may lead to a non-zero population of N_s atoms in $|\pm 1\rangle$. These spurious atoms are called from this point on the *classical seed*. Since they are produced at a single-particle level (due to e.g. not fully perfect radio-frequency transitions), the seed atoms in $|\pm 1\rangle$ occupy the same wave function as the BEC in $|0\rangle$ state, $\chi_0 = \psi_0/\sqrt{N}$, i.e. the initial state is given by $\chi_0(\sqrt{N_s}, \sqrt{N}, \sqrt{N_s})^T$. We need to know the effect of the operators $\hat{a}_{n\pm 1}$ on the states

$$(\chi_0|\pm 1\rangle)^{\otimes N_s} = \frac{1}{N_s!} \left(\hat{a}_{\chi\pm 1}^\dagger \right)^{N_s} |\mathrm{vac.}\rangle, \tag{3.16}$$

where $\hat{a}_{\chi\pm 1}^\dagger = \sum_n \chi_n \hat{a}_{n\pm 1}^\dagger$, with $\chi_n = \int d^3r \phi_n \chi_0$, creates one particle in single-particle state $\chi_0|\pm 1\rangle$. One finds

$$\hat{a}_{n\pm 1} (\chi_0|\pm 1\rangle)^{\otimes N_s} = \sqrt{N_s} \chi_n (\chi_0|\pm 1\rangle)^{\otimes (N_s-1)}. \tag{3.17}$$

We may then easily express the population $P_m(t) = \sum_n \langle \hat{a}_{n,m}^\dagger \hat{a}_{n,m} \rangle$ in the $m = \pm 1$ state, using Eqs. (5.21) and Eq. (3.17) as

$$P_{\pm 1}(t) = N_s \vec{\chi} \cdot \left(\mathbf{O}^\dagger \mathbf{O} + \widetilde{\mathbf{O}}^\dagger \widetilde{\mathbf{O}} \right) \cdot \vec{\chi} + \mathrm{trace} \left(\widetilde{\mathbf{O}}^\dagger \widetilde{\mathbf{O}} \right) \tag{3.18}$$

where the matrices $\mathbf{O}$ and $\widetilde{\mathbf{O}}$ are the upper left and upper right part of the time evolution matrix $\mathbf{U}(t)$ and $\vec{\chi} := (\chi_1, \chi_2, ...)^T$.

As for the instability rate, we first consider the simplified case of a box trap to gain some qualitative undestanding. In a box trap, the time evolution matrix $\mathbf{U}(t)$ decomposes into 2×2 matrices of the form

$$\mathbf{U}(t) = \begin{bmatrix} U_{11}^{(n)}(t) & U_{12}^{(n)}(t) \\ U_{21}^{(n)}(t) & U_{22}^{(n)}(t) \end{bmatrix} \tag{3.19}$$

where the matrices $U^{(n)}$ can be calculated independently. To calculate the population in $|\pm 1\rangle$, we evaluate the time evolution of $\hat{a}_{n1}(t)$ and $\hat{a}_{n-1}(t)$ and sum up for all the box levels. For each box level, $\hat{a}_{n1}(t)$ and $\hat{a}_{n-1}(t)$ can be written in terms of the matrices as

$$\hat{a}_{n1}(t) = U_{11}^{(n)} \hat{a}_{n1}(0) + U_{12}^{(n)} \hat{a}_{n-1}^{\dagger}(0) \quad \text{and}$$
$$\hat{a}_{n-1}(t) = U_{22}^{(n)*} \hat{a}_{n-1}(0) + U_{12}^{(n)*} \hat{a}_{n1}^{\dagger}(0). \tag{3.20}$$

After some calculations the matrices $U^{(n)}$ turn out to be

$$U_{11}^{n} = e^{\operatorname{Im}(\lambda_n^+)\, t/\hbar} \frac{(\sinh \theta_n + i)}{2i} = U_{22}^{n\,*},$$
$$U_{12}^{n} = e^{\operatorname{Im}(\lambda_n^+)\, t/\hbar} \frac{\cosh \theta_n}{2i} = U_{21}^{n\,*} \tag{3.21}$$

with $\coth \theta_n = \frac{U_1 n_0}{\varepsilon_n + U_1 n_0 + q}$.

Employing these expressions into Eq. (3.20), it then follows that

$$\hat{a}_{n1}(t) = \frac{e^{\operatorname{Im}(\lambda_n^+)\, t/\hbar}}{2i} \left[(\sinh \theta_n + i)\hat{a}_{n1}(0) + \cosh \theta_n \hat{a}_{n-1}^{\dagger}(0) \right]$$
$$- \frac{e^{-\operatorname{Im}(\lambda_n^+)\, t/\hbar}}{2i} \left[(\sinh \theta_n + i)\hat{a}_{n1}(0) + \cosh \theta_n \hat{a}_{n-1}^{\dagger}(0) \right]$$

and $\tag{3.22}$

$$\hat{a}_{n-1}(t) = \frac{e^{\operatorname{Im}(\lambda_n^+)\, t/\hbar}}{2i} \left[(\sinh \theta_n + i)\hat{a}_{n-1}(0) + \cosh \theta_n \hat{a}_{n1}^{\dagger}(0) \right]$$
$$- \frac{e^{-\operatorname{Im}(\lambda_n^+)\, t/\hbar}}{2i} \left[(\sinh \theta_n + i)\hat{a}_{n-1}(0) + \cosh \theta_n \hat{a}_{n1}^{\dagger}(0) \right].$$

After a sufficiently large evolution time, the pair creation is dominated by the most unstable mode (λ_0^+) and hence, the population of the $|\pm 1\rangle$ components evolves in the form

$$P_{\pm 1}(t) = 2N_s \sum_n \chi_n^2 \left[\frac{U_{1-1} n_0}{2|\lambda_n^+|} \right]^2 e^{2\operatorname{Im}(\lambda_n^+)\, t/\hbar} + \sum_n \left[\frac{U_{1-1} n_0}{2|\lambda_n^+|} \right]^2 e^{2\operatorname{Im}(\lambda_n^+)\, t/\hbar}. \tag{3.23}$$

The first term in Eq. (3.23), which is proportional to N_s, constitutes the contribution to the population growth triggered by the classical seed. On

the contrary the second term exists even if $N_s = 0$, being induced by purely quantum triggering. The latter term will be discussed in much further detail in the next chapter.

One sees that the population of the $|\pm 1\rangle$ components grows exponentially $\propto e^{2\,\mathrm{Im}(\lambda_n^+)\,t/\hbar}$. Therefore the population growth is resonantly enhanced, at the levels of the box, i. e. when $q = -U_1 n_0 - \varepsilon_n$, whereby the maxima of the instability landscape are located. As expected from our discussion of the instability rate, one sees that the population $P_{\pm 1}(t) = N_s$ remains stationary in the stable region $q > q_{cr} + |q_{cr}|$.

Similarly the instability rate of a harmonically trapped system has a pronounced maxima and minima landscape that leads to a strongly enhanced or reduced pair-creation efficiency into $|\pm 1\rangle$ components due to the exponential nature of the growth. Fig. 3.7 shows the population growth in $|\pm 1\rangle$ for the parameters of Fig. 3.4. The maxima and minima of the pair-creation efficiency in Fig. 3.7 are exactly at the predicted positions of maxima and minima of the instability rare in Fig. 3.4. However, the strength of the resonances and the absolute population are not totally as expected from the instabilitiy rate, whereby the strength of the resonance is smaller for small $|q|$ than for larger $|q|$. This is because the strength of the resonance is not only determined by the growth rate but also by the initial condition, which will be discussed in detail in the next chapter.
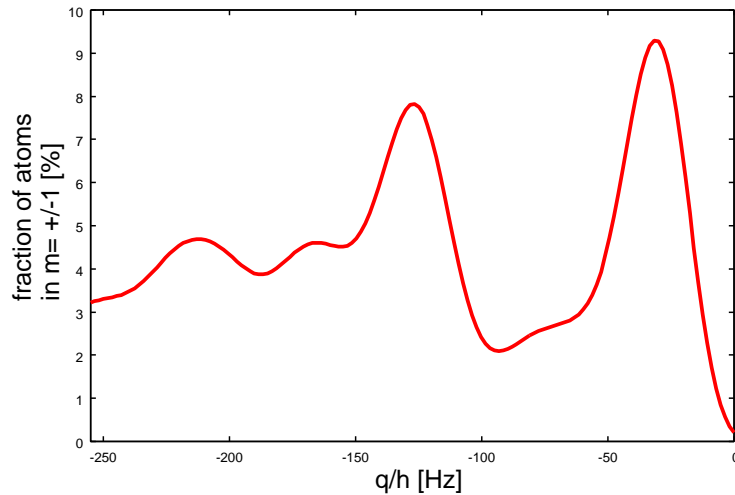
FIGURE 3.7: Fraction of atoms transferred into either $|m = +1\rangle$ or $|m = -1\rangle$ components as a function of the quadratic Zeeman energy q. This fraction of atoms is obtained from the ratio of the number of transferred atoms into $|m = \pm 1\rangle$ component to the total number of atoms in the condensate $|m = 0\rangle$. The positions of the maxima and minima on the resonance curve are exactly at the positions of the maxima and minima of the instability rate in Fig. (3.4).

3.3   Atom losses

In actual experiments with ^{87}Rb $F = 2$, it is important to take into account the possibility of hyperfine changing collisions, which lead to a decay into $F = 1$, introducing atom losses. We discuss at this point how this loss channel is taken into account in our calculations.

We focus only on the relevant losses within the linear regime, i.e. losses stemming from the collisions of atoms in the condensate and collisions of atoms in $| \pm 1 \rangle$ with the $|0\rangle$ condensate. These losses modify the spinor dynamics, since the instantaneous spin Bogoliubov modes change. As a consequence, the maxima in the transfer rate shift slightly from those expected without losses. Moreover, these losses slow down significantly the spinor dynamics. Thus one has to take into account these losses in our calculations.

We describe the losses in the form [21, 98, 99]

$$n_m(\vec{r}, t) = n_m(\vec{r}, t = 0) \exp\left(-\Gamma t\right), \tag{3.24}$$

with $\Gamma = \gamma \bar{n}_0(t)$, where $\bar{n}_0(t)$ is the average density, and the rate γ is obtained from an experimental fit.

To incorporate the effect of these losses, we define μ_0 as the chemical potential obtained before starting the dynamics. Thus, the initial wave function of the condensate at any time t can be written as $\psi_0(\vec{r}, t) = \psi_0(\vec{r}, t)e^{-i\mu_0 t/\hbar}$. The crucial point is that now the wave function of the condensate $\psi_0(\vec{r}, t) = \sqrt{n_0(\vec{r}, t)}e^{-i\vartheta(\vec{r}, t)}$ is a complex number, due to the losses. Since the losses are considered small, then $\vartheta(\vec{r}, t)$ evolves slowly compared to $\mu_0 t$. Thus, we define $\delta\hat{\psi}_m(\vec{r}, t) = \delta\hat{\psi}_m(\vec{r}, t)e^{-i\mu_0 t/\hbar}$. Then one obtains as before H_{eff}, but with an extra term $2U_{10}\big(n_0(\vec{r}, t) - n_0(\vec{r}, 0)\big)$. This term has a much slower energy than μ_0 and hence leads to a slower evolution and a slight shift in the positions of the instability maxima and minima.

Employing Eq. (3.24) into Eq. (3.7), we obtain

$$\begin{bmatrix} (\epsilon_n + q)\delta_{nn'} + B_{nn'} & -A_{nn'} \\ A_{nn'} & -(\epsilon_n + q)\delta_{nn'} + B_{nn'} \end{bmatrix} \begin{pmatrix} u_{\nu n}^{\pm} \\ v_{\nu n}^{\pm} \end{pmatrix} = \lambda_{\nu}^{\pm} \begin{pmatrix} u_{\nu n}^{\pm} \\ v_{\nu n}^{\pm} \end{pmatrix}. \tag{3.25}$$

Where $B_{nn'} = \int d^3r \, 2U_{10}[n_0(\vec{r}, t) - n_0(\vec{r}, 0)]\phi_n(\vec{r})\phi_{n'}(\vec{r})$ and $A_{nn'} = \int d^3r U_{1-1}n_0(\vec{r}, t)e^{-2i\vartheta(\vec{r}, t)}\phi_n(\vec{r})\phi_{n'}(\vec{r})$. Note that the terms $B_{nn'}$ and $A_{nn'}$ are now time dependent, leading to an instanteneous change of the spin Bogoliubov modes.
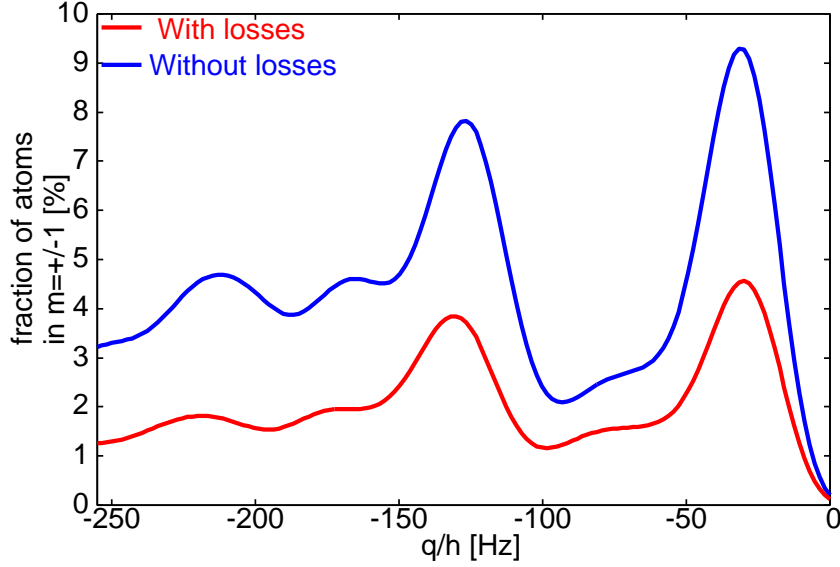
FIGURE 3.8: Fraction of atoms, with and without losses, transferred into $|m = \pm 1\rangle$ as a function of the quadratic Zeeman energy q. To obtain this fraction, the number of transferred atoms per state was divided by the total number of atoms in the condensate $|m = 0\rangle$ at 22.5 ms. we consider a loss rate $\gamma = 10^{-3} m^3 s^{-1}$.

Fig. (3.8) shows the population growth of the $|\pm 1\rangle$ components for the parameters of Fig. (3.4) with a loss rate $\gamma = 10^{-3} m^3 s^{-1}$. Note that the strength of the population growth decreases by approximately 40% compared to case without losses for the same parameters, showing once more that a small decrease in the instability rate leads to a large exponential decrease in the strength of the population growth.

3.4 Gross-Pitaevskii equation (GPE)

As mentioned in the introductory chapter, we may study the time evolution of the spinor BECs by means of coupled GPEs. This mean-field treatment, however, does not include by definition quantum fluctuations, a crucial drawback (compared to the exact Heisenberg equations discussed ebove) to explain key features of the experiments, as shown later on in this Thesis. In this section we discuss the numerical results coming from the coupled GPEs and compare them to the quantum results.

The coupled GPEs for a spin-2 BEC (in absence of dipole-dipole interac-

tions or magnetic field gradients) are:

$$
\begin{aligned}
i\hbar\frac{\partial \psi_m(\vec{r},t)}{\partial t} =& \left[-\frac{\hbar^2}{2M}\Delta + V(\vec{r}) + qm^2 + N(c_0 n + mc_1 f_z)\right]\psi_m(\vec{r},t) \\
&+ \frac{Nc_1}{2}\left[f_- S^+_{m,m-1}\psi_{m-1}(\vec{r},t) + f_+ S^-_{m,m+1}\psi_{m+1}(\vec{r},t)\right] \quad (3.26) \\
&+ \frac{2Nc_2}{5}(-1)^m S_- \psi^*_{-m}(\vec{r},t).
\end{aligned}
$$

As in actual experiments [3], we first prepare the ground state ψ_g to be in the $|2\rangle$ component using the imaginary-time propagation method. The spin polarized condensate is then transferred into the $|0\rangle$ component as an initial state. In order to simulate experimental imperfections in this population transfer, we assume a very small population in all the remaining four components, i.e. $\psi_m(\vec{r}, t = 0) = \sqrt{(N_s/N)}\psi_g$ with $m = \pm 2, \pm 1$ and N_s is the initial tiny number of seed particles, which will be discussed in detail in the next chapter. If all the atoms were initially in the $|0\rangle$ component ($N_s = 0$), it would then immediately follow from Eq. (3.26) that the other components ψ_m would remain zero during the subsequent time evolution. A seed is hence necessary in the coupled GPE approach. The time evolution of the system is obtained by numerically solving the coupled GPEs (3.26) in three dimensions with the Crank-Nicolson method.

We consider the same parameters as in Fig. (3.8) for our numerical calculations, i.e. a spin-2 ^{87}Rb BEC of $N(t = 0) = 5 \times 10^4$ atoms in a trap of frequencies $(w_x, w_y, w_z) = 2\pi(176, 132, 46)$ Hz with scattering lengths $a_0 = 87.685a_B, a_2 = 91.049a_B, a_4 = 99.197a_B$. We take into account the losses of atoms into Eq. (3.26) as discussed in the previous section. Thus, the number of particles in the GPE is now time dependent:

$$
N(t) = \int d^3r \sum_m n_m(\vec{r},t). \quad (3.27)
$$

Upon substituting the loss rate Eq. (3.24) into the above equation, we get

$$
N(t) = N(t = 0)e^{-\Gamma t}. \quad (3.28)
$$

Figure (3.9) shows the time evolution of the $|+2\rangle$ and $|+1\rangle$ components for the given parameters at a particular quadratic Zeeman energy $q = 29.92$ Hz. The $|+1\rangle$ component population grows exponential and reaches around 13%, whereas the population growth in the $|+2\rangle$ component remains around the seed population during the 28 ms evolution time, confirming the validity of neglecting the transfer of atoms into $|\pm 2\rangle$ during this evolution time, i.e. the time scale of the linear regime.

---

[3]PhD Thesis of Oliver Topič, Univ. of Hannover 2010 [100].
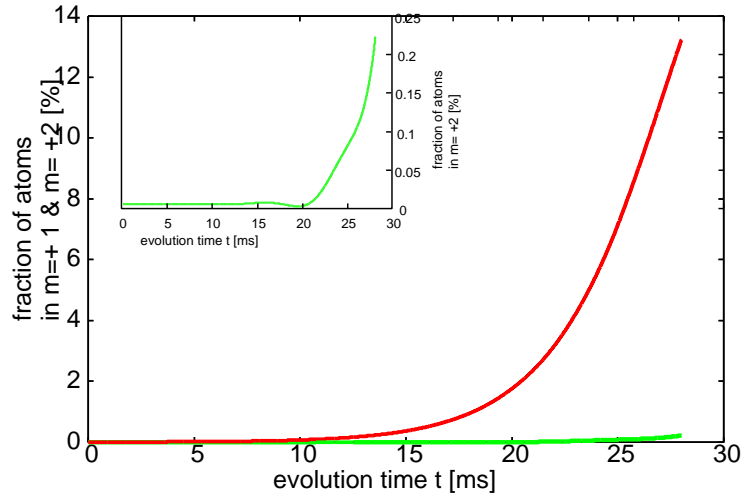
FIGURE 3.9: Fraction of atoms transferred into $m = +1$ (red colored line) and $m = +2$ (green colored line) components during 28 ms time of evolution. The inset shows the time evolution of the $m = +2$ component. In 28 ms evolution time an exponential growth in the $m = +1$ component is visible whereas there is no significant growth in the $m = +2$ component in this time scale.
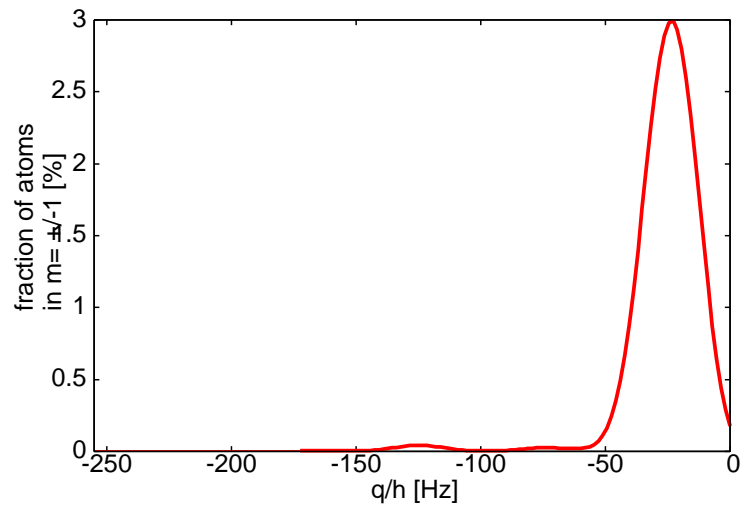
FIGURE 3.10: Fraction of atoms transferred into $|\pm 1\rangle$ components as a function of the quadratic Zeeman energy q during 22.5 ms evolution time. The high magnetic-field resonance is absent in the mean-field GPE calculation.

Figure (3.10) shows the population growth in $|\pm 1\rangle$ depending on the quadratic Zeeman energy q. This result clearly fails to reproduce the high magnetic-field resonance resulting from the quantum calculation in Fig. (3.8) for the same parameters. Note that the main difference is the lack of quantum fluctuations. This will be discussed in detail in the next chapter.

3.5   Comparison with experiments

Our results have been directly compared with experiments in a close collaboration with the experimental group leaded by Profs. J. Arlt and W. Ertmer at the Leibniz University of Hannover. As we have seen in the above discussions, slight differences in the instability rate are exponentially magnified in the pair-creation efficiency of atoms into $|\pm 1\rangle$. Hence to compare our results with the experimental results (see the PhD Thesis of O. Topič thesis [100] for more details concerning experiments), we have to focus on the exact values of the atomic density, trap frequencies, scattering lengths $a_{0,2,4}$ and the initial condition, which will be studied in the next chapter.

Here we consider experimental parameters: $N = 5 \times 10^4$ atoms, trap frequencies of $2\pi \times (176, 132, 46)$ Hz, and scattering lengths $a_0 = 87.685 a_B$, $a_2 = 91.049 a_B$, and $a_4 = 99.197 a_B$. The position of the maxima and minima of the observed pair creation efficiency in the experiments is in excellent agreement with the position of the calculated maxima and minima of the instability rate as in Fig. 3.11. However, as already mentioned, the evaluation of the resonance strength is more subtle. The experimentally observed resonance at low $|q|$ seems to be stronger than the one at high $|q|$, whereas the calculated instability rate is slightly smaller for the resonance at low $|q|$. As mentioned above, this is so because the absolute population is not only determined by the growth rate but also by the initial conditions. In fact, as we have seen in the derivation of the transfer rate, the resonant growth can be initiated by spuriously produced atoms in $|\pm 1\rangle$ and by vacuum spin fluctuations. These triggering mechanisms will be discussed in the next chapter.
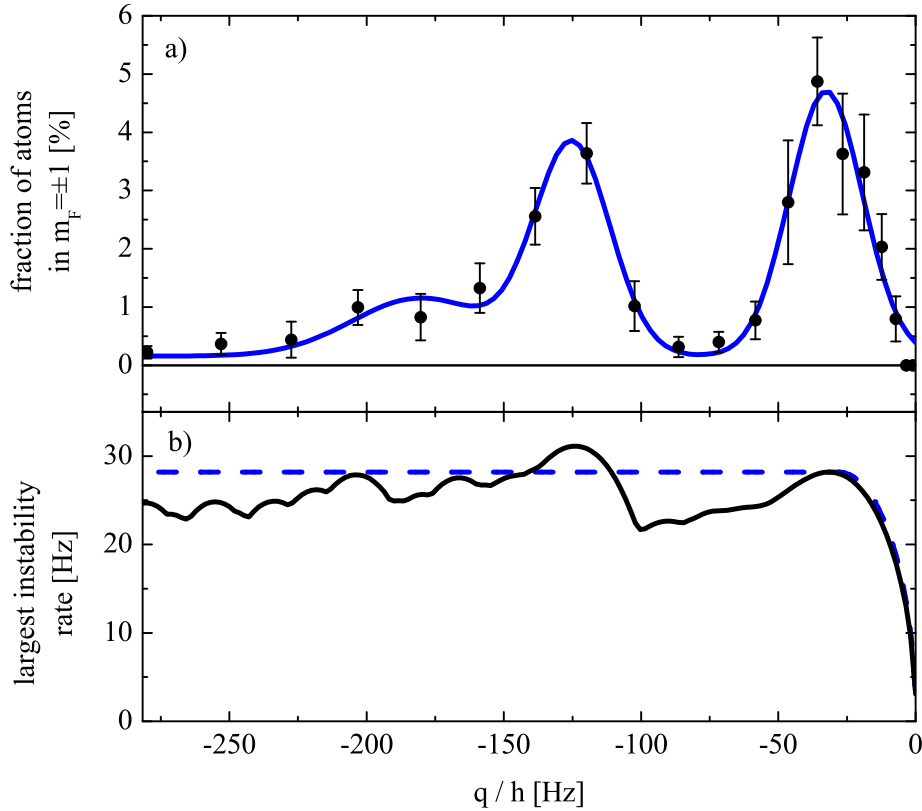
FIGURE 3.11: (a) Fraction of atoms transferred into $|\pm 1\rangle$ within 21 ms as a function of the quadratic Zeeman energy q. To obtain this fraction, the number of transferred atoms per state was divided by the sum of transferred $|\pm 1\rangle$ and condensed $|0\rangle$ atoms. Due to strong shot-to-shot fluctuations 15 independent realizations were averaged at each magnetic field. The error bars indicate statistical uncertainties. The blue line is a triple Gaussian fit to guide the eye. (b) Instability rate, given by the imaginary part of the most unstable spin Bogoliubov mode, corresponding to the pair creation efficiency into $|\pm 1\rangle$ (solid line). The maximal instability rate for an effective homogeneous case (dashed line) lacks any resonant features.

CHAPTER 4

Parametric amplification of vacuum fluctuations in a spinor condensate

Parametric amplification of vacuum fluctuations is crucial in modern quantum optics, enabling the creation of squeezing and entanglement. In this chapter, we study the parametric amplification of vacuum fluctuations for matter waves using a spinor condensate. As mentioned in previous chapters, spin-changing collisions lead to the correlated creation of pairs of atoms in $|\pm 1\rangle$ from an initially unstable $|0\rangle$ BEC, which acts as a vacuum for $|m \neq 0\rangle$ components. Although this pair creation of atoms from a $|0\rangle$ condensate is ideally triggered by vacuum fluctuations, unavoidable spurious initial atoms in $|\pm 1\rangle$ induce, as mentioned in the previous chapter, a classical seed which may become the dominant triggering mechanism.

In this chapter, we find that the classical seed plays only a relevant role at sufficiently low magnetic fields, where the amplified spin excitation mode has a large overlap with the original BEC. However, at larger magnetic fields the amplified spin excitations show pronounced spatial structures and lack a substantial overlap. As a result, our results show that the amplification is dominantly triggered by vacuum fluctuations.

The amplification of vacuum fluctuations is a key requirement for the production of non-classical matter waves with squeezed quadratures and strong quantum correlations. Our results hence open fascinating perspectives for spinor condensates, which may be employed in the next future as a source of two-mode squeezed matter waves [94] and entangled Einstein-Podolski-Rosen pairs [39, 101], and may possibly allow for Bell-type measurements [102, 103] with neutral atoms.

In this chapter, we first briefly discuss the analogy between spinor BEC and optical parametric amplifiers. We then comment on the experimental preparation of the system, and in particular on the unavoidable spurious classical seed atoms and on the quantum vacuum fluctuations. In the second part of the chapter, we study the magnetic-field dependence of the triggering mechanism and compare with experimental results obtained at the Leibniz University of Hannover.

4.1 Spinor condensates as parametric amplifiers

Parametric amplifiers have enabled the observation of non classical phenomena, by bringing the realm of quantum effects into the macroscopic world. In solid state systems, for example, low-noise Josephson-parametric amplifiers are used to investigate nonclassical electromagnetic fields [104]. In quantum optics, optical parametric amplifiers play a crucial role in the investigation and application of nonclassical states of light [105]

Nonclassical states of light have revolutionized the field of quantum optics in the past decades. Since the first observation of squeezed light [106], these non-classical states of light have become a valuable tool in modern optics, e.g. for the enhancement of modern interferometers [107]. Similarly, the production of entangled photon pairs [108] has triggered a still on-going series of fundamental tests of modern quantum mechanics [103, 109] and has many possible applications for quantum computing [110]. The tools developed for the production and manipulation of ultra-cold neutral atoms now bring many of these seminal investigations within the scope of experiments with matter waves. In this sense, the production of number-squeezed Bose-Einstein condensates [111, 112] and spin squeezed thermal clouds [113] has been demonstrated using the inherent Kerr nonlinearity in atomic condensates.

Spinor condensates initially prepared in the $|0\rangle$ Zeeman sublevel provide a promising method to generate non-classical matter waves. As mentioned in previous chapters, a collision of two $|0\rangle$ atoms can form a pair of correlated atoms in $|\pm 1\rangle$. Interestingly, this process is equivalent to photon pair creation in a non-degenerate optical parametric amplifier [90, 94]. In this analogy, the large condensate in $|0\rangle$ resembles a coherent pump, the nonlinear interactions in the condensate serve as an equivalent of the nonlinear crystal, and the produced atoms in $|\pm 1\rangle$ play the role of the signal and the idler. Pair production leads to an exponential amplification of the population in $|\pm 1\rangle$, which resembles the gain of an optical parametric amplifier. As it was mentioned in Chapter 3, the corresponding pair creation rate is governed by three competing energy scales: the quadratic Zeeman energy, the inter-atomic interactions and the external trap. In particular, the external confinement can lead to strong, magnetic field dependent spin resonances.

Similar to its optical counterpart, the output of the matter-wave amplifier depends crucially on the input state. This input state could be an ideal input that would be provided by the vacuum state $|vac\rangle$, which is characterized by the absence of atoms in $|\pm 1\rangle$ or a coherent classical input, which is characterized by the initial presence of spurious atoms in $|\pm 1\rangle$. The preparation of the initial input is hence crucial, and will be discussed next.

4.2 Experimental Preparation of the initial state

In the following we describe the experimental preparation of the initial BEC as performed at the group of J. Arlt and W. Ertmer at the Leibniz University of Hannover. In the experiment, a polarized BEC is created in $|2\rangle$, being subsequently coherently transferred into $|0\rangle$ by means of a radio frequency (rf) sweep (for more details see Ref. [100]). Afterwards, a strong magnetic-field gradient is applied in order to expel residual atoms in $|m \neq 0\rangle$ from the trap. However, this purification cannot be completely perfect, and some imperfections due to radio-frequency noise and/or magnetic field jitter result into a small amount of spuriously produced atoms, $N_s \ll N$, in the $|\pm 1\rangle$ components. These spurious atoms, the classical seed introduced in the previous chapter, are produced by single-particle processes, and thus share the spatial wave-function of the $|0\rangle$ condensate.

In the case of an ideal purification, whereby there is no any spurious atoms in $|\pm 1\rangle$, the state may be considered (in what concerns $|m \neq 0\rangle$) a *vacuum state*. This may be visualized as an ideally fixed spin orientation of the condensate. In this case, *vacuum fluctuations* result from the quantum uncertainty of the spin orientation. Note that there could also be a tiny spurious thermal seed atoms in the $|\pm 1\rangle$ component. However these thermal seed atoms are in average far away from the condensate and lack significant spatial overlap with the most unstable excitation mode (see discussion below), and as a result they do not contribute to the spin dynamics.

4.3 Triggering Mechanism

In this section we study the classical and quantum triggering mechanisms, discussing their relative importance as a function of the applied quadratic Zeeman energy q. As we discussed in previous chapters, the amplification dynamics is dominated by the most unstable spin Bogoliubov mode ν_0 with the largest imaginary part $\mathrm{Im}(\lambda_{\nu_0}) = h\Lambda(q)$. As already shown, this instability rate $\Lambda(q)$ shows a non-monotonous multi-resonant magnetic-field dependence due to the interplay between quadratic Zeeman energy, interactions and external confinement.

In the previous chapter we have shown as well how to calculate the relevant quantum evolution of the operators $\hat{a}_{n,\pm 1}(t)$ and $\hat{a}_{n,\pm 1}^{\dagger}(t)$. The total population in the $|\pm 1\rangle$ components is then given by $P_{\pm 1}(t) = \sum_n \langle \hat{a}_{n,\pm 1}^{\dagger}(t)\hat{a}_{n,\pm 1}(t)\rangle$, where the average is performed over the initial state $|\Psi_{\pm 1}(0)\rangle = |\Psi\rangle$. In the presence of the unstable spin excitation modes, the initial state $|\Psi\rangle$ triggers the subsequent amplification. Using the notation of the previous chapter, this initial state $|\Psi\rangle$ may include a classical seed, and can be represented as

$|\Psi\rangle = \frac{1}{N_s!} \left(\hat{a}_{\chi \pm 1}^{\dagger} \right)^{N_s} |\text{vac}\rangle$, where $\hat{a}_{\chi \pm 1}$ ($\hat{a}_{\chi \pm 1}^{\dagger}$), defined in subsection 3.2, creats (annihilates) a $m = \pm 1$ particle in the mode of the initial BEC. Note that if there are no spurious classical seed atoms, $N_s = 0$, in the $|\pm 1\rangle$ components, then pair-creation in $|\pm 1\rangle$ is ideally triggered by vacuum fluctuations. Otherwise, the classical seed in $|\pm 1\rangle$ components may become the dominant triggering mechanism.

One may re-write the population $P_{\pm 1}(t)$ from Eq. (3.18) as $P_{\pm 1} = P_C(t) + P_Q$, where

$$P_C(t) = N_s \vec{\chi} \cdot \left(\mathbf{O}^{\dagger} \mathbf{O} + \widetilde{\mathbf{O}}^{\dagger} \widetilde{\mathbf{O}} \right) \cdot \vec{\chi}, \qquad (4.1)$$

$$P_Q(t) = \text{Trace} \left(\widetilde{\mathbf{O}}^{\dagger} \widetilde{\mathbf{O}} \right), \qquad (4.2)$$

denote, respectively, the classically and the quantum-triggered contributions. In the previous expressions, $\vec{\chi}$ characterizes the overlap between the unstable mode and the condensate, and the matrices $\mathbf{O}$ and $\widetilde{\mathbf{O}}$ are the upper left and upper right part of the time evolution matrix $\mathbf{U(t)}$ defined in Sec. 3.2.

We have employed Eqs. (4.1) and (4.2) to determine the population in the $|\pm 1\rangle$ components at any time t. As we have discussed in subsection 3.3, although the inherent hyperfine-changing losses are small ($< 20\%$ of the total number) during the typical evolution time of 22.5 ms, they significantly alter the spin dynamics, and have been incorparated in our numerical analysis as discussed in the previous chapter, with an experimentally determined loss rate of $\Gamma \simeq 10^{-2}$ ms^{-1}.

We have performed numerical simulations for the time evolution of the population in $|\pm 1\rangle$ using the parameters of the experiments performed at the Leibniz University of Hannover. We have considered a spin-2 ^{87}Rb BEC initially containing $N = 5 \times 10^4$ atoms in an optical dipole trap with frequencies $(\omega_x, \omega_y, \omega_z) = 2\pi \times (176, 132, 46)$ Hz. We have assumed scattering lengths $a_0 = 87.685 a_B$, $a_2 = 91.049 a_B$, and $a_4 = 99.197 a_B$. Figures (4.1) show the numerical results for the population in $|\pm 1\rangle$.

Figure (4.1a) shows the magnetic-field dependence of the classically ($P_C(t)$) and quantum ($P_Q(t)$) triggered fraction of transferred atoms into $|\pm 1\rangle$ after an evolution time of 22.5 ms. The fraction of the transferred atoms due to the quantum triggered part is larger than the classically triggered part (with $N_s = 1$). Moreover, the second pronounced peak is absent in the classically triggered part. Hence the classical seed N_s only influences the spin dynamics significantly at the low magnetic-fields. We shall clarify in further subsections the reasons of this behavior.
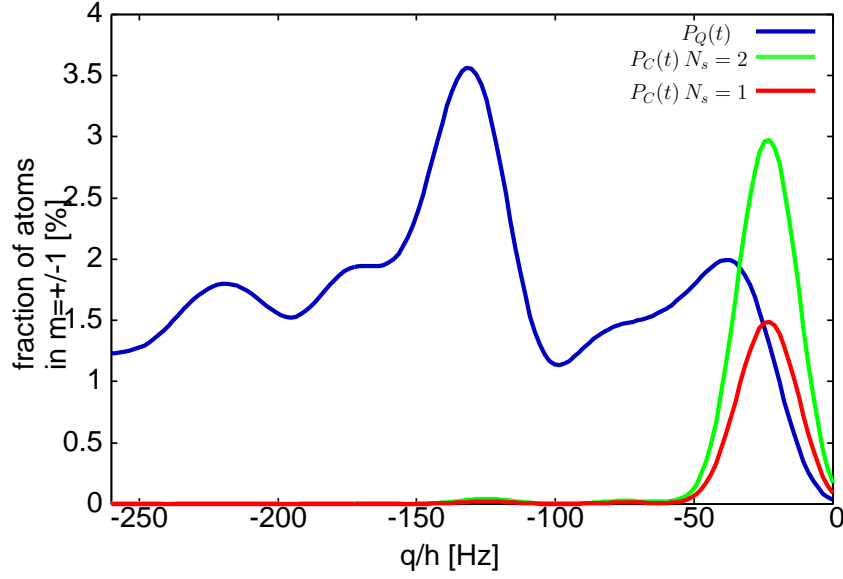
(A)
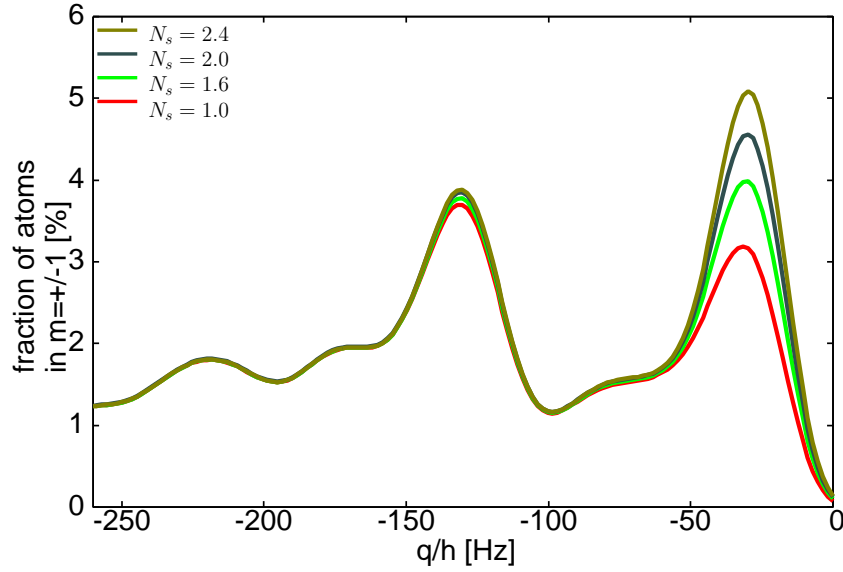
(B)

FIGURE 4.1: Fraction of atoms in the $|\pm 1\rangle$ components as a function of the quadratic Zeeman energy q for different experimental parameters: $N = 5 \times 10^4$ initial number of particles, trap frequencies $2\pi \times (176, 132, 46)$ Hz and scattering lengths $a_0 = 87.685 a_B$, $a_2 = 91.049 a_B$, and $a_4 = 99.197 a_B$. In Fig. (4.1a) the blue color corresponds to the quantum triggering part only, and the green and red colors correspond to the classically triggered part with classical seed atoms of $N_s = 2$ and $N_s = 1$ respectively. Fig. (4.1b) shows the total fraction of atoms as a function of the quadratic Zeeman energy q for different classical seed atoms. The classical seed atoms strongly influence the dynamics at the low magnetic-fields.

Figure (4.1b) shows the total fraction of transferred atoms, $P_C(t) + P_Q(t)$, in $|\pm 1\rangle$ after the same evolution time of 22.5 ms, which as mentioned in previous chapters shows a striking multi-resonant magnetic-field dependence, which maps the instability rate $\Lambda(q)$. The most pronounced resonances are at $q = -29.92$ Hz and $q = -130.24$ Hz, which we refer to as the low magnetic-field and high magnetic-field resonances respectively. The absolute value of the fraction of transferred atoms strongly depends on the initial condition. When we change N_s, the absolute value of the fraction of transferred atoms changes significantly at the low magnetic-field resonance. As an example, for $N_s = 1$, (red curve in Fig. 4.1b), the population at the higher magnetic-field resonance is larger than the lower magnetic-field one. However, for $N_s = 2$ (dark-grey curve in Fig. 4.1b), the low magnetic-field resonance is larger than the high magnetic-field one. Hence, the relative importance of both resonances strongly depends on the classical seed.

4.3.1 Relative importance of both triggering mechanisms

The relative importance of both triggering mechanisms is obtained from the ratio of the classical and quantum triggered parts. To gain a qualitative understanding of this, we consider the case of a box model. Thus, from subsection 3.2, the classical and quantum triggered parts in a box potential trap are given by

$$P_C(t) = 2N_s \sum_n \chi_n^2 \left[\frac{U_{1-1}n_0}{2|\lambda_n^+|} \right]^2 e^{\,2\mathrm{Im}(\lambda_n^+)\,t/\hbar} \quad \text{and}$$

$$P_Q(t) = \sum_n \left[\frac{U_{1-1}n_0}{2|\lambda_n^+|} \right]^2 e^{\,2\mathrm{Im}(\lambda_n^+)\,t/\hbar},$$

(4.3)

It is particularly useful to introduce the ratio $\eta = P_C/P_Q$ between both triggering mechanisms for $N_s = 1$:

$$\eta(t) = \frac{2 \sum_n \chi_n^2 \left[\frac{U_{1-1}n_0}{2|\lambda_n^+|} \right]^2 e^{\,2\mathrm{Im}(\lambda_n^+)\,t/\hbar}}{\sum_n \left[\frac{U_{1-1}n_0}{2|\lambda_n^+|} \right]^2 e^{\,2\mathrm{Im}(\lambda_n^+)\,t/\hbar}}.$$

(4.4)

When $\eta(t) \geq 1$ the classically triggered part dominates. On the contrary, if $\eta(t) < 1$ then the quantum triggered part is dominant, and one expects that as a result the classical seed does not significantly influence the amplification process.

For large evolution times, only the most unstable mode with the largest imaginary part $\mathrm{Im}(\lambda_{n_{max}}) = h\Lambda(q)$ contributes to the spin dynamics. Hence

we may characterize the growth by making a single-mode approximation, just paying attention to the contribution of this most unstable mode. Accordingly, the expressions for the classically and quantum-triggered parts take the form

$$P_C(t) = 2\chi_{n_{max}}^2 e^{2\Lambda(q)t},$$
$$P_Q(t) = e^{2\Lambda(q)t}, \tag{4.5}$$

and hence $\eta = 2\chi_{n_{max}}^2$, where $\chi_{n_{max}}$ characterizes the overlap between the most unstable mode and the condensate. To study the magnetic-field dependence of the ratio η, we have hence to study the magnetic-field dependence of $\chi_{n_{max}}$.

The magnetic-field dependence of the overlapping can be understood from our discussion of the preceeding chapters. We recall that two different unstable regimes occur:

- $q_{cr} < q < q_{cr} + |q_{cr}|$, in this regime the most unstable mode, which is the ground state of the box trap, has the same symmetry as the condensate, and as a result the overlapping of this most unstable mode with the condensate $\chi_{n_{max}}$ is maximum. This leads to $\eta \geq 1$, and hence the classically triggered part dominates.

- $q < q_{cr}$, in this regime the most unstable mode has a momentum $\sqrt{2(q_{cr} - q)}$, which leads to a smaller overlapping $\chi_{n_{max}}$ with the original BEC and hence eventually $\eta < 1$. In this case the quantum triggered part is dominant and as a result the classical seed does not significantly influence the amplification process.

Therefore, as we quench q towards higher values, i.e. as we excite progressively higher modes of the effective box-trap, the overlapping of the most unstable mode $\chi_{n_{max}}$ with the original condensate becomes smaller, and consequently the influence of the classical seed becommes negligible in the higher magnetic fields.

We have analyzed numerically the relative importance of both triggering mechanisms for realistic experimental situations. In our numerical calculations we have considered a spin-2 ^{87}Rb BEC containing $N = 5 \times 10^4$ initial number of particles in an optical dipole trap with frequencies $(\omega_x, \omega_y, \omega_z) = 2\pi \times (176, 132, 46)$ Hz and considered scattering lengths $a_0 = 87.685a_B$, $a_2 = 91.049a_B$, and $a_4 = 99.197a_B$. Fig. (4.2) shows η for an evolution time of 15 ms and for the limit of large evolution times. For large evolution times, as in the case of the box-trap model, we may approximate the evolution of $P_{C,Q}(t) \simeq \bar{P}_{C,Q} \exp(2\Lambda(q)t)$ and evaluate the time-independent ratio $\eta = \bar{P}_C/\bar{P}_Q$ between the classical and quantum triggering mechanisms. For sufficiently small quadratic Zeeman $|q|$, including the low magnetic-field resonance shown in Fig. (4.4), any classical seed is highly relevant ($\eta \sim 1$) due to the large overlap between the wave function of the most unstable mode and

the original BEC. However, for larger quadratic Zeeman $|q|$, including the high magnetic-field resonance, the overlap is negligible and the population is dominantly triggered by quantum vacuum fluctuations.

This general analysis may also be applied to other experiments on spinor BEC. In particular, Fig. (4.3) shows the relative importance of both triggering mechanisms for recent amplification experiments with spin-1 ^{87}Rb at Berkeley [93].
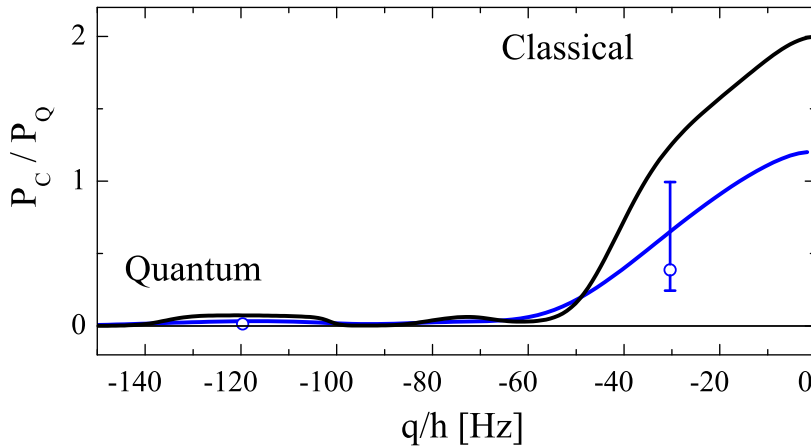
FIGURE 4.2: Ratio P_C/P_Q (see text) for the given parameters at an evolution time of 15 ms (blue) and for the limit of large evolution times (black). The quantum triggered dynamics is characterized by $P_C/P_Q \ll 1$. The hollow circles represent the experimental results (see Sec. 4.4.2).
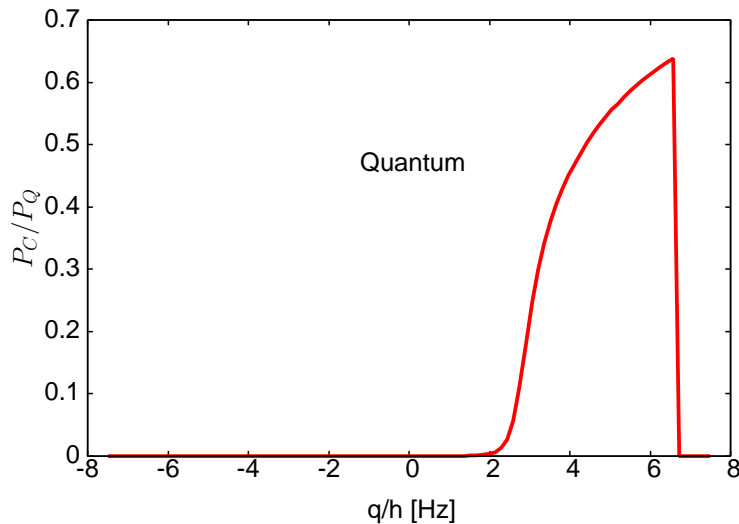
FIGURE 4.3: Ratio P_C/P_Q for the experimental parameters of Ref. [93], $(\omega_x, \omega_y, \omega_z) = 2\pi \times (440, 39, 4.2)$ Hz and $N = 2 \times 10^6$ atoms, for the limit of large evolution times. The quantum triggered dynamics is characterized by $P_C/P_Q \ll 1$.

4.4 Comparison with Experiments

To compare the theoretical results with the experimental data for $F = 2$ ^{87}Rb, as mentioned in Sec. 3.3, it is crucial to take into account the loss of atoms due to hyperfine changing collisions. Otherwise, the fraction of transferred atoms is far too large for the given experimental data as shown in Fig. (3.8). Other crucial experimental parameters that must be carefully considered concern the classical seed atoms and the exact values of the scattering lengths. In the following, we consider a $F = 2$ ^{87}Rb BEC contaning of $N = 5 \times 10^4$ atoms in an optical dipole trap with trapping frequencies of $2\pi \times (176, 132, 46)$ Hz.

4.4.1 Multi-peaked pair creation efficiency

We have calculated the magnetic-field dependence of the multi-peaked pair creation efficiency for the given experimental parameters. In this calculation, we considered the inherent hyperfine-changing losses with an experimentally determined loss rate of $\Gamma \simeq 10^{-2}$ ms^{-1}.

Figure 4.4 (a) shows the numerical results for the population tranferred into $|\pm 1\rangle$. As already shown in the preceeding chapter, the multi-resonant dependence of the instability rate $\Lambda(q)$ discussed in Chapter 3 directly maps into a multi-peaked pair creation efficiency, which is in a very good agreement with the experimental results.

As discussed in the above subsection 4.3, the classical seed atoms only influence the spin dynamics significantly at the low magnetic-field resonance, and hence the relative transferred fraction of atoms in the two resonances crucially depends on the number of classical seed atoms N_s.

Accordingly, the relative transferred fraction of atoms from the experimental result is obtained from a fit to the relative fraction of atoms on the two theoretical resonances, which corresponds to an estimated average number of classical seed atoms of $N_s = 1.6$ and $N_s = 2.4$, respectively. Furthermore, as it was mentioned in Sec. 3.2, the amplification dynamics depends on the total number of atoms and especially on the precise values of the scattering lengths a_F. We have employed $a_0 = 87.685 a_B$, $a_2 = 91.049 a_B$, and $a_4 = 99.197 a_B$, which are within their rather strict uncertainities [1], and lead to an excellent fit with the experimental results.

---

[1]Coupled channel analysis performed by Prof. E. Tiemann predict $a_0 = 87.9(2) a_B$, $a_2 = 91.2(2) a_B$, $a_4 = 99.0(2) a_B$
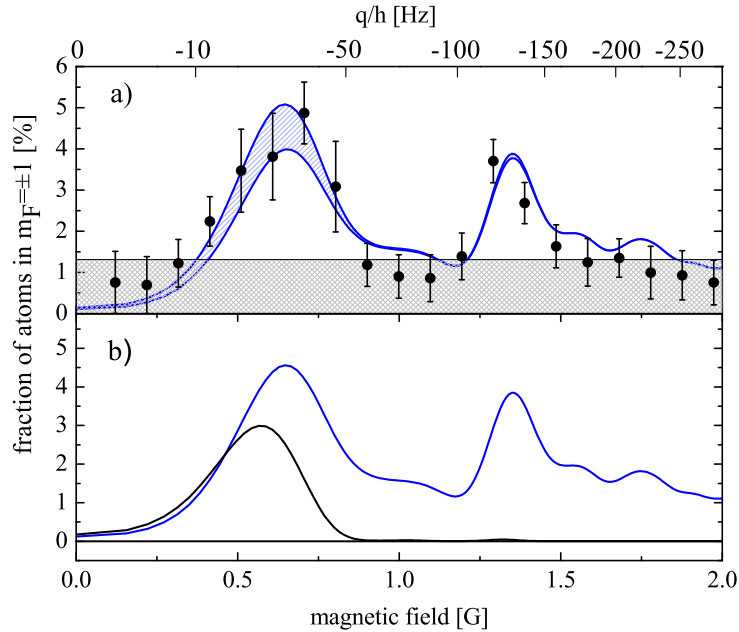
FIGURE 4.4: (a) Fraction of atoms transferred into $|\pm 1\rangle$ within 21 ms as a function of the applied magnetic field [100]. The error bars indicate statistical uncertainties and the detection uncertainty. The shaded blue area indicates the result of our theoretical prediction for a seed atom number of $N_s = 2 \pm 0.4$, assuming an initial BEC in $|0\rangle$ with $N = 50000$ (see text). The grey area indicates the detection limit for a single atom number measurement. (b) Comparison of the calculation, including both the classical seed $N_s = 2$ and vacuum spin fluctuations (blue line) with the GP result (black line).

Figure 4.4 (b) shows the numerical results for the given experimental parameters for both the exact calculation and the GPE calculation. These results show that the spin dynamics differs significantly from the result of the simple mean-field GPE approach introduce in Sec. 3.4. The striking difference between GP and exact results are a further indication of the fact that the two resonances display a very different sensitivity to a classical seed and quantum vacuum fluctuations.

4.4.2   Classical seed N_s sensitivity of the pair-creation efficiency

Experiments at the Leibniz University of Hannover have investigated the sensitivity of the spin dynamics to classical seed atoms at the available unstable spin excitation resonances. The sensitivity of the system to a classical seed is investigated by deliberately producing a very small symetric seed population in $|\pm 1\rangle$ prior to the spin evolution. This is accomplished by using a radio frequency pulse, which transfers a variable number of atoms from the $|0\rangle$

BEC into $|\pm 1\rangle$. By ramping down the intensity of the radio-frequency pulse it was possible to general controllably extremelly small number of atoms in $|\pm 1\rangle$. Note that there are also some spurious seed atoms in the experiment. Since both the spuriously and deliberately produced seeds result from similar single-atom processes, they have exactly the same spatial dependence as the original BEC. Therefore, the sensitivity to the deliberately produced seed is representative of the sensitivity to any classical seed in the experiment.
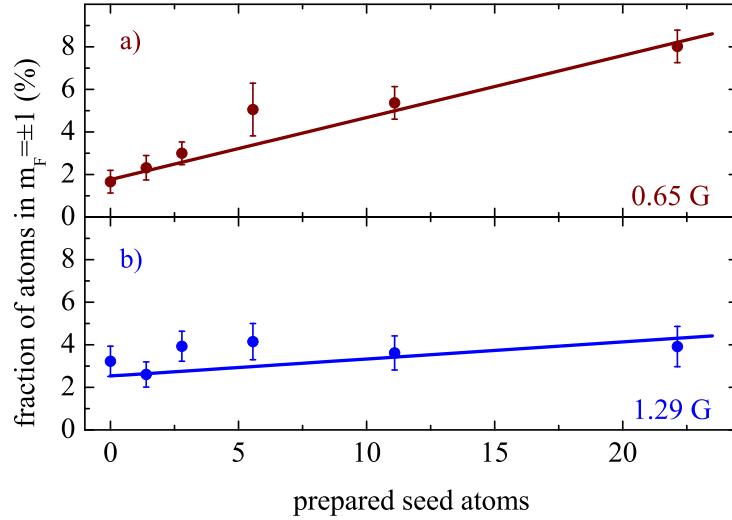
FIGURE 4.5: Fraction of atoms transferred into $|\pm 1\rangle$ as a function of the number of deliberately prepared seed atoms (in the BEC mode). (a) The fraction recorded at 0.65 G, corresponding to the low field resonance, shows a strong dependence on the classical seed after an evolution time of 15 ms. (b) The fraction recorded after $t = 23$ ms on the high field resonance at 1.29 G is basically independent of the number of seed atoms and we conclude that it is triggered by vacuum spin fluctuations. The error bars indicate statistical uncertainties. The solid lines represent the result of the theoretical model with a seed atom number $N_s = 4.5$.

Figure 4.5 (a) shows for the low magnetic-field resonance (Fig. 4.4) the transferred fraction of atoms in $|\pm 1\rangle$ after the spin dynamics, as a function of the number of deliberately created seed atoms. Starting at a small offset value, this transferred fraction of atoms grows linearly with increasing number of seed atoms (an amplification of 23 dB). Hence the low field resonance is strikingly sensitive to a classical seed, down to an extremely small number of seed atoms. The offset is both due to the amplification of vacuum fluctuations and a small number of accidentally produced seed atoms. A comparison of our theoretical model yields a seed atom number of $N_s = 4.5 \pm 0.3$, which is slightly higher than the value presented in Fig. 4.4 due to the additional preparation time after purification. An independent linear fit to the data yields the slope and the offset at zero seed atoms (at position $-N_s$ in the graph). The ratio of slope to offset yields the ratio of classical to quantum

triggering. The resulting data points are shown in Fig. 4.5 and confirm our theoretical model.

However this sensitivity to a classical seed is not general. Figure 4.5 (b) shows the fraction of transferred atoms for the high-field resonance. For this resonance the fraction of $|\pm 1\rangle$ atoms is largely independent of the number of deliberately produced seed atoms, which indicates that a spurious classical seed is irrelevant for sufficiently large $|q|$. Note in particular the remarkable difference between the results for P_C/P_Q at both resonances in Fig. 4.2. This experimentally confirms that quantum triggering dominates the amplification dynamics at the high field resonance and pair creation conclusively acts as a parametric amplification of vacuum fluctuations.

Parametric amplification of matter waves in dipolar spinor BECs

Interestingly, spin-changing collisions are typically characterized by a very low energy scale much lower than the chemical potential in the condensate. As a result of that, the spinor dynamics in alkaline gases may be extraordinarily sensitive to the magnetic dipole-dipole interactions (DDI). Moreover, the DDI is expected to yield rich phenomena when combined with spin degrees of freedom, such as the Einstein-de Hass effect [88, 114] and ground-state spin textures and mass currents [115, 116].

Up to very recently, only short-range interactions have played a role in typical experiments in ultra-cold gases. Recent experiments have started to unveil the rich physics resulting from the dipole-dipole interactions [117, 118]. This is particularly the case of Chromium, which presents a relatively large magnetic dipole moment, $\mu = 6\mu_B$. Remarkable effects of the magnetic DDI have been reported in recent experiments on Chromium BEC [119–124]. Alkaline atoms, on the contrary, present a much lower magnetic dipole moment, $\mu = \mu_B/2$, and hence they are not usually expected to show any trace of the DDI unless short-range interactions are switched-off by means of Feshbach resonances [125, 126]. However, as mentioned above, the spin-changing collisions in alkaline spinor BECs (in particular spin-$f = 1$ ^{87}Rb) are remarkably low-energetic. As a result, spinor dynamics is very sensitive to magnetic DDI, in spite of the very low magnetic dipole moment. Recent experiments [127] have shown that the DDI may induce magnetization patterns in spin-$f = 1$ ^{87}Rb BECs.

In this chapter we show that the amplification dynamics discussed in previous chapters may be extremely sensitive to the magnetic DDI. As a result of that, the amplification of EPR-like pairs is largely modified by the relative orientation between the applied magnetic field and the trap axis. We analyze in detail this dependence, as well as the effects of magnetic-field gradients. We show that these gradients modify also largely the amplification process and must be carefully controlled, since uncontrolled gradients may obscure the expected DDI effects.

The structure of the chapter is as follows. In Sec 5.1 we develop the linear regime Hamiltonian of the system considered (dipolar spinor BEC). An

intuitive qualitative picture of the effects of the DDI in the instability rate is discussed in Sec. 5.2. The discussion of these effects in a trapped system will be presented in Sec. 5.3. In Sec. 5.4 we introduce the main formalism to analyze the amplification dynamics in the presence of DDI, whereas the corresponding numerical results are presented in Sec. 5.4.1. The effects of the magnetic-field gradient are analyzed in Sec. 5.5. Finally we discuss experimental requirements in Sec. 5.6.

5.1 Linear regime Hamiltonian of dipolar spinor BECs

In the following we are interested in the first stages (linear regime) of the spinor dynamics of a spin-1 BEC initially prepared in the $|m = 0\rangle$ component, after quenching the quadratic Zeeman effect q into the unstable regime. As we have seen in Chapter 3, this dynamics, induced by spin-changing collisions, is characterized by the correlated pair creation of atoms into $|m = \pm 1\rangle$ components. In this Chapter we use a similar approach as in Chapter 2 to develop the contribution of the DDI to the effective Hamiltonian that describes the linear regime of onset of dynamics. In so doing, for the sake of simplicity, we do not consider magnetic-field gradients, which will be introduced in Sec. 5.5.

As it was mentioned in chapter 2, the first stage of the spinor dynamics may be described by means of a Bogoliubov approximation:

$$[\hat{\psi}_1(\vec{r},t), \hat{\psi}_0(\vec{r},t), \hat{\psi}_{-1}(\vec{r},t)]^T = \left[\left(\boldsymbol{\psi_0}(\vec{r}) + (\delta\hat{\psi}_1(\vec{r},t), \delta\hat{\psi}_0(\vec{r},t), \delta\hat{\psi}_{-1}(\vec{r},t) \right)^T \right] e^{-i\mu t} \tag{5.1}$$

with $(\boldsymbol{\psi_0}(\vec{r}))^T = (0, \psi_0(\vec{r}), 0)^T$. Where we consider small fluctuations of the spinor field operator $\{\delta\hat{\psi}_m(\vec{r},t)\}$, such that $|\psi_0(\vec{r})|^2 \gg \sum_m \langle \delta\hat{\psi}_m^\dagger(\vec{r},t)\delta\hat{\psi}_m(\vec{r},t)\rangle$.

In the following we consider that the condensate is trapped in a harmonic potential of the form $V(\vec{r}) = \frac{M}{2}\left(\omega_\perp^2 \left(x^2 + y'^2 \right) + \omega_\parallel^2 z'^2 \right)$, where M is the atomic mass, $\omega_\parallel \ll \omega_\perp$ are the trap frequencies (cigar-shape trap), and $y' = \cos\vartheta\, y + \sin\vartheta\, z$, $z' = -\sin\vartheta\, y + \cos\vartheta\, z$, with ϑ the angle between the trap axis and the magnetic field orientation. This angle will play a crucial role in our discussion of the effects of the DDI. Note that in the Thomas-Fermi regime $\mu = V(\vec{r}) + U_{00}n_0(\vec{r})$. In that regime, the effective potential (see Chapter 2) is $V_{eff}(\vec{r}) = U_{1-1}n_0(\vec{r})$ within the BEC region, and $V_{eff} = V(\vec{r}) - \mu$ outside.

The Hamiltonian of the DDI in the linear regime is obtained by inserting Eq. (5.1) into the Hamiltonian (1.38) and keeping terms up to second order

in $\delta\hat{\psi}_m(\vec{r})$. This gives

$$
\begin{aligned}
\hat{H}_{1,dd} &= \int d^3r\, d^3r'\, \delta\hat{\psi}_1^\dagger(\vec{r},t)\delta\hat{\psi}_{-1}^\dagger(\vec{r}',t)W_{1,-1}^{0,0}(\vec{r}-\vec{r}')\psi_0(\vec{r})\psi_0(\vec{r}') \\
&+ \int d^3r\, d^3r'\, \psi_0(\vec{r})\delta\hat{\psi}_{-1}^\dagger(\vec{r},t')W_{0,-1}^{0,-1}(\vec{r}-\vec{r}')\delta\hat{\psi}_{-1}(\vec{r},t)\psi_0(\vec{r}') \\
&+ \int d^3r\, d^3r'\, \psi_0(\vec{r})\delta\hat{\psi}_1^\dagger(\vec{r}',t)W_{0,1}^{0,1}(\vec{r}-\vec{r}')\delta\hat{\psi}_1(\vec{r},t)\psi_0(\vec{r}') \\
&+ \int d^3r\, d^3r'\, \Big\{\left(\psi_0(\vec{r})+\delta\hat{\psi}_0^\dagger(\vec{r}',t)\right)\left(\psi_0(\vec{r})+\delta\hat{\psi}_0^\dagger(\vec{r}',t)\right) \\
&\qquad W_{0,0}^{0,0}(\vec{r}-\vec{r}')\left(\psi_0(\vec{r})+\delta\hat{\psi}_0(\vec{r},t)\right)\left(\psi_0(\vec{r}')+\delta\hat{\psi}_0(\vec{r}',t)\right)\Big\} \quad (5.2)
\end{aligned}
$$

with

$$
W_{1,-1}^{0,0}(\vec{r}-\vec{r}') \equiv \frac{c_{dd}}{|\vec{r}-\vec{r}'|^3}\left[\vec{f}_{01}\cdot\vec{f}_{0-1}-3\left(\vec{f}_{01}\cdot\vec{u}_r\right)\left(\vec{f}_{0-1}\cdot\vec{u}_r\right)\right], \quad (5.3)
$$

and

$$
W_{m,0}^{0,m}(\vec{r}-\vec{r}') \equiv \frac{c_{dd}}{|\vec{r}-\vec{r}'|^3}\left[\vec{f}_{m0}\cdot\vec{f}_{0m}-3\left(\vec{f}_{m0}\cdot\vec{u}_r\right)\left(\vec{f}_{0m}\cdot\vec{u}_r\right)\right]. \quad (5.4)
$$

Inserting the values of $\hat{\vec{f}}_{m_3m_2}\cdot\hat{\vec{f}}_{m_4m_1}$ and $\hat{\vec{f}}_{m_3m_2}\cdot\vec{u}_r$ (detail calculations are included in Appendix B) into Eqs. (5.3) and (5.4), we obtain

$$
W_{m,0}^{0,m}(\vec{r}-\vec{r}') \equiv W_{1,-1}^{0,0}(\vec{r}-\vec{r}') \equiv \frac{c_{dd}}{|\vec{r}-\vec{r}'|^3}\left[\frac{3(z-z')^2}{|\vec{r}-\vec{r}'|^2}-1\right], \quad (5.5)
$$

with $m=\pm1$ and $W_{0,0}^{0,0}(\vec{r}-\vec{r}')=0$.

Therefore, there is no DDI contribution in the GP Eq. (2.1), since $\vec{f}_{00}=0$. There is however an important contribution to the effective Hamiltonian that describes the pair creation of atoms into $|\pm1\rangle$ components. This contribution is then obtained by employing Eq. (5.5) into Eq. (5.2), and after some calculations, the contribution to the effective Hamiltonian from the DDI $\hat{H}_{1,dd}$ has the form

$$
\begin{aligned}
\hat{H}_{1,dd} &= \int d^3r\, d^3r'\, \psi_0(\vec{r})\psi_0(\vec{r}')V_{\mathrm{dd}}(\vec{r}-\vec{r}') \\
&\times\Big[\delta\hat{\psi}_1^\dagger(\vec{r},t)\delta\hat{\psi}_1(\vec{r}',t)+\delta\hat{\psi}_{-1}^\dagger(\vec{r},t)\delta\hat{\psi}_{-1}(\vec{r}',t) \\
&\quad +\delta\hat{\psi}_1^\dagger(\vec{r},t)\delta\hat{\psi}_{-1}^\dagger(\vec{r}',t)+\delta\hat{\psi}_1(\vec{r},t)\delta\hat{\psi}_{-1}(\vec{r}',t)\Big] \quad (5.6)
\end{aligned}
$$

with $V_{\mathrm{dd}}(\vec{r}-\vec{r}')=\frac{c_{dd}}{2|\vec{r}-\vec{r}'|^5}\left(3(z-z')^2-|\vec{r}-\vec{r}'|^2\right)$.

In deriving the above effective Hamiltonian of Eq. (5.6), we have neglected terms related to scattering processes which do not preserve the total spin projection since, as mentioned in Sec. 1.2.3, the associated change in linear Zeeman energy (LZE) suppresses spin-violating processes even for very low magnetic fields. Note that the third line of $\hat{H}_{1,dd}$ originates from the spin-changing collisions, which converts atoms in the $|m = 0\rangle$ component into pair of atoms in the $|\pm 1\rangle$ components and vice-versa. This term is similar to the parametric amplification term discussed in Chapter 2. Thus, the DDI regularises the amplification process, i.e. depending on its sign either it will enhance or reduce the amplification process. To gain qualitative understanding of this effect, we will discuss the homogenous system in the following section.

5.2 Qualitative picture of the effect of the dipole-dipole interactions on the instability rate

The effects of the DDI on the amplification dynamics may be qualitatively understood from a simplified homogeneous model. We will first briefly recall the discussion of the homogenous case without DDI and then extend the discussion to the case when there is DDI. We introduce the Fourier Transform $\delta\hat{\psi}_m(\vec{r}) = \int d^3k/(2\pi)^3 e^{i\vec{k}\cdot\vec{r}}\hat{\eta}_m(\vec{k})$, which allows to write the non-dipolar Hamiltonian of Chapter 2 (Eq. (2.6)) in the simplified form: $H_1^{hom} = \int \hat{h}_k d^3k/(2\pi)^3$, where

$$
\begin{aligned}
\hat{h}_k &= \sum_{m_F}(E_k + q - q_{cr})\,\eta_{m_F}^\dagger(\vec{k})\eta_{m_F}(\vec{k}) \\
&- q_{cr}\left(\hat{\eta}_1^\dagger(\vec{k})\hat{\eta}_{-1}^\dagger(-\vec{k}) + \hat{\eta}_1(\vec{k})\hat{\eta}_{-1}(-\vec{k})\right),
\end{aligned}
\tag{5.7}
$$

with $E_k = \hbar^2 k^2/2M$ and $q_{cr} = -U_{1-1}n_0$. Note that for spin-$F = 1$ ^{87}Rb $U_1 < 0$, and hence $q_{cr} > 0$ (we consider in the following this case, although for the spin-$F = 2$ case the sign is the opposite as disccued in previous chapters). This Hamiltonian possesses eigen-energies

$$
\lambda_{\vec{k}}^\pm(q) = \sqrt{(E_k + q - q_{cr})^2 - q_{cr}^2}.
\tag{5.8}
$$

In the following we apply a similar formalism to the DDI term $\hat{H}_{1,dd}$. We introduce the Fourier transformation of $V_{dd}(\vec{r})$ to obtain $\tilde{V}_{dd}(\vec{k}) = U_{dd}(1 - 3\cos^2\theta)$, where $U_{dd} = 2\pi c_{dd}/3$ and θ is the angle between $\vec{k}$ and the dipole orientation (z axis). Using convolution theorem, and since we assume the density of the $|0\rangle$ BEC, n_0, as constant, we may then re-write $\hat{H}_{1,dd}$ in the

form:

$$
\hat{H}_{1,dd}^{hom} = \int \frac{d^3k}{(2\pi)^3} n_0 \tilde{V}_{dd}(\theta) \left\{ \sum_{m_F=\pm 1} \hat{\eta}_m(\vec{k})^\dagger \hat{\eta}_m(\vec{k}) \right.
$$
$$
\left. + \hat{\eta}_1(\vec{k})^\dagger \hat{\eta}_{-1}(-\vec{k})^\dagger + \hat{\eta}_1(\vec{k}) \hat{\eta}_{-1}(-\vec{k}) \right\}. \tag{5.9}
$$

Hence, the total effective Hamiltonian that describes the pair creation of atoms into $|m = \pm 1\rangle$ components becomes $\hat{H}_{1,Tot}^{hom} = \int \hat{h}_k^{Tot} d^3k/(2\pi)^3$, where

$$
\hat{h}_k^{Tot} = \sum_{m_F} \left(E_k + q - q_{cr} + n_0 \tilde{V}_{dd}(\theta) \right) \eta_{m_F}^\dagger(\vec{k}) \eta_{m_F}(\vec{k})
$$
$$
- (q_{cr} - n_0 \tilde{V}_{dd}(\theta)) \left(\hat{\eta}_1^\dagger(\vec{k}) \hat{\eta}_{-1}^\dagger(-\vec{k}) + \hat{\eta}_1(\vec{k}) \hat{\eta}_{-1}(-\vec{k}) \right). \tag{5.10}
$$

This total effective Hamiltonian, may be easily diagonalized for each momentum $\vec{k}$, having eigen-energies of the form

$$
\lambda_{\vec{k}}^{\pm}(q) = \sqrt{(E_k + q - q_{cr}^{eff}(\theta))^2 - q_{cr}^{eff}(\theta)^2}, \tag{5.11}
$$

with an effective $q_{cr}^{eff}(\theta) = q_{cr} - n_0 \tilde{V}_{dd}(\theta)$.

Note that, due to the anisotropy of the DDI, q_{cr}^{eff} depends on the angle θ. The effects of the trap geometry may be qualitative understood from this θ dependence. For axisymmetric trap the dominant momenta are those along the tightest direction. Therefore, when the axisymmetric trap is along the dipole orientation, then the dominant momenta in the instability (those with the lowest $\vec{k}$) are those with $\theta = \pi/2$, and hence $q_{cr}^{eff} \simeq q_{cr} - n_0 U_{dd}$. On the contrary, if the axisymmetric trap is perpendicular to the dipole orientation, then the dominant momenta are those with $\theta = 0$. Thus, $q_{cr}^{eff} \simeq q_{cr} + 2n_0 U_{dd}$.

Recall from Ch. 2 that the instability rate rises between $q_{cr}^{eff} < q < 2q_{cr}^{eff}$ acquiring its maximal value $\Lambda \simeq q_{cr}^{eff}$ at $q = q_{cr}^{eff}$, remaining constant for the homogeneous case for $q < q_{cr}^{eff}$. We, hence expect an enhancement of the instability for a magnetic field orientation perpendicular to the trap axis, and a reduced instability for a parallel orientation. Moreover, the position of the maxima shifts to the right, when the magnetic-field is perpendicular to the axisymetric of the trap, and to the left, when they are parallel, compared to the situation when there is no DDI.

Although the DDI in alkaline atoms is typically very weak, the spin-changing collisions are very weak as well. In particular, in spin-$f = 1$ [87]Rb the strength of the DDI is quite significant compared to the strength of the spin-changing collisions, $|U_{dd}/U_{1-1}| \approx 0.2$ [1]. As a result, the DDI modification

---

[1]On the contrary, in spin-$f = 2$ [87]Rb the strength of the DDI is quite smaller compared to the strength of the spin-changing collisions, $|U_{dd}/U_{1-1}| \approx 0.076$.

of the instability rate is expected to lead to a marked orientation dependence of the amplification dynamics. In the following sections we show that this is indeed the case when considering realistic trapped cases.

.

5.3 Instability rate of a trapped dipolar spinor condensates

Although the homogeneous model discussed before allows for a simplified intuitive understanding of the major effects of the DDI in the amplification process, a quantitative analysis of realistic experimental situations may be just achieved by properly considering the inhomogeneous trapping, and the corresponding inhomogeneous density $n_0(\vec{r})$ of the BEC in the $|0\rangle$ component.

As in Ch. 3 the analysis of the dipolar spinor dynamics is significantly simplified by considering the eigenfunctions and eigenergies of $\hat{H}_{eff}$, $\hat{H}_{eff}\phi_n(\vec{r}) = \epsilon_n\phi_n(\vec{r})$, and expanding the field operators in the basis of these eigenstates $\delta\hat{\psi}_m(\vec{r},t) = \sum_n \phi_n(\vec{r})\hat{a}_{n,m}(t)$. We may then re-write:

$$
\begin{aligned}
\hat{H}_1 + \hat{H}_{1,dd} \; = \; & \\
& \sum_n ((\epsilon_n + q)\delta_{n,n'} + B_{n,n'}) \sum_{m_F = \pm 1} \hat{a}^\dagger_{nm}\hat{a}_{n'm} \\
& + \sum_{nn'} (A_{nn'} + B_{n,n'}) \left(\hat{a}^\dagger_{n1}\hat{a}^\dagger_{n'-1} + \hat{a}_{n1}\hat{a}_{n'-1} \right),
\end{aligned}
\tag{5.12}
$$

where $A_{nn'} = U_{1-1} \int d^3r \, n_0(\vec{r})\phi_n(\vec{r})\phi_{n'}(\vec{r})$ characterizes the effects of the short-range spin-changing collisions, whereas the effects of the DDI are given by

$$
B_{nn'} = \int d^3r \int d^3r' F_n(\vec{r})V_{dd}(\vec{r}-\vec{r}')F_{n'}(\vec{r}'),
\tag{5.13}
$$

where $F_n(\vec{r}) = \psi_0(\vec{r})\phi_n(\vec{r})$. The matrix elements $B_{n,n'}$ are most efficiently calculated in $\vec{k}$-space according to

$$
B_{nn'} = \int \frac{d^3k}{(2\pi)^3} \tilde{F}_n(\vec{k})\tilde{V}_{dd}(\vec{k})\tilde{F}_{n'}(\vec{k})
\tag{5.14}
$$

where $\tilde{F}(\vec{k})$ is the Fourier transform of $F(\vec{r})$.

Eq. (5.12) is solved by the multimode Bogoliubov ansatz

$$
\hat{\alpha}^\pm_\nu = \sum_n \left(u^\pm_{\nu n}\hat{a}_{n1} + v^\pm_{\nu n}\hat{a}^\dagger_{n-1} \right),
\tag{5.15}
$$

where $\hat{\alpha}^\pm_\nu$ satisfy

$$
\left[\hat{\alpha}^\pm_\nu, \hat{H}_1 + \hat{H}_{1,dd} \right] = \lambda^\pm_\nu \hat{\alpha}^\pm_\nu,
\tag{5.16}
$$

which leads to the eigenvalue equation:

$$\mathbf{C} \cdot \begin{pmatrix} \vec{u}_\nu^{\pm} \\ \vec{u}_\nu^{\pm} \end{pmatrix} = \lambda_\nu^{\pm} \begin{pmatrix} \vec{u}_\nu^{\pm} \\ \vec{u}_\nu^{\pm} \end{pmatrix}, \tag{5.17}$$

where $\vec{u}_\nu^{\pm\,T} \equiv \{u_{\nu1}^{\pm}, u_{\nu2}^{\pm}, \dots\}$ (and similarly for $\vec{v}_\nu^{\pm}$) and

$$\mathbf{C} = \begin{bmatrix} (\epsilon_n + q)\mathbf{1} + \mathbf{B} & -\mathbf{A} + \mathbf{B} \\ \mathbf{A} + \mathbf{B} & -(\epsilon_n + q)\mathbf{1} - \mathbf{B} \end{bmatrix}, \tag{5.18}$$

with $\mathbf{1}$ the identity matrix, and $\mathbf{A}$ ($\mathbf{B}$) the matrix with components $A_{n,n'}$ ($B_{n,n'}$).

After diagonalizing Eq. (5.18) numerically, we obtain the spin Bogoliubov modes $\lambda_\nu(q)$. In our numerical calculations we have considered realistic experimental conditions, with $N = 10^5$ spin-$f = 1$ ^{87}Rb atoms in a cigar-shaped harmonic potential with $\omega_\perp = 2\pi \times 200$ Hz, and $\omega_\parallel = 2\pi \times 40$ Hz.
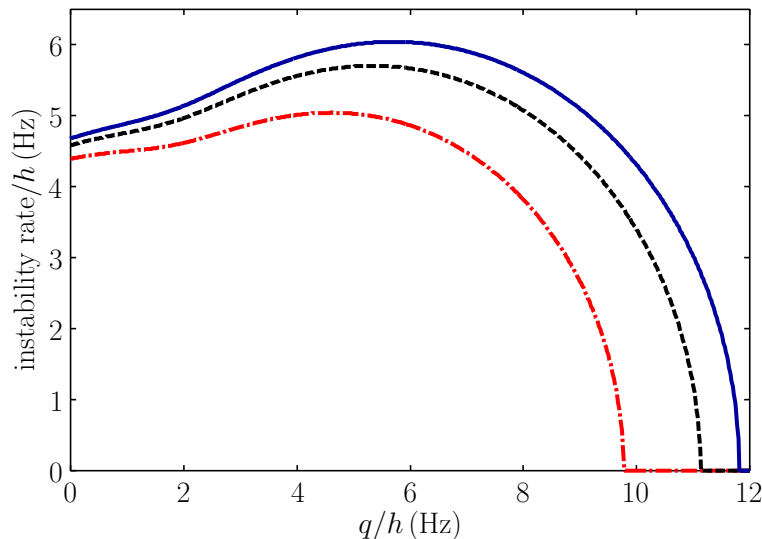
FIGURE 5.1: Instability rate $\Lambda(q)$ as a function of q for $N = 10^5$, $\omega_\perp = 2\pi \times 200$ Hz and $\omega_\parallel = 2\pi \times 40$ Hz, for the case when there is no DDI (black, dashed), when axisymmetric trap is aligned along the orientation of the magnetic field (red, dot-dashed) and when the magnetic field is oriented perpendicular to the trap axis (blue, solid).

Fig. 5.1 shows the dependence of the maximal instability rate $\Lambda(q) = \mathrm{Max}|\mathrm{Im}(\lambda_\nu(q))|/h$ as a function of the quadratic Zeeman effect q for the case when the axisymmetric axis is parallel or perpendicular to the magnetic field and when there is no DDI. Note that for all cases, the instability rate experiences a pronounced maximum contrary to the homogeneous case. This maximum, as already discussed in previous chapters, is induced by the inhomogeneous harmonic trapping and leads to marked resonances in the q-dependence of the amplification dynamics. However, this instability rate $\Lambda(q)$

clearly depends on the trap orientation confirming indeed the intuitive qualitative picture discussed in Sec. 5.2. When trap axis and magnetic-field are aligned the instability rate, $\Lambda(q)$, decreases compared to the non-dipolar case, whereas the opposite is true when the magnetic field is oriented perpendicular to the trap axis. Note as well that, also as expected from the qualitative picture of Sec. 5.2, the instability region is shifted towards lower q values in the parallel configuration, and towards larger q values in the perpendicular one.

5.4   Amplification dynamics in trapped dipolar spinor condensates

As we have seen in the above discussions, depending on the relative orientation between the trap axis and the dipole-dipole interaction the instability rate increases or decreases compared to the non-dipolar spinor system. This modified instability rate translates into a significantly distorted transfer of atoms into $|\pm 1\rangle$ components, due to the exponential nature of the parametric amplification. In this subsection, we obtain the expression of the transferred rate following the same procedure as in Sec. 3.2.

The time evolution of the quasi-particles operator $\hat{\alpha}_\nu^\pm(t)$ is obtained from the Heisenberg equations of motion

$$i\hbar\frac{d}{dt}\hat{\alpha}_\nu^\pm(t) = \left[\hat{\alpha}_\nu^\pm(t), \hat{H}_1 + \hat{H}_{1,dd}\right]. \tag{5.19}$$

Using Eq. (5.16), we obtain

$$\hat{\alpha}_\nu^\pm(t) = \hat{\alpha}_\nu^\pm(0)e^{-i\lambda_\nu^\pm t/\hbar}. \tag{5.20}$$

As in previous chapters, if for some eigen-energy $\text{Im}(\lambda_\nu^\pm) > 0$, then there is an exponential growth of correlated pairs of atoms in the $|\pm 1\rangle$ components. This exponential growth efficiency is once more best characterized by the instability rate $\Lambda = \max\{\text{Im}(\lambda_\nu^\pm)\}$. Thus, the decrease or increase of the instability rate due to the orientation between the axisymmetric trap and the magnetic-field leads to an exponential decrease or increase of the growth of pairs of atoms in the $|\pm 1\rangle$ components, respectively.

The time evolution of $\hat{a}_{n,\pm 1}$ is then easily obtained

$$\begin{bmatrix} \{\hat{a}_{n1}(t)\} \\ \{\hat{a}_{n-1}^\dagger(t)\} \end{bmatrix} = \mathbf{U}(t)\begin{bmatrix} \{\hat{a}_{n1}(0)\} \\ \{\hat{a}_{n-1}^\dagger(0)\} \end{bmatrix}, \tag{5.21}$$

with $\mathbf{U} = \mathbf{M}^{-1}e^{-i\mathbf{D}t/\hbar}\mathbf{M}$, where $\mathbf{M}$ is the matrix of eigenvectors obtained after solving Eq. (5.17) and $\mathbf{D}$ the corresponding diagonal matrix of eigenvalues.

As discussed in the previous chapter, we consider a BEC initially prepared in the $|0\rangle$ component with possibly an initial spurious classical seed atoms of

$N_s \ll N$ in the $|\pm 1\rangle$ components. Hence, following the same procedure as in Sec. 3.2, the population $P_\pm(t) = \sum_n \langle \hat{a}_{n,\pm1}^\dagger(t)\hat{a}_{n,\pm1}(t)\rangle$ is expressed in the form as $P_\pm(t) = P_C(t) + P_Q(t)$, where

$$P_C(t) = N_s \vec{\chi} \cdot \left(\mathbf{O}^\dagger \mathbf{O} + \widetilde{\mathbf{O}}^\dagger \widetilde{\mathbf{O}}\right) \cdot \vec{\chi}, \tag{5.22}$$

denotes the population triggered by the classical seed, and

$$P_Q(t) = \mathrm{Tr}\left(\widetilde{\mathbf{O}}^\dagger \widetilde{\mathbf{O}}\right), \tag{5.23}$$

denotes the population induced by quantum fluctuations (i.e. when $N_s = 0$). In the previous expressions, the matrices $\mathbf{O}$ and $\widetilde{\mathbf{O}}$ are the upper left and upper right part of the time evolution matrix $\mathbf{U}(t)$ and $\vec{\chi} = (\chi_1, \chi_2, ...)^T$ with $\chi_n = \int d^3 r \psi_0(\vec{r})\phi_n(\vec{r})$ as defined before.

5.4.1 Dipole-induced orientation-dependence of the amplification dynamics

In this subsection we employ the formalism developed in Sec. 5.4 to study the effects of the DDI in the amplification dynamics. We shall show that due to the DDI the amplification may be markedly dependent on the relative orientation, which is given by the angle θ, between the trap axis and the external magnetic field.

In our numerical calculations we have considered realistic experimental conditions, with $N = 10^5$ spin-$f = 1$ ^{87}Rb atoms in a cigar-shaped harmonic potential with $\omega_\perp = 2\pi \times 200$ Hz, and $\omega_\parallel = 2\pi \times 40$ Hz. As mentioned above, we consider the atoms as initially prepared in the $|0\rangle$ component with possibly an initial spurious classical seed $N_s = 2$ in $|\pm 1\rangle$ components. At $t = 0$ the quadratic Zeeman effect q is set to a given value within the instability regime. We monitor the subsequent evolution of the populations $P_{\pm 1}(t)$ obtained from Eqs. (5.22) and (5.23) as a function of q and the relative angle θ between the trap axis and the external magnetic field.

Fig. 5.2 shows the fraction of transferred atoms $P_{\pm 1}(t)/N$ after $t = 115$ ms as a function of quadratic Zeeman effect q for different values of θ. As expected from the form of the instability rate $\Lambda(q)$ we observe the appearance of a maximum for all θ, which is slightly shifted (by approx. 1 Hz) towards lower q when θ is shifted from $\pi/2$ to 0. However, this maximum is approximately more than twice as large for $\theta = \pi/2$ than for $\theta = 0$. The dependence of the amplification on θ is very clearly observable in the θ-dependence of the maximum of $P_{\pm 1}(t)$ (again at $t = 115$ ms) shown in Fig. 5.5. Note that the maximum grows monotonically from $\theta = 0$ to $\theta = \pi/2$.
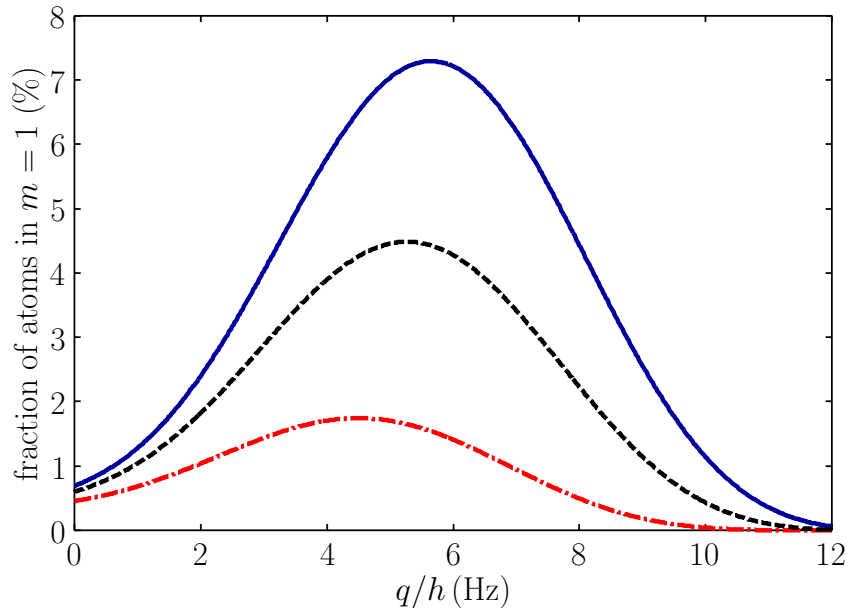
FIGURE 5.2: Fraction of atoms transferrered into $|\pm 1\rangle$ after 115 ms as a function of q for $N_s = 2$ and the same parameters as Fig. 5.1, and for the case of no DDI (black, dashed), $\theta = 0$ (red, solid) and $\theta = \pi/2$ (blue, dot-dashed).
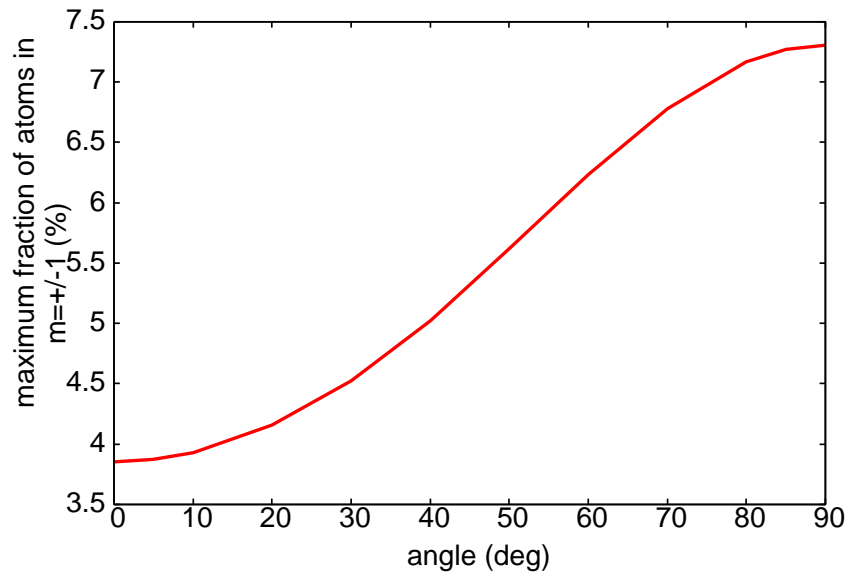

FIGURE 5.3: Maximal fraction of transffered atoms in $|m = \pm 1\rangle$ components after an evolution time of 115 ms as a function of θ (same parameters as Fig. 5.2).

5.5 Effects of magnetic field gradients on the amplification dynamics

As mentioned in Sec. 1.2.3 the homogeneous linear Zeeman effect (LZE) plays typically no role in the spinor dynamics (only at very low magnetic fields $B < 1$ mG the DDI could induce the equivalent of the Einstein-de Haas effect [89, 114], and in this case the residual LZE could play a role). However, magnetic field gradients cannot be gauged out, and may play a relevant role in the spinor physics [91]. In this section, we analyze the effects that these gradients may have on the amplification dynamics. We shall show that even relatively weak gradients may have a significant effect on the amplification process.

From Eq. (1.39), the Hamiltonian that account for the magnetic-field gradient is:

$$\hat{H}_{1,\text{gr}} = \sum_m m \nabla p \cdot \int d^3 r \, \hat{\psi}_m^\dagger(\vec{r}, t) \vec{r} \hat{\psi}_m(\vec{r}, t). \tag{5.24}$$

Thus, these magnetic-field gradients do not affect the GP equation for the BEC in $|0\rangle$ component. However, there is indeed a contribution to the effective Hamiltonian for $\delta\hat{\psi}_{\pm1}(\vec{r}, t)$ in the linear regime. This contribution is given by

$$\hat{H}_{1,\text{gr}} = \nabla p \cdot \int d^3 r \left(\delta\hat{\psi}_1^\dagger(\vec{r}, t) \vec{r} \delta\hat{\psi}_1(\vec{r}, t) - \delta\hat{\psi}_{-1}^\dagger(\vec{r}, t) \vec{r} \delta\hat{\psi}_{-1}(\vec{r}, t) \right). \tag{5.25}$$

Expanding this Hamiltonian in the basis of H_{eff}, we obtain

$$\hat{H}_{1,\text{gr}} = \nabla p \cdot \int d^3 r \, \phi_n(\vec{r}) \vec{r} \phi_{n'}(\vec{r}) \left(\hat{a}_{n,1}^\dagger(t) \hat{a}_{n',1}(t) - \hat{a}_{n,-1}^\dagger(t) \hat{a}_{n',-1}(t) \right), \tag{5.26}$$

which may be straightforwardly implemented into the matrix $\mathbf{C}$ of the eigenvalue equation (5.17),

$$\mathbf{C} = \begin{bmatrix} (\epsilon_n + q)\mathbf{1} + \mathbf{B} + \mathbf{D} & -\mathbf{A} + \mathbf{B} \\ \mathbf{A} + \mathbf{B} & -(\epsilon_n + q)\mathbf{1} - \mathbf{B} + \mathbf{D} \end{bmatrix}, \tag{5.27}$$

with $D_{nn'} = \nabla p \cdot \int d^3 r \, \phi_n(\vec{r}) \vec{r} \phi_{n'}(\vec{r})$.

The magnetic-field gradients have two main effects. On one side, they modify the effective potential $V_{eff}(\vec{r})$ in a different way for $m = 1$ than for $m = -1$. This reduces the overlap of the atomic clouds in the $|\pm1\rangle$ components with the BEC in $|0\rangle$ component and hence the scattering mediated transfer. This reduction is stronger for the short-range spin-changing collisions compared to the long-rage DDI, since non-overlapping clouds interact solely due to the nonlocal DDI. On the other side, atoms placed at different locations experience different Larmor precession frequencies. Although this does not affect the local short-range interactions, it does modify the non-local DDI. For large-enough

gradients this may lead to a time-averaged DDI [91]. For weak gradients, as those considered below, the explicit time dependence induced by the gradients must be considered.

Parametric amplification is handicapped by the presence of gradients as a result of these two combined effects. Fig. 5.4 shows the combined effect of the DDI and the magnetic-field gradient along the weak trap axis for $\theta = \pi/2$. As expected, we obtain a reduction of the transfer maximum with increasing gradient and a shift of its position to lower q by approximately 1.5 Hz for a gradient of 10 mG/cm. Hence the transfer maximum is shifted down and to lower q with decreasing θ and increasing gradient. As shown in Fig. 5.5, in the presence of a magnetic field gradient the maximum of $P_{\pm 1}(t)$ shows also a marked θ dependence.

Hence, even rather weak gradients (< 10 mG/cm) may largely modify the amplification dynamics, an effect which is enhanced by the presence of the DDI. Although as mentioned above, the θ-dependence should reveal also in the presence of gradients the effects of the DDI, slight variations of the magnetic field gradients (of the order of few mG/cm) when changing the magnetic-field orientation with respect to the trap axis must be very carefully controlled. This is indeed a crucial point, since otherwise, accidental θ-dependences of the magnetic-field gradients may obscure the physical θ-dependence characteristic of the DDI.
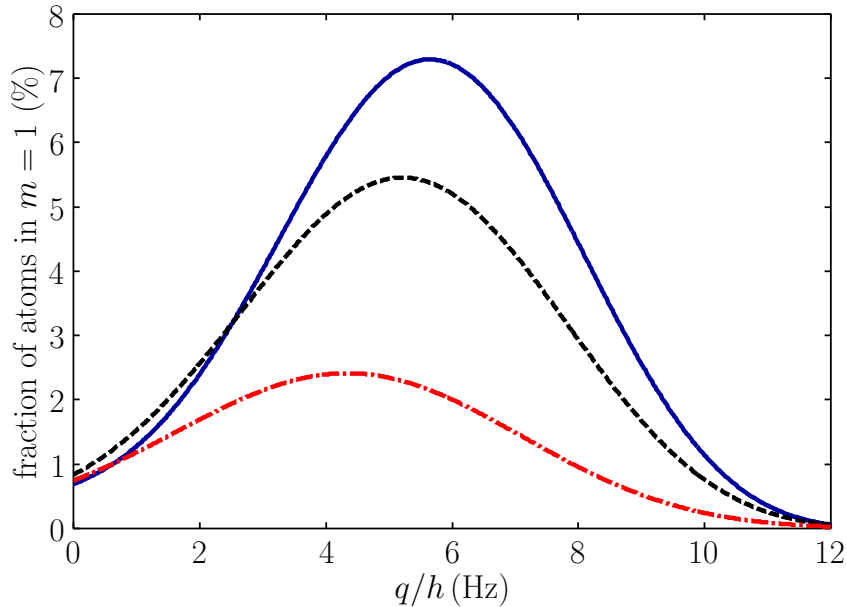

FIGURE 5.4: Fraction of atoms in $|\pm 1\rangle$ after a time 115 ms (same parameters as Fig. 5.2) as a function of q for $\theta = \pi/2$, and for gradients $\nabla B = 0$ (blue, solid), 5 mG/cm (black, dashed) and 10 mG/cm (red, dot-dashed).
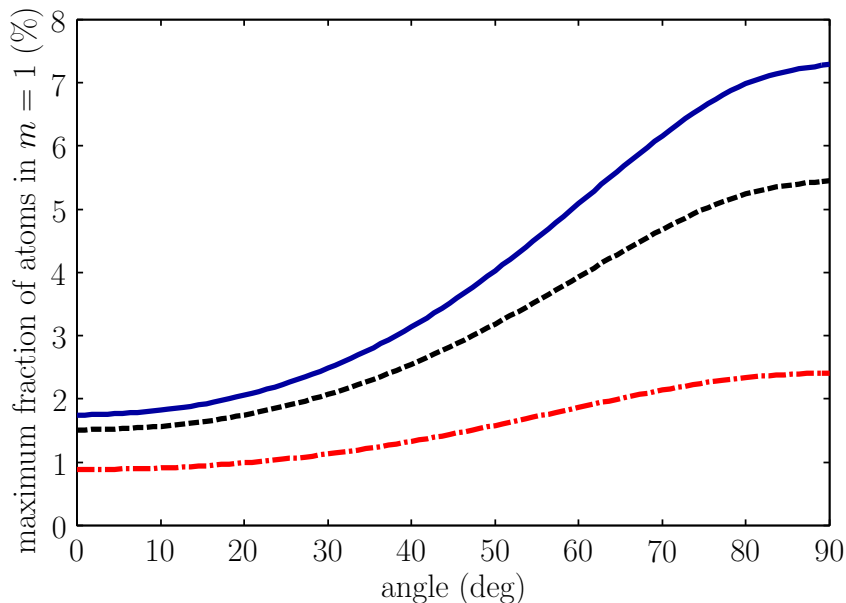
FIGURE 5.5: Maximal population transfer after $115\,\mathrm{ms}$ as a function of θ (same parameters as Fig. 5.2) for different magnetic field gradients $\nabla B = 0$ (blue, solid), $5\,\mathrm{mG/cm}$ (black, dashed) and $10\,\mathrm{mG/cm}$ (red, dot-dashed).

5.6 Experimental requirements

In the following we outline the general requirements to perform an experiment with F=1 ^{87}Rb to probe the theoretical results discussed above. A BEC in $|0\rangle$ component must be prepared in a crossed dipole trap following the same procedure detailed in Refs. [100]. The state preparation requires particular attention, since the classical atoms in $|\pm 1\rangle$ components may strongly alter the experimental result. Previous experiments have shown that the number of classical seed atoms in $|\pm 1\rangle$ components can be suppressed to $N_s \approx 2$ by briefly applying a strong magnetic field gradient to purify the system [100]. Due to the nature of the quadratic Zeeman effect in spin-1 ^{87}Rb, magnetic-fields can be used to access positive values of q, as required above.

As discussed in Sec. 5.5, the most significant requirement compared to previous experiments is related to the suppression of magnetic field gradients which could obscure the dipolar effects. Appropriate experiments should be carefully designed to minimize all sources of field gradients from the vicinity of the atomic sample (alternatively a magnetic shield could be placed around the sample). In state of the art precision measurements, field gradients are commonly suppressed below 1mG/cm [128], which is sufficient to realize the mandatory experimental conditions (see Sec. 5.5).

Fig. 5.2 shows that the fraction of transferred atoms into $|\pm 1\rangle$ components depends strongly on the relative orientation of the weak trap axis and the

external magnetic field. Since it is difficult to change the orientation of a dipole trap while maintaining its trapping potential, experiments must be designed to variate the orientation of the external magnetic field. In this sense, two sets of Helmholtz coils are necessary to provide a homogeneous external magnetic field. One of them should be placed along the weak axis of the trapping potential to realize the $\theta = 0$ configuration and another one along one of the strong axis to realize the $\theta = \pi/2$ case. Both magnetic fields have to be calibrated, preferentially using precision microwave spectroscopy between the ground state hyperfine manifolds of ^{87}Rb. Such an experimental apparatus would also allow for a rotation of the field, since the currents in the two Helmholtz coils could be adjusted to obtain a relative angle θ. In this way, it should be possible to perform a measurement analogous to that discussed in Fig. 5.5. Finally, additional magnetic field gradients can be applied along both magnetic field directions to observe the suppression shown in Fig. 5.4. By changing the strength and orientation of these gradients the effect of additional external gradients could be evaluated and, if necessary, compensated.

Spontaneous breaking of space and spin symmetries in spinor BEC

Spontaneous symmetry breaking is fundamental in disparate scenarios in physics ranging from cosmology [129] and particle physics [130] to liquid crystals [131] and superfuid Helium [132]. Symmetry breaking is also crucial in Bose-Einstein condensates (BECs), where $U(1)$ (phase) symmetry is spontaneously broken. Even more interesting, quantum gases provide unprecedented possibilities for the study of non-equilibrium dynamics, and in particular for the detailed analysis of dynamical symmetry breaking, including the formation of topological defects via Kibble-Zurek mechanism [129, 132, 133].

We have seen in the previous chapters that the spinor BEC prepared in a special initial state acts as a parametric amplifier. Parametric amplification of quantum fluctuations constitutes a fundamental scenario for symmetry breaking, and hence spinor BECs constitute an exciting scenario for the study of spontaneously broken symmetries. In a recent seminal experiment [133] the sudden quench of a spinor BEC from a polar into a ferromagnetic phase was followed by the formation of ferromagnetic domains and topological defects in the transverse magnetization, whereas the longitudinal magnetization remained negligible. Reference [133] provided a major insight in the formation of topological defects, but the nature of the symmetry breaking mechanism remained largely unexplored.

In this chapter, we study the nature of the symmetry breaking in a spin-2 ^{87}Rb BEC initially prepared in $|0\rangle$ state during the amplification of quantum fluctuations. Interestingly, a twofold spontaneous breaking of spatial and $+1$ and -1 spin symmetries may occur. On one hand, we show that quantum fluctuations of the relative phase between amplified degenerate spin modes may break the cylindrical symmetry imposed by the trap. On the other hand, contrary to the situation in reference [133], the density profiles in $|+1\rangle$ and $|-1\rangle$ may differ from each other, leading to spontaneously formed longitudinal magnetization patterns only if various nondegenerate spin modes are significantly amplified. We show that this novel type of spin-symmetry breaking is linked to quantum interferences occurring during the amplification process.

The chapter is structured as follows. In Sec. 6.1 we develop and analyze the eigen-states and eigen-values of the linear Hamiltonian in the case of a 2D-

circular box trap. A qualitative understanding of the two ways of spontaneous symmetry breaking is obtained using density-density correlation functions in Sec. 6.2. In Sec. 6.3 we introduce order parameters to characterize the breaking of symmetries for different values of the quadratic Zeeman effect q. The corresponding numerical results for a cylindrical harmonic trap are presented in Subsec. 6.3.1. Finally the comparison of our results with the experimental results is discussed in Sec. 6.4.

6.1   Two-dimensional circular box-trap

In this section we develop the expression of the spin excitations $\delta\hat{\psi}_m(\vec{r}, t)$ and the eigen-energies of the effective Hamiltonian $\hat{H}_{\pm 1}$ (see Eq. (2.6)), which describe the linear regime dynamics of the pair-creation of atoms in $|\pm 1\rangle$ components, in a two-dimensional circular box trap.

As it was discussed in previous chapters, we consider the initial BEC in $|0\rangle$ as a classical field $\sqrt{n_0(\vec{r})}$, whereas the excitations in the $|\pm 1\rangle$ are represented by the operators $\delta\hat{\psi}_{\pm 1}(\vec{r}, t)$. Moreover, we consider the fact that the population in the $|\pm 1\rangle$ components remains small compared to that in the $|0\rangle$ component and hence the first stages of the dynamics may be described by means of a Bogoliubov approximation of Eq. (2.3) and the effective Hamiltonian of Eq. (2.6).

In the following we consider that the condensate is trapped in a 2D circular box trap of the form given by

$$V(\vec{r}) = \begin{cases} 0 & \rho < R \\ \infty & \rho \geq R \end{cases} \tag{6.1}$$

Where R is the radius of the circular box and $\rho = \sqrt{x^2 + y^2}$. Note that in this case it is easy to see that in the Thomas-Fermi regime the effective potential $V_{eff}(\vec{r})$ (see chapter 2) is constant, i.e. $V_{eff}(\vec{r}) = U_{1-1}n_0$ within the circular region $\rho < R$ and $V_{eff}(\vec{r}) = \infty$ for $\rho \geq R$.

The eigenfunction of $\hat{H}_{eff}(\vec{r})$, in this case, is then decomposed into radial and angular part, which is expressed as

$$\varphi_{nl}(\rho, \phi) = R_{nl}(\rho)e^{il\phi}, \tag{6.2}$$

where each mode is identified by two quantum numbers n and l for the radial excitation and the orbital angular momentum. Employing Eq. (6.2) into the energy eigenvalue equation, $\hat{H}_{eff}\varphi_{nl}(\rho, \phi) = \epsilon_{nl}\varphi_{nl}(\rho, \phi)$, and taking into account the two-dimensional Laplacian equation, after some calculations, we obtain

$$\left[-\frac{\hbar^2}{2M}\left(\frac{d^2}{d\rho^2} + \frac{1}{\rho}\frac{d}{d\rho} - \frac{l^2}{\rho^2} \right) - U_{1-1}n_0 \right] R_{nl}(\rho) = \varepsilon_{nl}R_{nl}(\rho), \tag{6.3}$$

which leads to

$$\rho^2 \frac{d^2}{d\rho^2} R_{nl}(\rho) + \rho \frac{d}{d\rho} R_{nl}(\rho) + \left[\frac{2M}{\hbar^2} \left(\varepsilon_{nl} - U_{1-1} n_0 \right) \rho^2 - l^2 \right] R_{nl}(\rho) = 0, \quad (6.4)$$

which is the well known Bessel differential equation, whose solutions are of the form

$$R_{nl}(\rho) = \frac{1}{\sqrt{\pi} R J_{|l|+1}(\beta_{n|l|})} J_l(\beta_{n|l|} \frac{\rho}{R}), \quad (6.5)$$

where $J_{|l|}$ is the Bessel function of the first kind and $\beta_{n|l|}$ represents the nth zero of $J_{|l|}$.

Therefore, the eigenfunctions of $\hat{H}_{eff}$ become

$$\varphi_{nl}(\rho, \phi) = \frac{1}{\sqrt{\pi} R J_{|l|+1}(\beta_{n|l|})} J_l(\beta_{n|l|} \frac{\rho}{R}) e^{il\phi}, \quad (6.6)$$

with the corresponding eigen-energies of the form

$$\varepsilon_{n,l} = U_{1-1} n_0 + \frac{\hbar^2}{2MR^2} \beta_{n|l|}^2. \quad (6.7)$$

One can easily see that $\varepsilon_{n,l} = \varepsilon_{n,-l}$, and thus modes with the same n and opposite non-zero l and $-l$ are degenerate. This degeneracy is particularly important in the discusions of breaking of symmetries in Sec. 6.2.

Expanding the field operators $\delta\hat{\psi}_m(\vec{r}, t) = \sum_{nl} \varphi_{nl}(\rho, \phi) \hat{a}_{n,l,m}(t)$, the linear Hamiltonian of Eq. (2.6) splits into $\hat{H} = \sum_{n|l|} H_{n|l|}$, where

$$\begin{aligned} \hat{H}_{n|l|} &= (\varepsilon_{n|l|} + q) \sum_{m,l=\pm|l|} a_{n,l,m}^\dagger \hat{a}_{n,l,m} & (6.8) \\ &+ U_{1-1} n_0 \left(\hat{a}_{n,l,1}^\dagger \hat{a}_{n,-l,-1}^\dagger + \hat{a}_{n,-l,1}^\dagger \hat{a}_{nl,-1}^\dagger + \text{h.c.} \right). \end{aligned}$$

This Hamiltonian may be easily diagonalized, being characterized by the eigen-energy function of the form

$$\xi_{n,l}^2 = \left(\frac{\hbar^2}{2MR^2} \beta_{n|l|}^2 + q - q_{cr} \right)^2 - q_{cr}^2, \quad (6.9)$$

with $q_{cr} = -U_{1-1} n_0$. As in previous chapters, if $\xi_{n,l}$ is real the (n,l)-mode may be considered stable, whereas an imaginary $\xi_{n,l} = i|\xi_{n,l}|$ denotes instability. The (n,l)-mode is unstable for

$$-\frac{\hbar^2}{2MR^2} \beta_{n|l|}^2 < q < 2q_{cr} - \frac{\hbar^2}{2MR^2} \beta_{n|l|}^2. \quad (6.10)$$
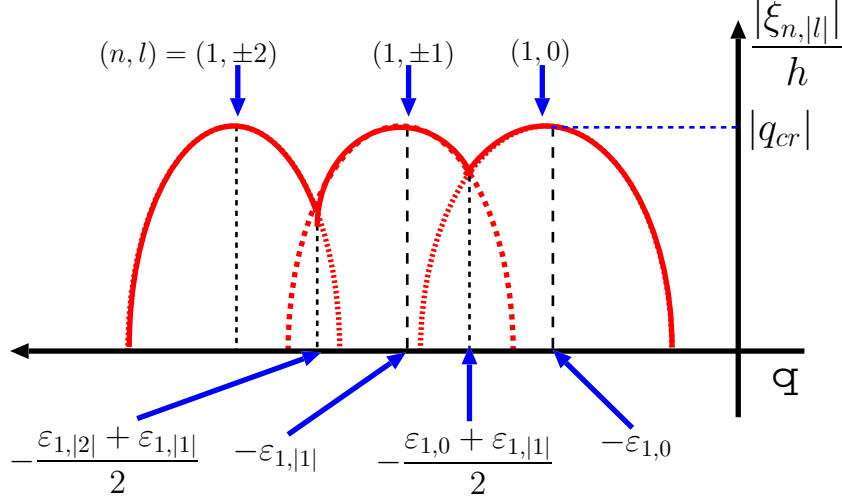
FIGURE 6.1: The instability rate for a spin-2 ^{87}Rb BEC in a 2D-circualr box trap. The solid curve is the maximal instability rate. This curve belongs to the most unstable $(1,0)$-mode in the region $-\frac{\varepsilon_{1,0}+\varepsilon_{1,|1|}}{2} < q < q_{cr}-\varepsilon_{1,0}$, then to the degenerate most unstable $(1,\pm1)$-modes in the region $-\frac{\varepsilon_{1,|1|}+\varepsilon_{1,|2|}}{2} < q < -\frac{\varepsilon_{1,0}+\varepsilon_{1,|1|}}{2}$ and soon. Besides to the degenerate most unstable modes, there may also non-degenerate equally unstable modes like $(1,\pm1)$ and $(1,0)$ at $q = -\frac{\varepsilon_{1,0}+\varepsilon_{1,|1|}}{2}$ and $(1,\pm1)$ and $(1,\pm2)$ at $q = -\frac{\varepsilon_{1,|1|}+\varepsilon_{1,|2|}}{2}$

As it was discussed in Chapter 3, the maximal instability occurs when $q = -\varepsilon_{n,|l|}$, as shown in Fig. (6.1). The solid curve in Fig. (6.1) is the maximal instability rate as a function of the quadratic Zeeman effect q and it belongs to different most unstable (n,l)-modes for different values of q. Note that modes with the same n and opposite non-zero l and $-l$ are degenerate and hence they are equally unstable (for example the curve that belongs to degenerate most unstable $(1,\pm1)$-modes in the region $-\frac{\varepsilon_{1,|1|}+\varepsilon_{1,|2|}}{2} < q < -\frac{\varepsilon_{1,0}+\varepsilon_{1,|1|}}{2}$ of Fig. (6.1)). On the other hand, modes with different n and n' ($\varepsilon_{n,l} \neq \varepsilon_{n',l'}$) can be approximately equally unstable ($|\xi_{n,l}| = |\xi_{n',l'}|$) (for example $|\xi_{1,0}| = |\xi_{1,-1}|$ at $q = -\frac{\varepsilon_{1,0}+\varepsilon_{1,|1|}}{2}$ as shown in Fig. (6.1)). These two ways of being equally unstable lead to different types of symmetry breaking that will be discussed in the next Sec. 6.2.

In the following, we focus on the unstable modes, since these modes are those related to the onset of spinor dynamics. As it was discussed in Subsec. 2.2.2, for an unstable mode the Hamiltonian of Eq. (6.9) may be re-written as

$$\hat{H}_{n|l|} = \frac{|\xi_{n,|l|}|}{2} \sum_{m,l=\pm|l|} \left[\hat{X}^{(1)}_{n,l,m}(t)\hat{X}^{(2)}_{n,l,m}(t) + \hat{X}^{(2)}_{n,l,m}(t)\hat{X}^{(1)}_{n,l,m}(t) \right], \qquad (6.11)$$

where

$$\hat{X}^{(1,2)}_{n,l,m}(t) = \frac{1}{\sqrt{2\sin(2\theta_{n,l})}} \left(e^{\pm i\theta_{n,l}} \hat{a}_{n,l,m}(t) + e^{\mp i\theta_{n,l}} \hat{a}^{\dagger}_{n,-l,-m}(t) \right), \qquad (6.12)$$

with $\cos(2\theta_{n,l}) = \frac{(\varepsilon_{n,|l|}+q)}{|q_{cr}|}$. The operators $\hat{X}^{(1,2)}_{n,l,m}(t)$ are quadratures, which satisfy the commutation relation

$$\left[\hat{X}^{(1)}_{n,l,m}(t), \hat{X}^{(2)}_{n,l,m}(t) \right] = i, \qquad (6.13)$$

being linked to the squeezing physics associated to the amplification dynamics. From the Heisenberg equation of motion, the time evolution of these operators is given by:

$$\hat{X}^{(1,2)}_{n,l,m}(t) = e^{\pm|\xi_{n,|l|}|t/\hbar} \hat{X}^{1,2}_{n,l,m}(0). \qquad (6.14)$$

This shows that the quadrature $\hat{X}^{(1)}_{n,l,m}(t)$ is stretched according to $e^{|\xi_{n,|l|}|t/\hbar}$, whereas $\hat{X}^{(2)}_{n,l,m}(t)$ is squeezed as $e^{-|\xi_{n,|l|}|t/\hbar}$. Hence the amplification process corresponding to the unstable (n,l)-mode is characterized by a squeezing parameter $|\xi_{n|l|}|t/\hbar$ and a mixing angle $\theta_{n,l}$. Interestingly, $\theta_{n,l}$, is different for different (n,l)-modes. This turns out to be crucial for understanding of breaking of $+1$ and -1 spin symmetry, which will be discussed in Subsec. 6.2.2.

The time evolution of the operator $\hat{a}_{n,l,m}(t)$ can be obtained by employing Eq. (6.14) into Eq. (6.12), after some calculation, it turns out to be

$$\begin{aligned} \hat{a}_{n,l,m}(t) =& \frac{e^{|\xi_{n,|l|}|t/\hbar}}{2i\sin 2\theta_{n,l}} \left[e^{2i\theta_{n,l}} \hat{a}_{n,l,m}(0) + \hat{a}^{\dagger}_{n,-l,-m}(0) \right] \\ &- \frac{e^{-|\xi_{n,|l|}|t/\hbar}}{2i\sin 2\theta_{n,l}} \left[e^{-2i\theta_{n,l}} \hat{a}_{n,l,m}(0) + \hat{a}^{\dagger}_{n,-l,-m}(0) \right]. \end{aligned} \qquad (6.15)$$

After some evolution time t only the growing part is important. It then follows that

$$\delta\hat{\psi}_m(\rho,\phi,t) = \sum_{nl} \varphi_{nl}(\rho,\phi) \frac{e^{|\xi_{n,|l|}|t/\hbar}}{2i\sin 2\theta_{n,l}} \left[e^{2i\theta_{n,l}} \hat{a}_{n,l,m}(0) + \hat{a}^{\dagger}_{n,-l,-m}(0) \right], \quad (6.16)$$

where only unstable modes are summed.

6.2 Correlation functions in a 2D- circular box-model

In this subsection we employ the formalism developed in Sec. 6.1 to calculate the density-density correlation functions of $|+1\rangle$ and $|-1\rangle$ components after a given evolution time t and for a given quadratic Zeeman effect q.

The density-density correlation function after a given time t can be expressed as

$$\langle \hat{n}_m(\rho, \phi, t) \hat{n}_{m'}(\rho', \phi', t) \rangle = \langle \delta \hat{\psi}_m^\dagger(\rho, \phi, t) \delta \hat{\psi}_m(\rho, \phi, t) \delta \hat{\psi}_{m'}^\dagger(\rho', \phi', t) \delta \hat{\psi}_{m'}(\rho', \phi', t) \rangle.$$
(6.17)

We need to calculate the density-density correlation functions during the amplifications of quantum modes. Hence, we consider the initial state to be a pure quantum state $|vac\rangle$ (with zero spurious seed atoms). Using Eq. (6.16) the above equation takes the form

$$\langle \hat{n}_m(\rho, \phi, t) \hat{n}_{m'}(\rho', \phi', t) \rangle = \sum_{\vec{n}_1, \vec{n}_2, \vec{n}_3, \vec{n}_4} \varphi_{\vec{n}_1}^*(\rho, \phi) \varphi_{\vec{n}_2}(\rho, \phi) \varphi_{\vec{n}_3}^*(\rho', \phi') \varphi_{\vec{n}_4}(\rho', \phi')$$

$$\times \frac{e^{\left[|\xi_{\vec{n}_1}| + |\xi_{\vec{n}_2}| + |\xi_{\vec{n}_3}| + |\xi_{\vec{n}_4}| \right] t/\hbar}}{16 \sin 2\theta_{\vec{n}_1} \sin 2\theta_{\vec{n}_2} \sin 2\theta_{\vec{n}_3} \sin 2\theta_{\vec{n}_4}}$$

$$\times \langle vac| \left[\left(e^{-2i\theta_{\vec{n}_1}} \hat{a}_{\vec{n}_1, m}^\dagger + \hat{a}_{-\vec{n}_1, -m} \right) \left(e^{-2i\theta_{\vec{n}_2}} \hat{a}_{\vec{n}_2, m}^\dagger + \hat{a}_{-\vec{n}_2, -m} \right) \right.$$

$$\left. \left(e^{-2i\theta_{\vec{n}_3}} \hat{a}_{\vec{n}_3, m'}^\dagger + \hat{a}_{-\vec{n}_3, -m'} \right) \left(e^{-2i\theta_{\vec{n}_4}} \hat{a}_{\vec{n}_4, m'}^\dagger + \hat{a}_{-\vec{n}_4, -m'} \right) \right] |vac\rangle,$$
(6.18)

with $\pm \vec{n}_i = (n_i, \pm l_i)$. Evaluating the above equation, we obtain two density-density correlations of the form

$$\langle \hat{n}_m(\rho, \phi, t) \hat{n}_m(\rho', \phi', t) \rangle = \sum_{\vec{n}, \vec{n}'} \frac{e^{2\left(|\xi_{\vec{n}}| + |\xi_{\vec{n}'}| \right) t/\hbar}}{16 \sin^2 2\theta_{\vec{n}} \sin^2 2\theta_{\vec{n}'}} \left\{ |\varphi_{\vec{n}}(\rho, \phi)|^2 |\varphi_{\vec{n}'}(\rho', \phi')|^2 \right.$$

$$\left. + \varphi_{\vec{n}}^*(\rho, \phi) \varphi_{\vec{n}}(\rho', \phi') \varphi_{\vec{n}'}^*(\rho, \phi) \varphi_{\vec{n}'}(\rho', \phi') \right\},$$
(6.19)

which is the density-density correlation of $|\pm 1\rangle$ with itself, and

$$\langle \hat{n}_{-m}(\rho, \phi, t) \hat{n}_m(\rho', \phi', t) \rangle = \sum_{\vec{n}, \vec{n}'} \frac{e^{2\left(|\xi_{\vec{n}}| + |\xi_{\vec{n}'}| \right) t/\hbar}}{16 \sin^2 2\theta_{\vec{n}} \sin^2 2\theta_{\vec{n}'}} \left\{ |\varphi_{\vec{n}}(\rho, \phi)|^2 |\varphi_{\vec{n}'}(\rho', \phi')|^2 \right.$$

$$\left. + \varphi_{\vec{n}}^*(\rho, \phi) \varphi_{\vec{n}}(\rho', \phi') \varphi_{\vec{n}'}^*(\rho, \phi) \varphi_{\vec{n}'}(\rho', \phi') \cos 2(\theta_{\vec{n}} - \theta_{\vec{n}'}) \right\},$$
(6.20)

which is the density-density correlation of $|+1\rangle$ with $|-1\rangle$.

These two previous equations can be expressed in terms of the radial and

angular parts of the wavefunction as

$$
\langle \hat{n}_m(\rho, \phi, t) \hat{n}_m(\rho', \phi', t) \rangle = \sum_{\substack{n,l \\ n',l'}} \frac{e^{2\left(|\xi_{n,|l|}| + |\xi_{n',|l'|}|\right)t/\hbar}}{16 \sin^2 2\theta_{n,l} \sin^2 2\theta_{n',l'}} \Bigg\{ |R_{nl}(\rho)|^2 |R_{n'l'}(\rho')|^2
$$
$$
+ R_{nl}(\rho) R_{nl}(\rho') R_{n'l'}(\rho) R_{n'l'}(\rho')
$$
$$
\times \cos(l - l')(\phi - \phi') \Bigg\}
$$

$$(6.21)$$

and

$$
\langle \hat{n}_{-m}(\rho, \phi, t) \hat{n}_m(\rho', \phi', t) \rangle = \sum_{\substack{n,l \\ n',l'}} \frac{e^{2\left(|\xi_{n,|l|}| + |\xi_{n',|l'|}|\right)t/\hbar}}{16 \sin^2 2\theta_{n,l} \sin^2 2\theta_{n',l'}} \Bigg\{ |R_{nl}(\rho)|^2 |R_{n'l'}(\rho')|^2
$$
$$
+ R_{nl}(\rho) R_{nl}(\rho') R_{n'l'}(\rho) R_{n'l'}(\rho')
$$
$$
\times \cos\{(l - l')(\phi - \phi') + 2(\theta_{nl} - \theta_{n'l'})\} \Bigg\}
$$

$$(6.22)$$

We employ these two equations in the following subsections to understand the key futures concerning the broken symmetries during the amplification dynamics.

6.2.1 Spontaneous breaking of cylindrical spatial symmetry

In this subsection, we study the spontaneous breaking of the cylindrical spatial symmetry during the amplification of quantum fluctuations. This broken symmetry can be understood from Eq. (6.21).

The first obvious fact that may be easily seen from Eq. (6.21) is that not all unstable modes contribute equally. Those with the largest amplification gain $|\xi_{n,|l|}|$ dominate after a transient time. We have seen in Sec. 6.1 that degenerate (n, l)-modes ($\varepsilon_{n,l} = \varepsilon_{n,-l}$), are equally unstable ($|\xi_{n,l}| = |\xi_{n,-l}|$). As a result any linear combination of these modes is equally unstable, being selected from shot to shot by quantum fluctuations, and hence inducing a shot-to-shot spontaneous breaking of the cylindrical symmetry. Of course, the cylindrical symmetry is maximally broken when degenerated modes with non-zero l are the most unstable ones. We have calculated the density-density correlation at two different values of the quadratic Zeeman effect q, to clarify this effect. One is the case at $q = -\varepsilon_{1,0}$, where there is only one maximally unstable $(1, 0)$-mode, and hence there is no breaking of the cylindrical spatial symmetry as shown in Fig. (6.2a). The other is the case at $q = -\varepsilon_{1,|1|}$,

whereby two degenerate most unstable $(1, \pm 1)$-modes exist. In this case, the cylindrical spatial symmetry is broken as shown in Fig. (6.2b).
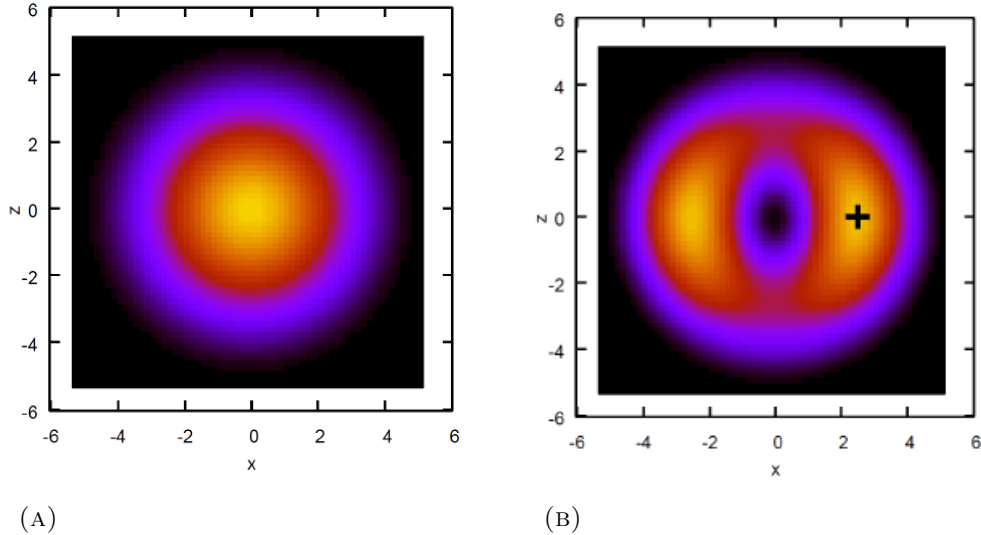

(A)   (B)

FIGURE 6.2: Density-density correlation functions at different quadratic Zeeman effect q. Fig. (6.2a) corresponds to the case at $q = -\varepsilon_{1,0}$, for which there is only one maximally unstable $(1, 0)$-mode. On the other hand, Fig. (6.2b) corresponds to the case at $q = -\varepsilon_{1,|1|}$ whereby two degenerate maximally unstable $(1, \pm 1)$-modes exist. Note that in the first case the cylindrical symmetry is not broken, whereas in the second case it is broken.

6.2.2 Spontaneous breaking of the spin symmerty

Besides to the breaking of cylindrical spatial symmetry, there may also be spontaneous breaking of the $+1$ and -1 spin symmetry during the amplification of quantum fluctuations. In this subsection, we study this broken $+1$ and -1 spin symmetry using Eqs. (6.21) and (6.22).

It is clear from Eqs. (6.21) and (6.22) that the mechanism for the breaking of the $+1$ and -1 spin symmetry is very different to the breaking of the cylindrical spatial symmetry. This breaking of the $+1$ and -1 spin symmetry is directly linked to a quantum interference between unstable modes with different mixing angles $\theta_{n,l}$. Note in particular that degenerate modes ($\varepsilon_{n,l} = \varepsilon_{n,-l}$) posses equal mixing angles, and hence do not contribute to the $+1$ and -1 spin symmetry breaking. Therefore, those states which maximally break the cylindrical symmetry do not contribute to the $+1$ and -1 asymmetry. A maximal $+1$ and -1 symmetry breaking is produced when two non-degenerate modes with $\varepsilon_{n,|l|} \neq \varepsilon_{n',|l'|}$ are approximately equally unstable ($|\xi_{n,|l|}| = |\xi_{n',|l'|}|$), which demands $-q = (\varepsilon_{n,|l|} + \varepsilon_{n',|l'|})/2$, being the most unstable ones. For instance, this breaking of $+1$ and -1 spin symmetry occurs for the case

$q_1 = -\frac{\varepsilon_{1,|1|}+\varepsilon_{1,0}}{2}$, at which the $(1,0)$ mode interferes with $(1,\pm1)$-modes and for $q_2 = -\frac{\varepsilon_{1,|1|}+\varepsilon_{1,|2|}}{2}$, whereby the $(1,\pm1)$-modes interfere with the $(1,\pm2)$-modes.

This spontaneous breaking of the $+1$ and -1 spin symmetry gives rise to fluctuations of local longitudinal magnetization,

$$S_z = \sum_m m\delta\hat{\psi}^\dagger_m(\vec{r},t)\delta\hat{\psi}_m(\vec{r},t) \tag{6.23}$$

contrary to Ref. [133] where S_z was negligible. Fig. (6.3) shows the fluctuations of local magnetization, S_z, at q_1 and q_2 respectively.

(A) (B)
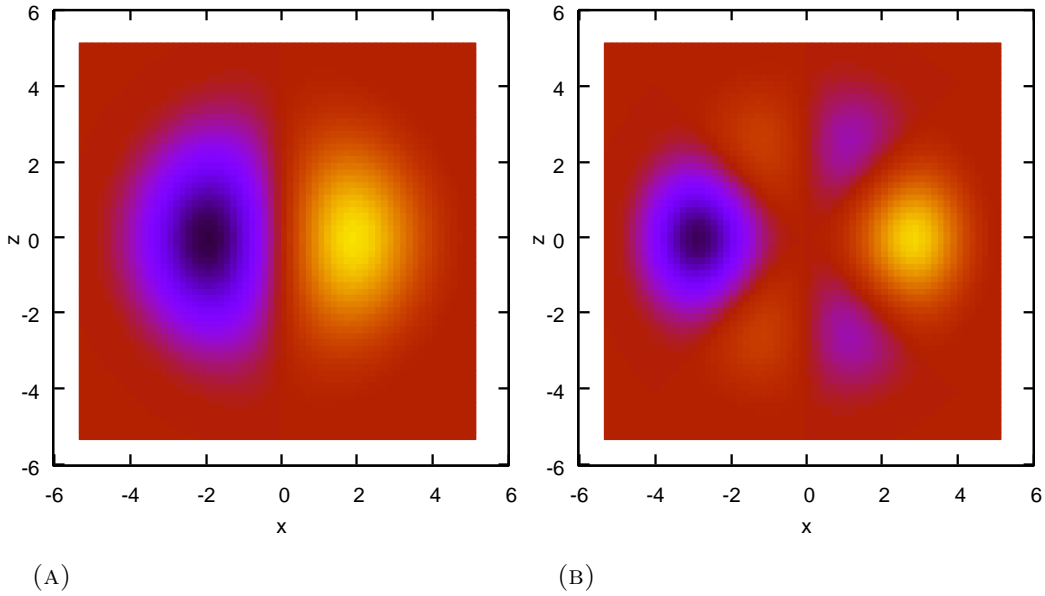
FIGURE 6.3: Fluctuations of the local magnetization at different quadratic Zeeman effect q. Fig. (6.3a) corresponds to the case at q_1 at which two modes of $(1,\pm1)$ and $(1,0)$ are the most unstable ones. Fig. (6.3b) corresponds to the case at q_2 whereby two modes of $(1,\pm1)$ and $(1,\pm2)$ are the most unstable ones. Both cases show that the $+1$ and -1 spin symmetry may be clearly broken.

6.3 Order parameters for the asymmetry of the correlations

In this subsection we study the cylindrical spatial asymmetry and the $+1$ and -1 spin asymmetry of the density profile using various order parameters. These order parameters are particularly important for the characterization of the type of broken symmetry in a trapped system, which will be discussed in Subsec. 6.3.1, and in the discussions of the experimental results.

The first order parameter that we use to study the cylindrical spatial asymmetry of the $|\pm 1\rangle$ density cloud is defined as

$$G_{m,m}^{\Delta l} = \frac{\int d^3\vec{r} \int d^3\vec{r}' \langle \hat{n}_m(\vec{r},t)\hat{n}_m(\vec{r}',t)\rangle \cos \Delta l(\phi - \phi')}{\left[\int d^3\vec{r} \langle \hat{n}_m^2(\vec{r},t)\rangle\right]} \tag{6.24}$$

with $\Delta l = l - l' = 2, 4, 6, ...$ This order parameter will be particularly large when two degenerate modes with $l = \frac{\Delta l}{2}$ and $l = -\frac{\Delta l}{2}$ are the most unstable ones. Note that $G_{m,m}^{\Delta l} = 0$ for the case where there is no breaking of cylindrical spatial symmetry.

The other order parameter employed to study the $+1$ and -1 spin asymmetry is

$$\eta = \left| 1 - \frac{\int d^3\vec{r} \langle \hat{n}_1(\vec{r},t)\hat{n}_{-1}(\vec{r},t)\rangle}{\int d^3\vec{r} \langle \hat{n}_1(\vec{r},t)\hat{n}_1(\vec{r},t)\rangle} \right|. \tag{6.25}$$

Note that $\eta = 0$ when the $+1$ and -1 densities are locked to each other, i.e. when there is no breaking of the $+1$ and -1 spin symmetry, but $\eta \neq 0$ when the $+1$ and -1 spin symmetry is broken.

We have calculated numerically the above two order parameters for a spin-2 ^{87}Rb BEC trapped by 2D-circular box trap. We considered $N = 10^5$ atoms and $2\pi \times (1, 50, 1)$ Hz frequencies in order to check that our numerics gives the results of the previous discussions.
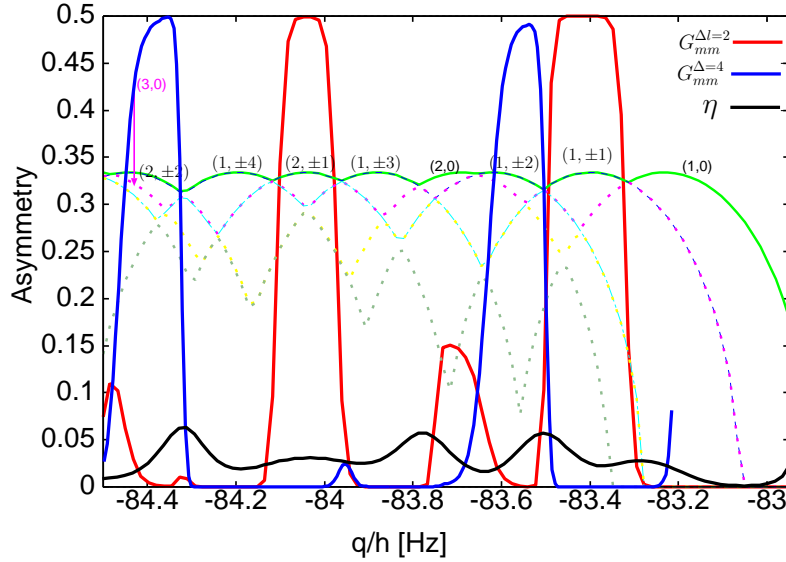
FIGURE 6.4: Cylindrical spatial and the $+1$ and -1 spin asymmetry as a function of quadratic Zeeman effect q for the given artificial parameters (see text). $G_{mm}^{\Delta l=2,4}$ is the cylindrical spatial asymmetry for the modes with $\Delta l = 2$ and 4 and η is the $+1$ and -1 spin asymmetry.

Fig. (6.4) shows the cylindrical spatial asymmetry and the $+1$ and -1 spin asymmetry as a function of quadratic Zeeman effect q. The red curve, i.e. $G_{mm}^{\Delta l=2}$,

corresponds to cylindrical spatial asymmetry i.e. for the lower modes with $l = \pm 1$. As it was discussed in Subsec. 6.2.1, the curve shows a maximum breaking of cylindrical spatial symmetry at the values of q where the degenerate $(1, \pm 1)$ and $(2, \pm 1)$ modes are located. The cylindrical asymmetry for higher modes with $l = \pm 2$ is given by the blue curve ($G_{mm}^{\Delta l=4}$) and it shows a maximum breaking of cylindrical spatial symmetry for the values of q, at which the degenerate $(1, \pm 2)$ and $(2, \pm 2)$ modes are located.

The black curve in Fig.(6.4) shows the breaking of $+1$ and -1 spin symmetry. It shows that there is a relative maximum breaking of the $+1$ and -1 spin symmetry at the values of q whereby two non-degenerate unstable modes are equally unstable, like in the case at values of q where two non-degenerate modes cross each other, as expected from the discussion of Subsec. 6.2.2.

6.3.1   Results in the trapped system

In this subsection, we study the breaking of the above two types of symmetries during the amplification of quantum fluctuations for realistic experimental parameters. To this end, we have performed numerical simulations to calculated the above two order parameters for a spin-2 ^{87}Rb BEC initially containing $N = 5 \times 10^4$ atoms in an optical dipole trap with a cylindrical harmonic trapping potential of frequencies given by $(\omega_x, \omega_y, \omega_z) = 2\pi \times (187, 183, 67)$ Hz.
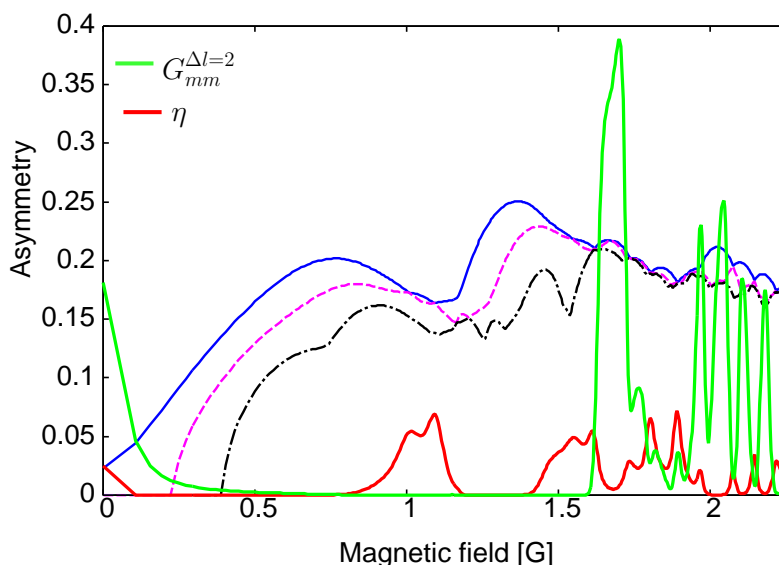

FIGURE 6.5: Cylindrical spatial and $+1$ and -1 spin asymmetry as a function of the magnetic field for the experimental parameters (see text). $G_{mm}^{\Delta l=2}$ corresponds for the cylidrical asymmetry of the $l = \pm 1$ modes and η characterizes for the $+1$ and -1 spin asymmetry.

Fig. (6.5) shows the cylindrical spatial asymmetry (green curve) and the

$+1$ and -1 spin asymmetry (red curve) as a function of the magnetic field after an evolution time of $t = 100$ms. There is a maximum breaking of the cylindrical spatial symmetry around $B = 1.68$G, in which two most unstable rates, which belong to modes with $|l| = 1$, overlap. For the reasons explained in Subsec. 6.2.1 the red curve in Fig. (6.5) shows no breaking of the $+1$ and -1 spin symmetry at the value of $B = 1.68$G at which the cylindrical spatial symmetry is maximally broken. Interestingly, to the right and left of this value of B there is both breaking of cylindrical spatial symmetry and the $+1$ and -1 spin symmetry. This region will be the focus of the qualitative comparison of the experimental results in Sec. 6.4. Around $B = 1$G the $+1$ and -1 spin symmetry is broken without breaking of the cylindrical spatial symmetry. This happen when two modes with $|l| = 0$ are the most unstable ones.

6.4 Comparison with the experimental results

To compare quantitatively the theoretical results with the experimental ones, we have to consider the exact values of the atomic density, trap frequencies, scattering lengths, the atomic losses and the magnetic field gradients. Since these parameters are not known very precisely, in the following we will focus on the qualitative comparison of the theoretical and experimental results.

We consider a spin-2 ^{87}Rb BEC initially containing $N = 5 \times 10^4$ atoms in a cylindrical trapping potential of $2\pi \times (187, 183, 67)$ Hz frequencies.

Figure(6.6a) shows (from left to right) the averaged density profiles of all realizations recorded at the magnetic field of $B = 0.64$G, 0.9G, 1.3G, 1.7G, 2.0G and $2.3G$ respectively. As expected, the averaged density profiles show spatial cylindrical symmetry and a spin symmetry under the interchange $|+1\rangle$ and $|-1\rangle$. Figure (6.6b) shows an individual realization at the above given values of B. It is clear from Fig. (6.5) that at the values of $B = 0.64$G, 1.3G and 2.0G there is only one maximally unstable mode ($l = 0$), and hence the clouds remain cylindrically symmetric at these values even in individual realizations. However, at around $B = 1.7$G there are two equally maximally unstable modes, $|l| = 1$, which allows for a clockwise rotation (vortex) or an anticlockwise one (antivortex). As a result the relative strength of vortex-antivortex mode is chosen from shot-to-shot by quantum fluctuations, and hence inducing a shot-to-shot spontaneous breaking of the cylindrical symmetry as shown in Fig. (6.6b).

Note that at lower values of the magnetic field B, as it was discussed in Chapter 4, the spurious seeds influences the production of population in $|\pm1\rangle$, moreover at these values of B the experimental clouds are very sensitive to small magnetic field gradients (see Ref.[134] for experimental details).

Therefore, the symmetry breaking during the amplifications of quantum
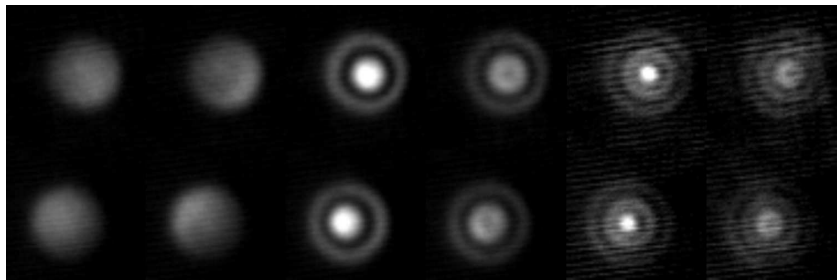
(A)
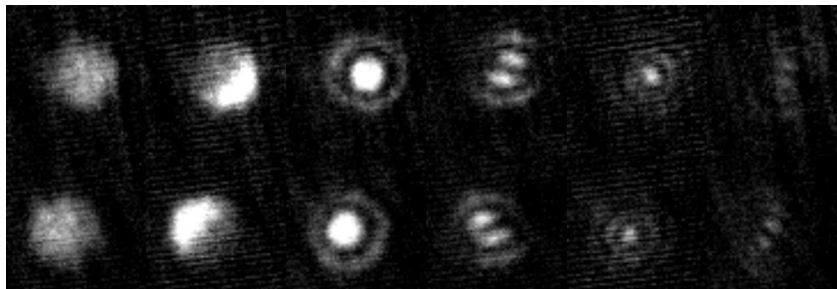
(B)

FIGURE 6.6: The experimental density distributions $|+1\rangle$ and $|-1\rangle$ clouds at the above given magnetic fields (see text) after time-of-flight expansion. (6.6a) corresponds to the averaged experimental density profiles. (6.6b) shows an individual experimental realization.

fluctuation is best studied at higher magnetic fields. Accordingly, experimental measurments were taken at four magnetic field values between 1.68G and 1.84G to evaluate the symmetry breaking process (see Ref. [134] for experimental details). At these values of B the density profiles show qualitative form as that at $B = 1.7$G in Fig. (6.6b). Note that the density profile of each component has a defined density node at the center, which is oriented in a particular direction. The angle between this direction and a fixed axis was measured experimentally for a large number of realizations.

Fig. (6.4) is a histogram that shows the distribution of angles for $|1\rangle$ and $|-1\rangle$ as well as the difference between these angles. All angles of the $|\pm1\rangle$ clouds occur with roughly the same probability, showing that the cylindrical symmetry is indeed spontaneously broken. This matches reasonably well with our result in Fig. (6.5) for the magnetic field values between 1.6G and 1.8G.
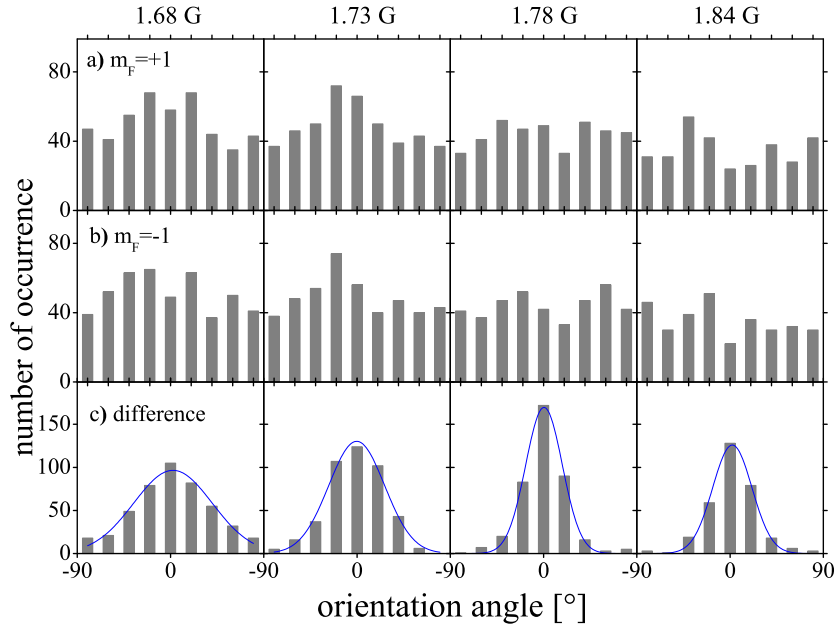
FIGURE 6.7: The orientation of individual density distributions recorded at four magnetic field values bewteen 1.68G and 1.84G. (a) and (b) The distribution of angles for the $|1\rangle$ and $|-1\rangle$ states. (c)The distribution of the difference between the angles of orientation.

The relative angle in Fig. (6.4) shows an intriguing behaviour. At 1.78G, the two angles are locked to each other and hence there is no significant breaking of the $+1$ and -1 spin symmetry. However, towards lower and higher magnetic fields, the locking relaxes and different angles become more probable. Such realizations with different orientations of the density distributions in $|1\rangle$ and $-1\rangle$ break the spin symmetry of the density profiles. Note, again, that this observation is in good agreement with our numerical results of Fig. (6.5), where a dip in η was expected for the maximum of $G_{mm}^{\Delta l=2}$ at approximately the values observed experimentally.

Conclusion and outlook

In this thesis, we have studied the parametric amplification of matter-waves on the basis of spinor BECs. Spinor dynamics is particularly interesting for the case of condensates initially prepared in the $|0\rangle$ Zeeman sublevel. In that case, spin-changing collisions may lead to correlated pair-creation of atoms into $|\pm 1\rangle$, in a process which closely resembles parametric down conversion in non-linear optics. As a result, spinor condensates may act as parametric amplifiers of matter waves, opening interesting perspectives for the creation of nonclassical states of matter based on spinor BECs. In this thesis we have studied how the amplification dynamics crucially depends on the interplay between trapping potential, quadratic Zeeman effect q, magnetic-field gradients, spin-changing collisions and DDI. Furthermore, we have investigated its sensitivity with respect to quantum spin fluctuations and the spontaneous breaking of space and spin symmetries in the parametrically amplified clouds in $|\pm 1\rangle$.

We detail in the following the main results of this thesis:

In Chapter 2, we have studied the first stages (linear regime) of the spinor dynamics (without the DDI and the magnetic-field gradient) by analyzing the properties of the Bogoliubov spectrum of spin excitations of the initial condensate in the $|0\rangle$ Zeeman sublevel for both spin-1 and spin-2 ^{87}Rb homogenous spinor BECs. The BEC in $|0\rangle$ is stable or unstable depending on the quadratic Zeeman effect q. The instability of the condensate leads to the pair-creation of atoms into $|\pm 1\rangle$ Zeeman sublevel. This pair-creation efficiency is characterized by the instability rate, which is obtained from the most unstable spin excitation modes. This instability rate is growing for small $|q|$ and acquired its maximum value at certain value of $|q|$, and from that point on, for large $|q|$ it remains constant.

In Chapter 3, we have studied the influence of the trapping potential on the instabilitiy rate. On the contrary to the homogenous case, we have shown that the magnetic field dependent instability rate has a non-monotonous character, which mostly results from the finite size and inhomogeneity of both the trapping potential and the density of the BEC in the $|0\rangle$. This trap-dependent modulation of the instability rate is directly reflected into a strong enhancement or suppression of the pair-creaction efficiency for particular magnetic field values. Accordingly, we have shown that the pair-creation efficiency is characterized by a striking multi-resonant magnetic field dependence, which maps the instability rate (with two particularly strongly enhanced peaks for

the experiments in Hannover). We have shown that the resonant growth can
be initiated by spuriously produced atoms in $|\pm 1\rangle$ and by vacuum spin fluctu-
ations (These triggering mechanisms were discussed in Chapter 4.), and hence
the relative importance of the resonance strengths is controlled accordingly.
Furthermore, we have studied the mean-field calculations of the pair-creation
efficiency using coupled GPEs. These results clearly failed to reproduce the
high magnetic-field resonance resulting from the quantum calculation, due to
the lack of quantum fluctuations in the GPEs calculation. Finally, we directly
compared our results with the experimental results and showed an excellent
agreement.

In Chapter 4, we have studied the triggering mechanism of the amplifica-
tion dynamics (with particular emphasis on spin-2 ^{87}Rb). We have shown that
the classical seed atoms, which are spuriously produced atoms in $|\pm 1\rangle$, are
highly relevant at low magnetic-fields, for which the amplified spin excitation
mode has a large overlap with the original BEC. However, at larger magnetic-
fields the amplified spin excitations show pronounced spatial structures and
lack a substantial overlap. As a result, the amplification dynamics is insensi-
tive to the presence of classical seed atoms, and hence dominantly triggered
by quantum vacuum fluctuations. Thus the system acts as a matter-wave
amplifier for the vacuum fluctuations. These results were also in an excellent
agreement with the experiments in Hannover university.

In Chapter 5, we have studied the effect of the DDI and the magnetic field
gradient on the amplifications dynamics. We have shown that, in spite of the
very small magnetic moment, the magnetic DDI may lead to a strong mod-
ification of the amplification dynamics in spin-1 ^{87}Rb due to the low-energy
scale of the spin-changing collisions. We have shown that the DDI induce a
very marked dependence of the amplification gain with respect to the relative
orientation between magnetic-field direction and trap axis. If both directions
are perpendicular to each other the amplification dynamics is much faster than
for the parallel configuration. Remarkably, the number of transferred atoms
into $|\pm 1\rangle$ may increase for spin-1 ^{87}Rb for a fixed holding time of around
100ms by a factor over 400% when turning from a parallel to a perpendicular
configuration. We have shown as well that magnetic-field gradients may also
significantly modify the amplification dynamics, both due to their effects on
the trapping and on the DDI. As a result, magnetic-field gradients must be
carefully controlled, since uncontrolled changes in the gradient when turn-
ing the magnetic field orientation may obscure the orientation dependence of
the DDI effects on the amplification. This demands specific requirements for
future experiments.

In Chapter 6, we have studied a nontrivial double spontaneous symmetry
breaking during the amplification of quantum fluctuations in $|\pm 1\rangle$ in spin-2
^{87}Rb. On one hand, we have shown that the cylindrical spatial symmetry
introduced by the trap is broken when amplification dynamics is dominated

by degenerate most unstable spin modes, since any linear combination of these modes is equally unstable, being selected from shot to shot by quantum fluctuations, and hence inducing a shot-to-shot spontaneous breaking of the cylindrical symmetry. On the other hand, if the amplification dynamics is dominated by at least two non-degenerate most unstable spin modes, spontaneously formed longitudinal magnetization patterns appear due to quantum interferences between the different amplified quadratures. These nontrivial double spontaneous symmetry breaking was recently observed in experiments at Hannover University.

Our results on parametric amplification using spinor condensates open fascinating perspectives for the creation and analysis of non-classical state of matter. This possibility will be explored in the next future in close collaboration with the experimental group at the Leibniz University of Hannover. For example, relative and total number fluctuations should show interesting statistical properties. Recently, we have studied the number statistics of the parametrically amplified clouds in $|\pm 1\rangle$ of spin-2 ^{87}Rb and in particular the so called Q-paramter [135] given by

$$Q = \frac{\langle (\Delta \hat{N})^2 \rangle - \langle \hat{N} \rangle}{\langle \hat{N} \rangle}, \tag{7.1}$$

where $\langle (\Delta \hat{N})^2 \rangle = \langle \hat{N}^2 \rangle - \langle \hat{N} \rangle^2$ with $\hat{N} = \hat{N}_{+1} + \hat{N}_{-1}$ the total number of atoms in $|\pm 1\rangle$. Note that for Q in the range $-1 \leq Q < 0$ the statistics is sub-Poissonian, and if $Q > 0$, super-Poissonian. Fig.(7.1) shows the Q-parameter as a function of the quadratic Zeeman effect q for spin-2 ^{87}Rb BEC of $N = 5 \times 10^4$ atoms in a trap of frequencies $(w_x, w_y, w_z) = 2\pi \times (176, 132, 46)$ Hz with scattering lengths $a_0 = 87.685 a_B, a_2 = 91.049 a_B, a_4 = 99.197 a_B$. It clearly shows that, except for very low magnetic fields, the number statics is super-Poissonian. Particularly, it is more super-Poissonian around the second resonance (high magnetic field resonance), and hence there is a very large number fluctuations around this region.

The statistics of the relative number $\hat{N}_r = \hat{N}_{+1} - \hat{N}_{-1}$ is even more interesting, being at the moment investigated in close collaboration with the experimental group at the Leibniz University of Hannover.
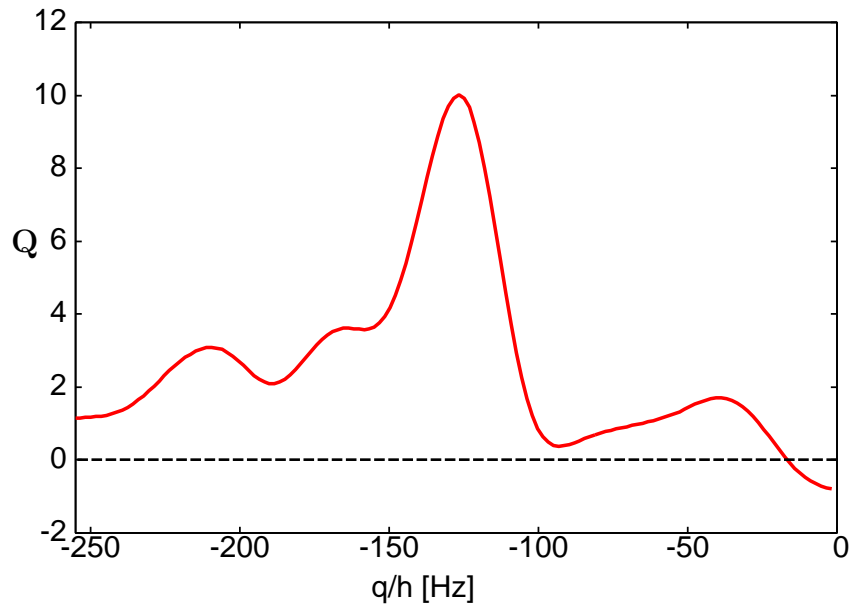
FIGURE 7.1: The Q-paramter as a function of quadratic Zeeman effect q for the given parameters (see text). Except at very low $|q|$, the number statistics is super-Poissonian.

Operator Identities

In this appendix we derive some important relations, which are useful in the discussion of the Hamiltonian employed in Chapters 1 and 2.

The projection operator onto a two-particle state with total with total spin-F is expressible as:

$$\hat{P}_F = \sum_{m_F=-F}^{F} |F, m_F\rangle\langle F, m_F|. \tag{A.1}$$

Using the following orthogonality relations of the Clebsch-Gordan coefficients:

$$\sum_{F=0,2}^{2F} \sum_{m_F=-F}^{F} \langle f_1, m_1; f_2, m_2|F, m_F\rangle\langle F, m_F|f_1, m_3; f_2, m_4\rangle = \delta_{m_1 m_3}\delta_{m_2 m_4}. \tag{A.2}$$

and the closure relationship of the projection operator, one can see that

$$\sum_{F=0,2}^{2F} \lambda_F \hat{P}_F = \sum_{F=0,2}^{2F} \sum_{m_F=-F}^{F} \lambda_F \langle f_1, m_1; f_2, m_2|F, m_F\rangle\langle F, m_F|f_1, m_3; f_2, m_4\rangle \tag{A.3}$$

with $\lambda_F = \frac{1}{2}[F(F+1) - 2f(f+1)]$.

Inserting λ_F into one of the Clebsch-Gordan coefficients gives

$$\begin{aligned}\lambda_F \langle F, m_F|f_1, m_3; f_2, m_4\rangle &= \langle F, m_F|\frac{1}{2}F(F+1) - f(f+1)|f_1, m_3; f_2, m_4\rangle \\ &= \langle F, m_F|\frac{1}{2}(\hat{\vec{F}} - \hat{\vec{f}}_1 - \hat{\vec{f}}_2)|f_1, m_3; f_2, m_4\rangle \\ &= \langle F, m_F|\hat{\vec{f}}_1 \cdot \hat{\vec{f}}_2|f_1, m_3; f_2, m_4\rangle. \end{aligned} \tag{A.4}$$

Up on substituting Eq. (A.4) into Eq. (A.3), we obtain

$$\sum_{F=0,2}^{2F} \lambda_F \hat{P}_F = \sum_{F=0,2}^{2F} \sum_{m_F=-F}^{F} \langle f_1, m_1; f_2, m_2|F, m_F\rangle\langle F, m_F|\hat{\vec{f}}_1 \cdot \hat{\vec{f}}_2|f_1, m_3; f_2, m_4\rangle. \tag{A.5}$$

Performing the summation over F and m_F, the above equation becomes

$$\sum_{F=0,2}^{2F} \lambda_F \hat{P}_F = \langle f_1, m_1; f_2, m_2 | \hat{\vec{f}_1} \cdot \hat{\vec{f}_2} | f_1, m_3; f_2, m_4 \rangle \tag{A.6}$$

$$= \hat{\vec{f}}_{m_3 m_2} \cdot \hat{\vec{f}}_{m_4 m_1} = (\hat{f}_\alpha)_{m_3 m_2} (\hat{f}_\alpha)_{m_4 m_1}$$

where $(\hat{f}_\alpha)_{m_3 m_2}$ are the matrix elements for the Cartesian traceless spin $f = 2$ Pauli matrices. This is one of the operator identities that we use in the calculation.

In the following we express the projection operator onto $|F = 0, m_F = 0\rangle$ state, i.e. $\hat{P}_{F=0} = |F = 0, m_F = 0\rangle\langle F = 0, m_F = 0|$. The state $|F = 0, m_F = 0\rangle$ for spin-$F = 2$ may be expressed interms of the five Zeeman sublevels as:

$$|F = 0, m_F = 0\rangle = \sum_{m_1, m_2} |m_1, m_2\rangle\langle m_1, m_2 | F = 0, m_F = 0\rangle \tag{A.7}$$

with $m_1 + m_2 = 0$. Using the Clebsch-Gordan coefficients, the above equation becomes

$$|F = 0, m_F = 0\rangle = \frac{1}{\sqrt{5}}\left(|2, -2\rangle - |1, -1\rangle + |0, 0\rangle - |-1, 1\rangle + |-2, 2\rangle\right) \tag{A.8}$$

Thus, the projection operator $\hat{P}_0$ takes the form

$$\hat{P}_0 = \frac{1}{5}\left(|2, -2\rangle - |1, -1\rangle + |0, 0\rangle - |-1, 1\rangle + |-2, 2\rangle\right)$$
$$\times \left(\langle 2, -2| - \langle 1, -1| + \langle 0, 0| - \langle -1, 1| + \langle -2, 2|\right), \tag{A.9}$$

which is employed particularly in Sec. 1.3.

Derivation of Linear regime Hamiltonian

In this appendix we discuss in detail the derivations of the linear regime Hamiltonian that employed in Chapters 1 and 5. In the following we consider a spin-2 (or spin-1) ^{87}Rb atoms, with Zeeman components $m = \pm 2, \pm 1, 0$ (or $m = \pm 1, 0$), confined in a dipole trap in the presence of an external magnetic field oriented along the z-axis. In the discussion of the short-range interactions Hamiltonian, we show how to calculate the coupling constants for the possible collisional channels in spin-2 and spin-1 systems.

- The second-quantized single-particle Hamiltonian of the system is given by

$$\hat{H}_0 = \sum_m \int d^3 r \, \hat{\psi}_m^\dagger(\vec{r}) \left[-\frac{\hbar^2}{2M}\Delta + V(\vec{r}) + E_z \right] \hat{\psi}_m(\vec{r}), \qquad (B.1)$$

where $\hat{\psi}_m(\vec{r})$ annihilates bosons with spin projection m. The first part is the kinetic energy, the second is the optical trap and the third part is the Zeeman energy, $E_z = (p + \nabla p \cdot \vec{r}) \, m + q m^2$, which contains the linear and quadratic Zeeman effects due to homogeneous magnetic field and the magnetic gradient effect (see Sec. 1.2.3).

- The second-quantized two-particle Hamiltonian that describes short-range interactions is expressible as

$$\hat{H}_{\mathrm{sr}} = \frac{1}{2} \int d^3 \vec{r} \sum_{\vec{m}} U_{\vec{m}} \hat{\psi}_{m_4}^\dagger(\vec{r}) \hat{\psi}_{m_3}^\dagger(\vec{r}) \hat{\psi}_{m_2}(\vec{r}) \hat{\psi}_{m_1}(\vec{r}), \qquad (B.2)$$

where

$$U_{\vec{m}} = \sum_F \sum_{M=-F}^F g_F \langle m_1, m_2 | F, M \rangle \langle F, M | m_3, m_4 \rangle \qquad (B.3)$$

are the coupling constants for the collisional channels $\{m_1, m_2\} \rightarrow \{m_3, m_4\}$ ($\vec{m} \equiv (m_1, m_2, m_3, m_4)$), where $\langle m_1, m_2 | F, M \rangle$ are the Clebsch-Gordan coefficients.

In the following we are interested in the first stage (linear regime) of the spinor dynamics of a spin-2 (or spin-1) BEC initially prepared in the $|0\rangle$ sublevel. Hence, the possible collisions, in this case, are:

Spin preserving collisions

$$
\begin{aligned}
\{0,0\} \to \{0,0\} \Longrightarrow U_{\substack{0,0 \\ 0,0}} &= g_0 \langle 0,0|0,0\rangle \langle 0,0|0,0\rangle^* + g_2 \langle 0,0|2,0\rangle \\
&\times \langle 0,0|2,0\rangle^* + g_4 \langle 0,0|4,0\rangle \langle 0,0|4,0\rangle^* \\
&= \tfrac{g_0}{5} + \tfrac{2g_2}{7} + \tfrac{18g_4}{35} = \tfrac{c_2}{5} + c_0 \\
\{0,1\} \to \{0,1\} \Longrightarrow U_{\substack{0,1 \\ 0,1}} &= g_2 \langle 0,1|2,1\rangle \langle 0,1|2,1\rangle^* \\
&+ g_4 \langle 0,1;4,1\rangle \langle 0,1|4,1\rangle^* \\
&= \tfrac{g_2}{14} + \tfrac{3g_4}{7} = \tfrac{c_0+3c_1}{2} \\
\{0,-1\} \to \{0,-1\} \Longrightarrow U_{\substack{0,-1 \\ 0,-1}} &= g_2 \langle 0,-1|2,-1\rangle \langle 0,-1|2,-1\rangle^* \\
&+ g_4 \langle 0,-1|4,-1\rangle \langle 0,-1|4,-1\rangle^* \\
&= \tfrac{g_2}{14} + \tfrac{3g_4}{7} = \tfrac{c_0+3c_1}{2} = U_{\substack{0,1 \\ 0,1}}
\end{aligned}
$$

Spin changing collisions

$$
\begin{aligned}
\{0,0\} \to \{1,-1\} \Longrightarrow U_{\substack{0,0 \\ 1,-1}} &= g_0 \langle 0,0|0,0\rangle \langle 1,-1|0,0\rangle^* + g_2 \langle 0,0|2,0\rangle \\
&\times \langle 1,-1|2,0\rangle^* + g_4 \langle 0,0|4,0\rangle \langle 1,-1|4,0\rangle^* \\
&= \tfrac{-g_0}{5} - \tfrac{g_2}{7} + \tfrac{12g_4}{35} = -\tfrac{c_2}{5} + 3c_1 \\
\{1,-1\} \to \{0,0\} \Longrightarrow U_{\substack{1,-1 \\ 0,0}} &= g_0 \langle 1,-1|0,0\rangle \langle 0,0|0,0\rangle^* + g_2 \langle 1,-1|2,0\rangle \\
&\times \langle 0,0|2,0\rangle^* + g_4 \langle 1,-1|4,0\rangle \langle 0,0|4,0\rangle^* \\
&= \tfrac{-g_0}{5} - \tfrac{g_2}{7} + \tfrac{12g_4}{35} = -\tfrac{c_2}{5} + 3c_1 = U_{\substack{0,0 \\ 1,-1}}
\end{aligned}
$$

We use similar ways to calculate the coupling strength coeffiecents for all possible collisions in spin-2 system, which are tabulated in Table 1.3.

Following the same way, the coupling constants for spin-1 are:

$$
\begin{aligned}
U_{\substack{0,0 \\ 0,0}} &= \tfrac{g_0+2g_2}{3} \\
U_{\substack{0,1 \\ 0,1}} = U_{\substack{0,-1 \\ 0,-1}} &= \tfrac{g_2}{2} \\
U_{\substack{0,0 \\ 1,-1}} = U_{\substack{1,-1 \\ 0,0}} &= \tfrac{-g_0+g_2}{3}
\end{aligned}
$$

Using the above coupling strength coeffiecients, the short-range interaction part of the Hamiltonian in the linear regime takes the form

$$
\begin{aligned}
\hat{H}_{\mathrm{sr}}^{\mathrm{lr}} = \frac{1}{2} \int d^3\vec{r} \Big\{ &U_{\substack{0,0 \\ 0,0}} \hat{\psi}_0^\dagger(\vec{r})\hat{\psi}_0^\dagger(\vec{r})\hat{\psi}_0(\vec{r})\hat{\psi}_0(\vec{r}) \\
&+ 4U_{\substack{0,1 \\ 0,1}} \big[\hat{\psi}_0^\dagger(\vec{r})\hat{\psi}_1^\dagger(\vec{r})\hat{\psi}_0(\vec{r})\hat{\psi}_1(\vec{r}) + \hat{\psi}_0^\dagger(\vec{r})\hat{\psi}_{-1}^\dagger(\vec{r})\hat{\psi}_0(\vec{r})\hat{\psi}_{-1}(\vec{r}) \big] \\
&+ 2U_{\substack{0,0 \\ 1,-1}} \big[\hat{\psi}_0^\dagger(\vec{r})\hat{\psi}_0^\dagger(\vec{r})\hat{\psi}_1(\vec{r})\hat{\psi}_{-1}(\vec{r}) + \hat{\psi}_1^\dagger(\vec{r})\hat{\psi}_{-1}^\dagger(\vec{r})\hat{\psi}_0(\vec{r})\hat{\psi}_0(\vec{r}) \big] \Big\}.
\end{aligned}
$$
$$\tag{B.4}$$

The free energy of the spinor system is described by $\hat{K} = \hat{H}_0 + \hat{H}_{\mathrm{sr}} - \mu\hat{N}$, where $\hat{N} = \sum_m \int d^3r\, \hat{\psi}_m^\dagger(\vec{r})\hat{\psi}_m(\vec{r})$ is the total number operator of the system.

Thus, this free energy in the linear regime becomes

$$
\hat{K} = \int d^3\vec{r} \Bigg\{ \psi_0^\dagger(\vec{r}) \left[-\frac{\hbar^2}{2M}\Delta + V(\vec{r}) - \mu \right] \hat{\psi}_0(\vec{r})
$$
$$
+ \sum_{m=\pm 1} \psi_m^\dagger(\vec{r}) \left[\frac{\hbar^2}{2M}\Delta + V(\vec{r}) + m\nabla p \cdot \vec{r} + q - \mu \right] \hat{\psi}_m(\vec{r})
$$
$$
+ \frac{U_{0,0}^{0,0}}{2} \hat{\psi}_0^\dagger(\vec{r})\hat{\psi}_0^\dagger(\vec{r})\hat{\psi}_0(\vec{r})\hat{\psi}_0(\vec{r})
$$
$$
+ 2U_{0,1}^{0,1} \left[\hat{\psi}_0^\dagger(\vec{r})\hat{\psi}_1^\dagger(\vec{r})\hat{\psi}_0(\vec{r})\hat{\psi}_1(\vec{r}) + \hat{\psi}_0^\dagger(\vec{r})\hat{\psi}_{-1}^\dagger(\vec{r})\hat{\psi}_0(\vec{r})\hat{\psi}_{-1}(\vec{r}) \right]
$$
$$
+ U_{1,-1}^{0,0} \left[\hat{\psi}_0^\dagger(\vec{r})\hat{\psi}_0^\dagger(\vec{r})\hat{\psi}_1(\vec{r})\hat{\psi}_{-1}(\vec{r}) + \hat{\psi}_1^\dagger(\vec{r})\hat{\psi}_{-1}^\dagger(\vec{r})\hat{\psi}_0(\vec{r})\hat{\psi}_0(\vec{r}) \right] \Bigg\}.
$$

(B.5)

As it was mentioned in chapter 2, this first stages of the spinor dynamics (linear regime) may be described by means of a Bogoliubov approximation (see Ch. 5 for spin-1):

$$
[\hat{\psi}_2(\vec{r},t), \hat{\psi}_1(\vec{r},t), \hat{\psi}_0(\vec{r},t), \hat{\psi}_{-1}(\vec{r},t), \hat{\psi}_{-2}(\vec{r},t)]^T = \left[(\boldsymbol{\Psi}_0(\vec{r}) + \delta\hat{\boldsymbol{\Psi}}(\vec{r},t))^T \right] e^{-i\mu t}.
$$

(B.6)

where $\delta\hat{\boldsymbol{\Psi}}(\vec{r},t)^T = (\delta\hat{\psi}_2(\vec{r},t), \delta\hat{\psi}_1(\vec{r},t), \delta\hat{\psi}_0(\vec{r},t), \delta\hat{\psi}_{-1}(\vec{r},t), \delta\hat{\psi}_{-2}(\vec{r},t))^T$ are small fluctuations of the spinor field operator and $\boldsymbol{\Psi}_0(\vec{r})^T = (0, 0, \psi_0(\vec{r}), 0, 0)^T$ is the initial state of the condensate with $\psi_0(\vec{r})$ and μ obtained by solving the time-independent Gross-Pitaevskii equation Eq. (2.1).

Inserting Eq. (B.6) into Eq. (B.5), we obtain

$$
\hat{K} = \int d^3\vec{r} \Bigg\{ (\delta\psi_0^\dagger(\vec{r}) + \psi_0^*(\vec{r})) \left[-\frac{\hbar^2}{2M}\Delta + V(\vec{r}) - \mu \right] (\delta\hat{\psi}_0(\vec{r}) + \psi_0(\vec{r}))
$$
$$
+ \sum_{m=\pm 1} \delta\psi_m^\dagger(\vec{r}) \left[\frac{\hbar^2}{2M}\Delta + V(\vec{r}) + m\nabla p \cdot \vec{r} + q - \mu \right] \delta\hat{\psi}_m(\vec{r})
$$
$$
+ \frac{U_{0,0}^{0,0}}{2}(\delta\hat{\psi}_0^\dagger(\vec{r}) + \psi_0^*(\vec{r}))(\delta\hat{\psi}_0^\dagger(\vec{r}) + \psi_0^*(\vec{r}))(\delta\hat{\psi}_0(\vec{r}) + \psi_0(\vec{r}))(\delta\hat{\psi}_0(\vec{r}) + \psi_0(\vec{r}))
$$
$$
+ 4U_{0,1}^{0,1} \left[(\delta\hat{\psi}_0^\dagger(\vec{r}) + \psi_0^*(\vec{r}))\delta\hat{\psi}_1^\dagger(\vec{r})(\delta\hat{\psi}_0(\vec{r}) + \psi_0(\vec{r}))\delta\hat{\psi}_1(\vec{r}) \right.
$$
$$
\left. + (\delta\hat{\psi}_0^\dagger(\vec{r}) + \psi_0^*(\vec{r}))\delta\hat{\psi}_{-1}^\dagger(\vec{r})(\delta\hat{\psi}_0(\vec{r}) + \psi_0(\vec{r}))\delta\hat{\psi}_{-1}(\vec{r}) \right]
$$
$$
+ 2U_{1,-1}^{0,0} \left[(\delta\hat{\psi}_0^\dagger(\vec{r}) + \psi_0^*(\vec{r}))(\delta\hat{\psi}_0^\dagger(\vec{r}) + \psi_0(\vec{r}))\delta\hat{\psi}_1(\vec{r})\delta\hat{\psi}_{-1}(\vec{r}) \right.
$$
$$
\left. + \delta\hat{\psi}_1^\dagger(\vec{r})\delta\hat{\psi}_{-1}^\dagger(\vec{r})(\delta\hat{\psi}_0(\vec{r}) + \psi_0(\vec{r}))(\delta\hat{\psi}_0(\vec{r}) + \psi_0(\vec{r})) \right] \Bigg\}.
$$

(B.7)

Keeping terms up to second order in $\delta\hat{\psi}_m(\vec{r})$, the above equation reduces to:

$$
\hat{K} = \int d^3\vec{r} \Bigg\{ \psi_0^*(\vec{r})(-\frac{\hbar^2}{2M}\nabla^2 + V(\vec{r}) + \frac{U_{0,0}^{0,0}}{2}\psi_0^2(\vec{r}) - \mu)\psi_0(\vec{r})
$$

$$
+ \delta\hat{\psi}_0^\dagger(\vec{r})(-\frac{\hbar^2}{2M}\nabla^2 + V(\vec{r}) + U_{0,0}\psi_0^2(\vec{r}) - \mu)\delta\hat{\psi}_0(\vec{r})
$$

$$
+ \frac{U_{0,0}^{0,0}}{2}\psi_0^2(\vec{r})(\delta\hat{\psi}_0^\dagger(\vec{r})\delta\hat{\psi}_0^\dagger(\vec{r}) + \delta\hat{\psi}_0(\vec{r})\delta\hat{\psi}_0(\vec{r}))
$$

$$
+ \psi_0^*(\vec{r})(-\frac{\hbar^2}{2M}\nabla^2 + V(\vec{r}) + U_{0,0}\psi_0^2(\vec{r}) - \mu)\delta\hat{\psi}_0(\vec{r})
$$

$$
+ \delta\hat{\psi}_0^\dagger(\vec{r})(-\frac{\hbar^2}{2M}\nabla^2 + V(\vec{r}) + U_{0,0}\psi_0^2(\vec{r}) - \mu)\psi_0(\vec{r})
$$

$$
+ \sum_{m=\pm 1} \delta\hat{\psi}_m^\dagger(\vec{r})(-\frac{\hbar^2}{2M}\nabla^2 + V(\vec{r}) + 2U_{01}^{0,1}\psi_0^2(\vec{r}) + m\nabla p \cdot \vec{r} + q - \mu)\delta\hat{\psi}_m(\vec{r})
$$

$$
+ U_{0,0}^{1,-1}\psi_0^2(\vec{r})(\delta\hat{\psi}_{-1}^\dagger(\vec{r})\delta\hat{\psi}_1^\dagger(\vec{r}) + \delta\hat{\psi}_1(\vec{r})\delta\hat{\psi}_{-1}(\vec{r})) \Bigg\}. \tag{B.8}
$$

In the above equation, as it was discussed in Ch. 2, the fourth and the fifth terms vanish due to the time-independent GPE (2.1). The first term is the free energy of the initial BEC, which is constant. The second and third terms describe the dynamics of the density and phase fluctuations $\delta\hat{\psi}_0(\vec{r})$ of the $|0\rangle$ BEC. Note that these fluctuations are decoupled from the spin fluctuations $\delta\hat{\psi}_{\pm 1}(\vec{r})$ in the linear regime. The two last terms govern the dynamics of the spin fluctuations in $|\pm 1\rangle$, which clearly describes pair creation into $|\pm 1\rangle$.

Therefore, the effective Hamiltonian that describes pair creation of atoms into $|\pm 1\rangle$ Zeeman sublevels acquires the form:

$$
\hat{H}_{\pm 1} = \int d^3\vec{r} \Bigg\{ \sum_{m=\pm 1} \delta\hat{\psi}_m^\dagger(\vec{r})\left[\hat{H}_{eff}(\vec{r}) + m\nabla p \cdot \vec{r} + q\right]\delta\hat{\psi}_m(\vec{r})
$$
$$
+ U_{1-1}n_0(\vec{r})\left[\delta\hat{\psi}_{-1}^\dagger(\vec{r})\delta\hat{\psi}_1^\dagger(\vec{r}) + \delta\hat{\psi}_1(\vec{r})\delta\hat{\psi}_{-1}(\vec{r})\right] \Bigg\} \tag{B.9}
$$

with

$$
\hat{H}_{eff}(\vec{r}) = -\frac{\hbar^2}{2M}\nabla^2 + V_{eff}(\vec{r}) \tag{B.10}
$$

where $V_{eff}(\vec{r}) = V(\vec{r}) + 2U_{01}n_0(\vec{r}) - \mu$ and $n_0(\vec{r}) = \psi_0^2(\vec{r})$. Note that for the sake of simplicity we use U_{00} for U_{00}^{00} and U_{1-1} for U_{00}^{1-1} in the thesis and it is also clrear that $2U_{01} = U_{00}^{00} + U_{00}^{1-1}$. The last term of the above equation originates from spin-changing collisions process, which convert atoms in the $|0\rangle$ BEC into pairs of atoms in $|\pm 1\rangle$ and vice-versa, resembles parametric down conversion in optical parametric amplifiers.

• The second-quantized magnetic dipole-dipole interactions is given by

$$\hat{H}_{\mathrm{dd}} = \sum_{\vec{m}} \int \ d^3r \, d^3r' \, \hat{\psi}_{m_1}^\dagger(\vec{r}) \hat{\psi}_{m_2}^\dagger(\vec{r}') U_{m_1,m_2}^{\mathrm{dd}}(\vec{r},\vec{r}') \hat{\psi}_{m_4}(\vec{r}') \hat{\psi}_{m_3}(\vec{r}), \ \text{(B.11)}$$

where

$$U_{\substack{m_1,m_2 \\ m_3,m_4}}^{\mathrm{dd}}(\vec{r},\vec{r}') = \frac{c_{dd}}{2|\vec{r}-\vec{r}'|^3} \times \left[\hat{\vec{F}}_{m_1 m_3} \cdot \hat{\vec{F}}_{m_2 m_4} - 3 \left(\hat{\vec{F}}_{m_1 m_3} \cdot \vec{u}_r \right) \left(\hat{\vec{F}}_{m_2 m_4} \cdot \vec{u}_r \right) \right],$$
(B.12)

are the effective DDI coupling strength coeffiecents and $\vec{u}_r = \frac{\vec{r}-\vec{r}'}{|\vec{r}-\vec{r}'|}$ is the unit vector along the relative interparticle distance.

In the following we follow a similar approach as in the short-range interaction part, i.e. we calculate the effective DDI coupling strength coefficients for the first stage of the dynamics (linear regime):

Spin preserving collisions
for the collisions of $\{0,1\} \to \{1,0\}$:

$$U_{\substack{0,1 \\ 1,0}}^{\mathrm{dd}}(\vec{r},\vec{r}') = \frac{c_{dd}}{2|\vec{r}-\vec{r}'|^3} \times \left[\hat{\vec{F}}_{01} \cdot \hat{\vec{F}}_{10} - 3 \left(\hat{\vec{F}}_{01} \cdot \vec{u}_r \right) \left(\hat{\vec{F}}_{10} \cdot \vec{u}_r \right) \right]. \qquad \text{(B.13)}$$

Using $\hat{\vec{F}}_{m_1 m_2} = ((\hat{F}_x)_{m_1 m_2}, (\hat{F}_y)_{m_1 m_2}, (\hat{F}_z)_{m_1 m_2})$ and the matrix elements for the Cartesian traceless spin-$F = 2$ and spin-$F = 1$ Pauli matrices, one can easily see that

$\hat{\vec{F}}_{m_1 m_2}$	spin-2	spin-1
$\hat{\vec{F}}_{10} = \hat{\vec{F}}_{0-1}$	$(\frac{\sqrt{6}}{2}, -i\frac{\sqrt{6}}{2}, 0)$	$(\frac{\sqrt{2}}{2}, -i\frac{\sqrt{2}}{2}, 0)$
$\hat{\vec{F}}_{01} = \hat{\vec{F}}_{-10}$	$(\frac{\sqrt{6}}{2}, i\frac{\sqrt{6}}{2}, 0)$	$(\frac{\sqrt{2}}{2}, i\frac{\sqrt{2}}{2}, 0)$
$\hat{\vec{F}}_{00}$	$(0, 0, 0)$	$(0, 0, 0)$

Thus, employing the values of $\hat{\vec{F}}_{10}$ and $\hat{\vec{F}}_{01}$ for spin-2 into Eq. (B.13), we get

$$\begin{aligned} U_{\substack{0,1 \\ 1,0}}^{\mathrm{dd}}(\vec{r},\vec{r}') &= \frac{c_{dd}}{2|\vec{r}-\vec{r}'|^3} \times \left[\frac{12}{4} - \frac{18}{4} \left(\frac{(x-x')^2 + (y-y')^2}{|\vec{r}-\vec{r}'|^2} \right) \right] \\ &= \frac{-3c_{dd}\left(1 - 3\cos^2\theta_{rr'}\right)}{4|\vec{r}-\vec{r}'|^3} \end{aligned}$$
(B.14)

where $\cos\theta_{rr'} = \frac{(z-z')}{|r-r'|}$.

Thus, for spin-2, following the same procedure, one obtains

- $\{0, -1\} \rightarrow \{-1, 0\}$: $U^{\mathrm{dd}}_{\substack{0,-1 \\ -1,0}}(\vec{r}, \vec{r}') = \frac{-3c_{dd}\left(1 - 3\cos^2\theta_{rr'}\right)}{4|\vec{r} - \vec{r}'|^3}$

- $\{0, 0\} \rightarrow \{0, 0\}$: $U^{\mathrm{dd}}_{\substack{0,0 \\ 0,0}}(\vec{r}, \vec{r}') = 0$ since $\hat{\vec{F}}_{00} = (0, 0, 0)$.

Spin changing collisions

for the collision $\{0, 0\} \rightarrow \{1, -1\}$, we have

$$U^{\mathrm{dd}}_{\substack{0,0 \\ 1,-1}}(\vec{r}, \vec{r}') = \frac{c_{dd}}{2|\vec{r} - \vec{r}'|^3} \times \left[\hat{\vec{F}}_{01} \cdot \hat{\vec{F}}_{0-1} - 3\left(\hat{\vec{F}}_{01} \cdot \vec{u}_r\right)\left(\hat{\vec{F}}_{0-1} \cdot \vec{u}_r\right)\right]. \quad (\text{B.15})$$

Using the values of $\hat{\vec{F}}_{01}$ and $\hat{\vec{F}}_{0-1}$ for spin-2 in the above equation, we get

- $\{0, 0\} \rightarrow \{1, -1\}$: $U^{\mathrm{dd}}_{\substack{0,0 \\ 1,-1}}(\vec{r}, \vec{r}') = \frac{-3c_{dd}\left(1 - 3\cos^2\theta_{rr'}\right)}{4|\vec{r} - \vec{r}'|^3}$

- $\{1, -1\} \rightarrow \{0, 0\}$: $U^{\mathrm{dd}}_{\substack{1,-1 \\ 0,0}}(\vec{r}, \vec{r}') = \frac{-3c_{dd}\left(1 - 3\cos^2\theta_{rr'}\right)}{4|\vec{r} - \vec{r}'|^3}$

For spin-1 system, the above effective DDI coupling becomes

$$U^{\mathrm{dd}}_{\substack{0,1 \\ 1,0}}(\vec{r}, \vec{r}') = U^{\mathrm{dd}}_{\substack{0,-1 \\ -1,0}}(\vec{r}, \vec{r}') = U^{\mathrm{dd}}_{\substack{0,0 \\ 1,-1}}(\vec{r}, \vec{r}') = \frac{-c_{dd}\left(1 - 3\cos^2\theta_{rr'}\right)}{4|\vec{r} - \vec{r}'|^3}$$

Using these effective DDI coupling strengths, the linear regime part of the DDI Hamiltonian becomes

$$\hat{H}^{\mathrm{lr}}_{dd} = \int d^3r \, d^3r' \frac{-\alpha c_{dd}\left(1 - 3\cos^2\theta_{rr'}\right)}{2|\vec{r} - \vec{r}'|^3} \left\{\hat{\psi}^\dagger_1(\vec{r})\hat{\psi}^\dagger_{-1}(\vec{r}')\hat{\psi}_0(\vec{r})\hat{\psi}_0(\vec{r}')\right.$$

$$+ \hat{\psi}^\dagger_0(\vec{r})\hat{\psi}^\dagger_{-1}(\vec{r}')\hat{\psi}_{-1}(\vec{r})\hat{\psi}_0(\vec{r}') \quad (\text{B.16})$$

$$\left. + \hat{\psi}^\dagger_0(\vec{r})\hat{\psi}^\dagger_1(\vec{r}')\hat{\psi}_1(\vec{r})\psi_0(\vec{r}')\right\}$$

with $\alpha = 3$ and 1 for spin-2 and spin-1 respectively.

Upon inserting Eq. (B.6) into Eq. (B.16) and keeping terms up to second order in $\delta\hat{\psi}_m(\vec{r})$, the Hamiltonian of the DDI in the linear regime takes the form

$$\hat{H}^{\mathrm{lr}}_{dd} = \int d^3r \, d^3r' \psi_0(\vec{r})\psi_0(\vec{r}')V_{\mathrm{dd}}(\vec{r} - \vec{r}')$$

$$\times \left[\delta\hat{\psi}^\dagger_1(\vec{r})\delta\hat{\psi}_1(\vec{r}') + \delta\hat{\psi}^\dagger_{-1}(\vec{r})\delta\hat{\psi}_{-1}(\vec{r}')\right.$$

$$\left. + \delta\hat{\psi}^\dagger_1(\vec{r})\delta\hat{\psi}^\dagger_{-1}(\vec{r}') + \delta\hat{\psi}_1(\vec{r})\delta\hat{\psi}_{-1}(\vec{r}')\right] \quad (\text{B.17})$$

with $V_{\mathrm{dd}}(\vec{r} - \vec{r}') = \frac{\alpha c_{dd}}{2|\vec{r} - \vec{r}'|^3}\left(3\cos^2\theta_{rr'} - 1\right)$. The last term is similar to the last term in Eq. (B.9), and hence the DDI regularises the spin changing process, which resembles parametric amplification process, i.e. depending on its sign either it will enhance or reduce the amplification process.

Bibliography

[1] S. Chu, L. Hollberg, J. E. Bjorkholm, A. Cable and A. Ashkin, *Three-dimensional viscous confinement and cooling of atoms by resonance radiation pressure*, Phys. Rev. Lett. **55**, 48 (1985).

[2] E. L. Raab, M. Prentiss, A. Cable, S. Chu and D. E. Pritchard, *Trapping of Neutral Sodium Atoms with Radiation Pressure*, Phys. Rev. Lett. **59**, 2631 (1987).

[3] M. Greiner, O. Mandel, T. Esslinger, T. Hänsch and I. Bloch, *Quantum phase transition from a superfluid to a Mott insulator in a gas of ultracold atoms*, Nature **415**, 39 (2002).

[4] T. Stöferle, H. Moritz, C. Schori, M. Köhl and T. Esslinger, *Transition from a Strongly Interacting 1D Superfluid to a Mott Insulator*, Phys. Rev. Lett. **92**, 130403 (2004).

[5] B. Paredes, A. Widera, V. Murg, O. Mandel, S. Fölling, I. Cirac, G. V. Shlyapnikov, T. W. Hänsch and I. Bloch, *Tonks-Girardeau gas of ultracold atoms in an optical lattice*, Nature **429**, 277 (2004).

[6] T. Kinoshita, T. Wenger and D. S. Weiss, *Observation of a One-Dimensional Tonks-Girardeau Gas*, Science **305**, 1125 (2004).

[7] K. E. Strecker, G. B. Partridge, A. G. Truscott and R. G. Hulet, *Formation and propagation of matter-wave soliton trains*, Nature **417**, 150 (2002).

[8] L. Khaykovich, F. Schreck, G. Ferrari, T. Bourdel, J. Cubizolles, L. D. Carr, Y. Castin and C. Salomon, *Formation of a Matter-Wave Bright Soliton*, Science **296**, 1290 (2002).

[9] S. Burger, K. Bongs, S. Dettmer, W. Ertmer, K. Sengstock, A. Sanpera, G. V. Shlyapnikov and M. Lewenstein, *Dark Solitons in Bose-Einstein Condensates*, Phys. Rev. Lett. **83**, 5198 (1999).

[10] J. Denschlag, J. E. Simsarian, D. L. Feder, C. W. Clark, L. A. Collins, J. Cubizolles, L. Deng, E. W. Hagley, K. Helmerson, W. P. Reinhardt, S. L. Rolston, B. I. Schneider and W. D. Phillips, *Generating Solitons by Phase Engineering of a Bose-Einstein Condensate*, Science **287**, 97 (2000).

[11] B. Eiermann, T. Anker, M. Albiez, M. Taglieber, P. Treutlein, K.-P. Marzlin and M. K. Oberthaler, *Bright Bose-Einstein Gap Solitons of Atoms with Repulsive Interaction*, Phys. Rev. Lett. **92**, 230401 (2004).

[12] P. R. Berman, *Atom Interferometry*, Academic Press (1997).

[13] D. S. Weiss, B. C. Young and S. Chu, *Precision measurement of the photon recoil of an atom using atomic interferometry*, Phys. Rev. Lett. **70**, 2706 (1993).

[14] A. Peters, K. Y. Chung and S. Chu, *Measurement of Gravitational Acceleration by Dropping Atoms*, Nature **400**, 849 (1999).

[15] G. Lamporesi, A. Bertoldi, L. Cacciapuoti, M. Prevedelli and G. M. Tino, *Determination of the Newtonian Gravitational Constant Using Atom Interferometry*, Phys. Rev. Lett. **100**, 050801 (2008).

[16] T. L. Gustavson, A. Landragin and M. A. Kasevich, *Rotation Sensing with a Dual Atom-interferometer Sagnac Gyroscope*, Class. Quantum Grav. **17**, 2385 (2000).

[17] H. Müller, S.-w. Chiow, S. Herrmann, S. Chu and K.-Y. Chung, *Atom-Interferometry Tests of the Isotropy of Post-Newtonian Gravity*, Phys. Rev. Lett. **100**, 031101 (2008).

[18] C. J. Myatt, E. A. Burt, R. W. Ghrist, E. A. Cornell and C. E. Wieman, *Production of Two Overlapping Bose-Einstein Condensates by Sympathetic Cooling*, Phys. Rev. Lett. **78**, 586 (1997).

[19] D. M. Stamper-Kurn, M. R. Andrews, A. P. Chikkatur, S. Inouye, H.-J. Miesner, J. Stenger and W. Ketterle, *Optical Confinement of a Bose-Einstein Condensate*, Phys. Rev. Lett. **80**, 2027 (1998).

[20] M.-S. Chang, C. D. Hamley, M. D. Barrett, J. A. Sauer, K. M. Fortier, W. Zhang, L. You and M. S. Chapman, *Observation of Spinor Dynamics in Optically Trapped ^{87}Rb Bose-Einstein Condensates*, Phys. Rev. Lett. **92**, 140403 (2004).

[21] H. Schmaljohann, M. Erhard, J. Kronjäger, M. Kottke, S. van Staa, L. Cacciapuoti, J. J. Arlt, K. Bongs and K. Sengstock, *Dynamics of $F = 2$ Spinor Bose-Einstein Condensates*, Phys. Rev. Lett. **92**, 040402 (2004).

[22] N. N. Klausen, J. L. Bohn and C. H. Greene, *Nature of spinor Bose-Einstein condensates in rubidium*, Phys. Rev. A **64**, 053602 (2001).

[23] T.-L. Ho, *Spinor Bose Condensates in Optical Traps*, Phys. Rev. Lett. **81**, 742 (1998).

[24] C. V. Ciobanu, S.-K. Yip and T.-L. Ho, *Phase diagrams of F = 2 spinor Bose-Einstein condensates*, Phys. Rev. A **61**, 033607 (2000).

[25] A. Griesmaier, J. Werner, S. Hensler, J. Stuhler and T. Pfau, *Bose-Einstein Condensation of Chromium*, Phys. Rev. Lett. **94**, 160401 (2005).

[26] T. Ohmi and K. Machida, *Bose-Einstein condensation with internal degrees of freedom in alkali atom gases*, Journal of the Physical Society of Japan **67**, 1822 (1998).

[27] M. Koashi and M. Ueda, *Exact Eigenstates and Magnetic Response of Spin-1 and Spin-2 Bose-Einstein Condensates*, Phys. Rev. Lett. **84**, 1066 (2000).

[28] W. X. Zhang, S. Yi and L. You, *Mean field ground state of a spin-1 condensate in a magnetic field*, New Journal of Physics **5**, 77 (2003).

[29] C. K. Law, H. Pu and N. P. Bigelow, *Quantum Spins Mixing in Spinor Bose-Einstein Condensates*, Phys. Rev. Lett. **81**, 5257 (1998).

[30] E. V. Goldstein and P. Meystre, *Quantum theory of atomic four-wave mixing in Bose-Einstein condensates*, Phys. Rev. A **59**, 3896 (1999).

[31] H. Pu, C. K. Law, S. Raghavan, J. H. Eberly and N. P. Bigelow, *Spin-mixing dynamics of a spinor Bose-Einstein condensate*, Phys. Rev. A **60**, 1463 (1999).

[32] J. P. Burke, P. S. Julienne, C. J. Williams, Y. B. Band and M. Trippenbach, *Four-wave mixing in Bose-Einstein condensate systems with multiple spin states*, Phys. Rev. A **70**, 033606 (2004).

[33] D. R. Romano and E. J. V. de Passos, *Population and phase dynamics of F = 1 spinor condensates in an external magnetic field*, Phys. Rev. A **70**, 043614 (2004).

[34] W. Zhang, D. L. Zhou, M.-S. Chang, M. S. Chapman and L. You, *Coherent spin mixing dynamics in a spin-1 atomic condensate*, Phys. Rev. A **72**, 013602 (2005).

[35] A. E. Leanhardt, Y. Shin, D. Kielpinski, D. E. Pritchard and W. Ketterle, *Coreless Vortex Formation in a Spinor Bose-Einstein Condensate*, Phys. Rev. Lett. **90**, 140403 (2003).

[36] T. Isoshima, K. Machida and T. Ohmi, *Spin-domain formation in spinor Bose-Einstein condensation*, Phys. Rev. A **60**, 4857 (1999).

[37] J. Stenger, S. Inouye, D. M. Stamper-Kurn, H.-J. Miesner, A. P. Chikkatur and W. Ketterle, *Spin domains in ground-state Bose-Einstein condensates*, Nature **396**, 345 (1998).

[38] L.-M. Duan, J. I. Cirac and P. Zoller, *Quantum entanglement in spinor Bose-Einstein condensates*, Phys. Rev. A **65**, 033619 (2002).

[39] H. Pu and P. Meystre, *Creating Macroscopic Atomic Einstein-Podolsky-Rosen States from Bose-Einstein Condensates*, Phys. Rev. Lett. **85**, 3987 (2000).

[40] A. Einstein, *Quantentheorie des einatomigen idealen Gases*, Sitzber. Kgl. Preuss. Akad. Wiss. **1**, 3 (1925).

[41] S. N. Bose, *Plancks Gesetz und Lichtquantenhypothese*, Z. Phys **26**, 178 (1924).

[42] K. Huang, *Statistical Mechanics*, Wiley. New York p. 2nd edition (1987).

[43] M. H. Anderson, J. R. Ensher, M. R. Matthews, C. E. Wieman and E. A. Cornell, *Observation of Bose-Einstein Condensation in a Dilute Atomic Vapor*, Science **269**, 198 (1995).

[44] K. B. Davis, M. O. Mewes, M. R. Andrews, N. J. van Druten, D. S. Durfee, D. M. Kurn and W. Ketterle, *Bose-Einstein Condensation in a Gas of Sodium Atoms*, Phys. Rev. Lett. **75**, 3969 (1995).

[45] C. C. Bradley, C. A. Sackett, J. J. Tollett and R. G. Hulet, *Evidence of Bose-Einstein Condensation in an Atomic Gas with Attractive Interactions*, Phys. Rev. Lett. **75**, 1687 (1995).

[46] D. G. Fried, T. C. Killian, L. Willmann, D. Landhuis, S. C. Moss, D. Kleppner and T. J. Greytak, *Bose-Einstein Condensation of Atomic Hydrogen*, Phys. Rev. Lett. **81**, 3811 (1998).

[47] S. L. Cornish, N. R. Claussen, J. L. Roberts, E. A. Cornell and C. E. Wieman, *Stable ^{85}Rb Bose-Einstein Condensates with Widely Tunable Interactions*, Phys. Rev. Lett. **85**, 1795 (2000).

[48] G. Modugno, G. Ferrari, G. Roati, R. J. Brecha, A. Simoni and M. Inguscio, *Bose-Einstein Condensation of Potassium Atoms by Sympathetic Cooling*, Science **294**, 1320 (2001).

[49] T. Weber, J. Herbig, M. Mark, H.-C. Nagerl and R. Grimm, *Bose-Einstein Condensation of Cesium*, Science **299**, 232 (2003).

[50] Q. Beaufils, R. Chicireanu, T. Zanon, B. Laburthe-Tolra, E. Maréchal, L. Vernac, J.-C. Keller and O. Gorceix, *All-optical production of chromium Bose-Einstein condensates*, Phys. Rev. A **77**, 061601 (2008).

[51] S. Kraft, F. Vogt, O. Appel, F. Riehle and U. Sterr, *Bose-Einstein Condensation of Alkaline Earth Atoms:* ^{40}Ca, Phys. Rev. Lett. **103**, 130401 (2009).

[52] S. Stellmer, M. K. Tey, B. Huang, R. Grimm and F. Schreck, *Bose-Einstein Condensation of Strontium*, Phys. Rev. Lett. **103**, 200401 (2009).

[53] Y. Takasu, K. Maki, K. Komori, T. Takano, K. Honda, M. Kumakura, T. Yabuzaki and Y. Takahashi, *Spin-Singlet Bose-Einstein Condensation of Two-Electron Atoms*, Phys. Rev. Lett. **91**, 040404 (2003).

[54] R. Wynar, R. S. Freeland, D. J. Han, C. Ryu and D. J. Heinzen, *Molecules in a Bose-Einstein Condensate*, Science **287**, 1016 (2000).

[55] C. A. Regal, C. Ticknor, J. L. Bohn and D. S. Jin., *Creation of ultracold molecules from a Fermi gas of atoms*, Nature **424**, 47 (2003).

[56] J. Herbig, T. Kraemer, M. Mark, T. Weber, C. Chin, H.-C. Nagerl and R. Grimm, *Preparation of a Pure Molecular Quantum Gas*, Science **301**, 1510 (2003).

[57] J. Cubizolles, T. Bourdel, S. J. J. M. F. Kokkelmans, G. V. Shlyapnikov and C. Salomon, *Production of Long-Lived Ultracold Li_2 Molecules from a Fermi Gas*, Phys. Rev. Lett. **91**, 240401 (2003).

[58] S. Jochim, M. Bartenstein, A. Altmeyer, G. Hendl, S. Riedl, C. Chin, J. Hecker Denschlag and R. Grimm, *Bose-Einstein Condensation of Molecules*, Science **302**, 2101 (2003).

[59] K. Xu, T. Mukaiyama, J. R. Abo-Shaeer, J. K. Chin, D. E. Miller and W. Ketterle, *Formation of Quantum-Degenerate Sodium Molecules*, Phys. Rev. Lett. **91**, 210402 (2003).

[60] L. V. Butov, C. W. Lai, A. L. Ivanov, A. C. Gossard and D. S. Chemla, *Towards Bose-Einstein Condensation of Excitons in Potential Traps*, Nature **417**, 47 (2002).

[61] H. Deng, G. Welhs, C. Santori, J. Bloch and Y. Yamamoto, *Condensation of Semiconductor Microcavity Exciton Polaritons*, Science **298**, 199 (2002).

[62] J. Kasprzak, M. Richard, S. Kundermann, A. Baas, P. Jeambrun, J. M. J. Keeling, F. M. Marchetti, M. H. Szymańska, R. André, J. L. Staehli, V. Savona, P. B. Littlewood, B. Deveaud and L. S. Dang, *Bose-Einstein Condensation of Exciton Polaritons*, Nature **443**, 409 (2006).

[63] S. O. Demokritov, V. E. Demidov, O. Dzyapko, G. A. Melkov, A. A. Serga, B. Hillebrands and A. N. Slavin, *Bose-Einstein Condensation of Quasi-equilibrium Magnons at Room Temperature Under Pumping*, Nature **443**, 430 (2006).

[64] O. Penrose and L. Onsager, *Bose-Einstein Condensation and Liquid Helium*, Phys. Rev. **104**, 576 (1956).

[65] E. J. Mueller, T.-L. Ho, M. Ueda and G. Baym, *Fragmentation of Bose-Einstein condensates*, Phys. Rev. A **74**, 033612 (2006).

[66] P. W. Anderson, *Considerations on the Flow of Superfluid Helium*, Rev. Mod. Phys. **38**, 298 (1966).

[67] A. J. Leggett, *Bose-Einstein Condensation*, Cambridge University Press (1995).

[68] A. J. Leggett and F. Sols, *On the Concept of Spontaneously Broken Gauge Symmetry in Condensed Matter Physics*, Foundations of Physics **21** (1991).

[69] F. Dalfovo, S. Giorgini, L. P. Pitaevskii and S. Stringari, *Theory of Bose-Einstein condensation in trapped gases*, Rev. Mod. Phys. **71**, 463 (1999).

[70] J. L. Roberts, N. R. Claussen, S. L. Cornish and C. E. Wieman, *Magnetic Field Dependence of Ultracold Inelastic Collisions near a Feshbach Resonance*, Phys. Rev. Lett. **85**, 728 (2000).

[71] A. J. Moerdijk, B. J. Verhaar and A. Axelsson, *Resonances in ultracold collisions of ^6Li, ^7Li, and ^{23}Na*, Phys. Rev. A **51**, 4852 (1995).

[72] E. A. Donley, N. R. Claussen, S. L. Cornish, J. L. Roberts, E. A. Cornell and C. E. Wieman, *Dynamics of Collapsing and Exploding Bose-Einstein Condensates*, Nature **412**, 295 (2001).

[73] J. M. Gerton, D. Strekalov, I. Prodan and R. G. Hulet, *Direct Observation of Growth and Collapse of a Bose-Einstein Condensate with Attractive Interactions*, Nature **408**, 692 (2000).

[74] C. C. Bradley, C. A. Sackett and R. G. Hulet, *Bose-Einstein Condensation of Lithium: Observation of Limited Condensate Number*, Phys. Rev. Lett. **78**, 985 (1997).

[75] L. P. Pitaevskii, *Vortex Lines in an Imperfect Bose Gas*, Sov. Phys. JETP **13**, 451 (1961).

[76] E. P. Gross, *Structure of a Quantized Vortex in Boson Systems*, Nuovo Cimento **20**, 454 (1961).

[77] E. P. Gross, *Hydrodynamics of a Superfluid Condensate*, J. Math. Phys **4**, 195 (1963).

[78] N. N. Bogoliubov, *Theory of Superfluidity*, j. Phys (Moscow) **11**, 23 (1947).

[79] A. J. Leggett, *Bose-Einstein condensation in the alkali gases: Some fundamental concepts*, Rev. Mod. Phys. **73**, 307 (2001).

[80] C. J. Pethick and H. Smith, *Bose-Einstein Condensation in Dilute Gases*, Cambridge University Press (2002).

[81] L. P. Pitaevskii and S. Stringari, *Bose-Einstein Condensation*, Oxford University Press (2003).

[82] E. H. Lieb, R. Seiringer and J. Yngvason, *Bosons in a trap: A rigorous derivation of the Gross-Pitaevskii energy functional*, Phys. Rev. A **61**, 043602 (2000).

[83] C. Sulem and P. L. Sulem, *The Nonlinear Schrödinger Equation*, Springer-Verlag, New York (1999).

[84] A. L. Fetter and A. A. Svidzinsky, *Vortices in a trapped dilute Bose-Einstein condensate*, Journal of Physics: Condensed Matter **13**, R135 (2001).

[85] B. D. C. Cohen-Tannoudji and F. Laloë, *Quantum Mechanics*, John Wiley & Sons, New York (1997).

[86] F. Deuretzbacher, *Spinor Tonks-Girardeau gases and ultracold molecules*, Ph.D. thesis, Universität Hamburg (2008).

[87] F. Gerbier, A. Widera, S. Fölling, O. Mandel and I. Bloch, *Resonant control of spin dynamics in ultracold quantum gases by microwave dressing*, Phys. Rev. A **73**, 041602 (2006).

[88] L. Santos, M. Fattori, J. Stuhler and T. Pfau, *Spinor condensates with a laser-induced quadratic Zeeman effect*, Phys. Rev. A **75**, 053606 (2007).

[89] L. Santos and T. Pfau, *Spin-3 Chromium Bose-Einstein Condensates*, Phys. Rev. Lett. **96**, 190404 (2006).

[90] A. Lamacraft, *Quantum Quenches in a Spinor Condensate*, Phys. Rev. Lett. **98**, 160404 (2007).

[91] R. W. Cherng and E. Demler, *Magnetoroton Softening in Rb Spinor Condensates with Dipolar Interactions*, Phys. Rev. Lett. **103**, 185301 (2009).

[92] T. Kuwamoto, K. Araki, T. Eno and T. Hirano, *Magnetic field dependence of the dynamics of ^{87}Rb spin-2 Bose-Einstein condensates*, Phys. Rev. A **69**, 063604 (2004).

[93] S. R. Leslie, J. Guzman, M. Vengalattore, J. D. Sau, M. L. Cohen and D. M. Stamper-Kurn, *Amplification of fluctuations in a spinor Bose-Einstein condensate*, Phys. Rev. A **79**, 043631 (2009).

[94] P. Meystre and M. Sargent, *Elements of quantum optics*, Springer, Berlin, 4th edition (2007).

[95] J. Kronjäger, C. Becker, M. Brinkmann, R. Walser, P. Navez, K. Bongs and K. Sengstock, *Evolution of a spinor condensate: Coherent dynamics, dephasing, and revivals*, Phys. Rev. A **72**, 063619 (2005).

[96] J. Kronjäger, C. Becker, P. Navez, K. Bongs and K. Sengstock, *Magnetically Tuned Spin Dynamics Resonance*, Phys. Rev. Lett. **97**, 110404 (2006).

[97] A. T. Black, E. Gomez, L. D. Turner, S. Jung and P. D. Lett, *Spinor Dynamics in an Antiferromagnetic Spin-1 Condensate*, Phys. Rev. Lett. **99**, 070403 (2007).

[98] S. Tojo, T. Hayashi, T. Tanabe, T. Hirano, Y. Kawaguchi, H. Saito and M. Ueda, *Spin-dependent inelastic collisions in spin-2 Bose-Einstein condensates*, Phys. Rev. A **80**, 042704 (2009).

[99] J. Söding, D. Guéry-odelin, P. Desbiolles, F. Chevy, H. Inamori and J. Dalibard, *Three-body decay of a rubidium Bose-Einstein condensate*, Appl. Phys. B **69**, 257 (1999).

[100] O. Topič, *Resonante Spindynamik in Bose-Einstein-Kondensaten*, Ph.D. thesis, Gottfried Wilhelm Leibniz Universität Hannover (2010).

[101] L.-M. Duan, A. Sørensen, J. I. Cirac and P. Zoller, *Squeezing and Entanglement of Atomic Beams*, Phys. Rev. Lett. **85**, 3991 (2000).

[102] J. S. Bell, *On the Einstein-Podolsky-Rosen paradox*, Physics **1**, 195 (1964).

[103] A. Aspect, J. Dalibard and G. Roger, *Experimental Test of Bell's Inequalities Using Time- Varying Analyzers*, Phys. Rev. Lett. **49**, 1804 (1982).

[104] R. Movshovich, B. Yurke, P. G. Kaminsky, A. D. Smith, A. H. Silver, R. W. Simon and M. V. Schneider, *Observation of zero-point noise squeezing via a Josephson-parametric amplifier*, Phys. Rev. Lett. **65**, 1419 (1990).

[105] D. F. Walls and G. Milburn, *Quantum Optics*, Springer, Heidelberg (1994).

[106] R. E. Slusher, L. W. Hollberg, B. Yurke, J. C. Mertz and J. F. Valley, *Observation of Squeezed States Generated by Four-Wave Mixing in an Optical Cavity*, Phys. Rev. Lett. **55**, 2409 (1985).

[107] H. Vahlbruch, S. Chelkowski, B. Hage, A. Franzen, K. Danzmann and R. Schnabel, *Demonstration of a Squeezed-Light-Enhanced Power- and Signal-Recycled Michelson Interferometer*, Phys. Rev. Lett. **95**, 211102 (2005).

[108] Y. H. Shih and C. O. Alley, *New Type of Einstein-Podolsky-Rosen-Bohm Experiment Using Pairs of Light Quanta Produced by Optical Parametric Down Conversion*, Phys. Rev. Lett. **61**, 2921 (1988).

[109] G. Weihs, T. Jennewein, C. Simon, H. Weinfurter and A. Zeilinger, *Violation of Bell's Inequality under Strict Einstein Locality Conditions*, Phys. Rev. Lett. **81**, 5039 (1998).

[110] J.-W. Pan, M. Daniell, S. Gasparoni, G. Weihs and A. Zeilinger, *Experimental Demonstration of Four-Photon Entanglement and High-Fidelity Teleportation*, Phys. Rev. Lett. **86**, 4435 (2001).

[111] C. Orzel, A. K. Tuchman, M. L. Fenselau, M. Yasuda and M. A. Kasevich, *Squeezed States in a Bose-Einstein Condensate*, Science **291**, 2386 (2001).

[112] J. Estëve, C. Gross, A. Weller, S. Giovanazzi and M. K. Oberthaler, *Squeezing and entanglement in a Bose-Einstein condensate*, Nature **455**, 1216 (2008).

[113] J. Hald, J. L. Sørensen, C. Schori and E. S. Polzik, *Spin Squeezed Atoms: A Macroscopic Entangled Ensemble Created by Light*, Phys. Rev. Lett. **83**, 1319 (1999).

[114] Y. Kawaguchi, H. Saito and M. Ueda, *Einstein–de Haas Effect in Dipolar Bose-Einstein Condensates*, Phys. Rev. Lett. **96**, 080405 (2006).

[115] S. Yi and H. Pu, *Spontaneous Spin Textures in Dipolar Spinor Condensates*, Phys. Rev. Lett. **97**, 020401 (2006).

[116] Y. Kawaguchi, H. Saito and M. Ueda, *Spontaneous Circulation in Ground-State Spinor Dipolar Bose-Einstein Condensates*, Phys. Rev. Lett. **97**, 130404 (2006).

[117] M. A. Baranov, *Theoretical progress in many-body physics with ultracold dipolar gases*, Physics Reports **464**, 71 (2008).

[118] T. Lahaye, C. Menotti, L. Santos, M. Lewenstein and T. Pfau, *The physics of dipolar bosonic quantum gases*, Reports on Progress in Physics **72**, 126401 (2009).

[119] T. Lahaye, T. Koch, B. Fröhlich, M. Fattori, J. Metz, A. Griesmaier, S. Giovanazzi and T. Pfau, *Strong Dipolar Effects in a Quantum Ferrofluid*, Nature **448**, 672 (2007).

[120] T. Koch, T. Lahaye, J. Metz, B. Frölich, A. Griesmaier and T. Pfau, *Stabilization of a purely dipolar quantum gas against collapse*, Nature Physics **4**, 218 (2008).

[121] T. Lahaye, J. Metz, B. Fröhlich, T. Koch, M. Meister, A. Griesmaier, T. Pfau, H. Saito, Y. Kawaguchi and M. Ueda, *d-Wave Collapse and Explosion of a Dipolar Bose-Einstein Condensate*, Phys. Rev. Lett. **101**, 080401 (2008).

[122] J. Metz, T. Lahaye, B. Fröhlich, A. Griesmaier, T. Pfau, H. Saito, Y. Kawaguchi and M. Ueda, *Coherent collapses of dipolar Bose-Einstein condensates for different trap geometries*, New Journal of Physics **11**, 055032 (2009).

[123] J. Stuhler, A. Griesmaier, T. Koch, M. Fattori, T. Pfau, S. Giovanazzi, P. Pedri and L. Santos, *Observation of Dipole-Dipole Interaction in a Degenerate Quantum Gas*, Phys. Rev. Lett. **95**, 150406 (2005).

[124] S. Giovanazzi, P. Pedri, L. Santos, A. Griesmaier, M. Fattori, T. Koch, J. Stuhler and T. Pfau, *Expansion dynamics of a dipolar Bose-Einstein condensate*, Phys. Rev. A **74**, 013621 (2006).

[125] M. Fattori, G. Roati, B. Deissler, C. D'Errico, M. Zaccanti, M. Jona-Lasinio, L. Santos, M. Inguscio and G. Modugno, *Magnetic Dipolar Interaction in a Bose-Einstein Condensate Atomic Interferometer*, Phys. Rev. Lett. **101**, 190405 (2008).

[126] S. E. Pollack, D. Dries, M. Junker, Y. P. Chen, T. A. Corcovilos and R. G. Hulet, *Extreme Tunability of Interactions in a ^7Li Bose-Einstein Condensate*, Phys. Rev. Lett. **102**, 090402 (2009).

[127] M. Vengalattore, S. R. Leslie, J. Guzman and D. M. Stamper-Kurn, *Spontaneously Modulated Spin Textures in a Dipolar Spinor Bose-Einstein Condensate*, Phys. Rev. Lett. **100**, 170403 (2008).

[128] A. Gauguet, B. Canuel, T. Lévèque, W. Chaibi and A. Landragin, *Characterization and limits of a cold-atom Sagnac interferometer*, Phys. Rev. A **80**, 063604 (2009).

[129] T. W. B. Kibble, *Topology of cosmic domains and strings*, Journal of Physics A: Mathematical and General **9**, 1387 (1976).

[130] N. Turok and J. Zadrozny, *Dynamical generation of baryons at the electroweak transition*, Phys. Rev. Lett. **65**, 2331 (1990).

[131] I. Chuang, R. Durrer, N. Turok and B. Yurke, *Cosmology in the Laboratory: Defect Dynamics in Liquid Crystals*, Science **251**, 1336 (1991).

[132] W. H. Zurek, *Cosmological experiments in superfluid helium?*, Nature **317**, 505 (1985).

[133] L. E. Sadler, J. M. Higbie, S. R. Leslie, M. Vengalattore and D. M. Stamper-Kurn, *Spontaneous symmetry breaking in a quenched ferromagnetic spinor Bose-Einstein condensate*, Nature **443**, 312 (2006).

[134] M. Scherer, B. Lücke, G. Gebreyesus, O. Topic, F. Deuretzbacher, W. Ertmer, L. Santos, J. J. Arlt and C. Klempt, *Spontaneous Breaking of Spatial and Spin Symmetry in Spinor Condensates*, Phys. Rev. Lett. **105**, 135302 (2010).

[135] C. C. Gerry and P. L. Knight, *Introductory quantum optics*, Cambridge (2005).

Selbstständigkeitserklärung

Hiermit versichere ich, die vorliegende Doktorarbeit selbstständig und unter ausschließlicher Verwendung der angegebenen Hilfsmittel angefertigt zu haben.

Hannover, den 27. October 2010

Gebremedhn Gebreyesus Hagoss

Acknowledgment

This thesis would not have materialized if it were not for the valuable contribution of a number of people who have supported me through out my PhD journey. The least I can do is to try to express my sincere gratitude in the next few lines.

First and foremost, I would like to express my heartfelt gratitude to my supervisor Prof. Dr. Luis Santos for his excellent supervision, critical comments, unreserved involvement and constant encouragement throughout the course of this work. Luis, you were always so understanding, friendly and patient to listen to all my questions and concerns. Despite your busy schedule, I have never experienced any delay in getting your feedback on any of my questions. You have contributed a great deal to the successful completion of this thesis and I have learned a lot from working with you. For me, you epitomize an excellent supervisor and guide any one can hope for.

My deepest gratitude goes to Dr. Philipp Hyllus and Dr. Frank Deuretzbacher for their valuable discussions, advises and very successful collaborations. I have benefited a lot working with both of you and we had really enjoyable collaborations, "guys, well done!". Frank, I highly appreciate your meticulous reading of this thesis, valuable suggestions and comments. I am also highly indebted to all members of the experimental group of Prof. Dr. Jan Arlt and Prof. Dr. Wolfgang Ertmer for the very successful collaborations. Prof. Dr. Jan Arlt, thank you for taking the time for reviewing my thesis and being examiner. I would also like to thank Dr. Carsten Klempt for his sustained assistance, and discussions of the experimental aspects of my work.

Joining Prof. Luis Santos's group has also given me an opportunity to meet and know many interesting people from whom I have benefited a lot. I have learned a lot concerning latex and numerical simulations from both my office colleagues Karen Rodriguez and Arturo Argüelles. Karen and Arturo, I have always enjoyed your company and I am grateful for the enjoyable time we had together. My special thanks go to Rejish Nath for his valuable discussions and guidance during the first year of my research. I have had fruitful discussions about spinor condensates with Ulrich Ebling. Thank you Urlich for the stimulating discussions. I am grateful to the whole members of our group: Kazimierz Lakomy, Alexander Pikovski, Xiaolong Deng, Mattia Jona Lasinio, Sahbi Aloui for their insightful discussions and pleasant working environment. I would also like to express my gratitude to Catharina Bolz and to the former members of our group: Maria Colomé-Tatché, Michael Klawunn, Andreas Jacob, Giovanni Mazzarella, Nils Bornemann, Jörg Duhme. I enjoyed not only working with you but also for all the joyful moments I shared with you. Thank you Luis and Rocio for inviting me to your house.

Curriculum Vitae

Gebremedhn Gebreyesus Hagoss
Bischofscholer Damm 85, 30173 Hannover, Germany
 Tel.   :   +49 (0)511 762 4836 (office)
            +49(0)17663177626 (mobile)
E-mail: garu.gebreyesus@itp.uni-hannover.de
Homepage: http://www.itp.uni-hannover.de/ garu/

Personal profile

Date of Birth	:	30 December 1975
Place of Birth	:	Adigrat, Ethiopia
Sex	:	Male
Marital Status	:	Single
Nationality	:	Ethiopian
Language	:	English, Amharic, Tigringa

Education

April 2007 to date	PhD candidate, Institute of Theoretical Physics, Leibniz University of Hannover, Hannover, Germany.
2002 - 2004	Master of Science in Physics (Quantum Optics), Addis Ababa University, Addis Ababa, Ethiopia.
1997 - 2001	B. Sc. Physics, Addis Ababa University, Addis Ababa, Ethiopia.
1995 - 1997	Diploma in physics (pre Degree), Bahrdar University, Bahrdar, Ethiopia

Research experience

April 2007 - December 2010		Graduate student at Leibniz University of Hannover, Germany
Thesis Title	:	Parametric Amplification in Spinor Bose-Einstein Condensates.
Advisor	:	Prof. Dr. Luis Santos.
September 2002 - August 2004		Master Thesis at Addis Ababa University, Ethiopia
Thesis Title	:	A three level cascade laser with the cavity mode driven by coherent light and coupled to a squeezed vacuum reserviour.
Advisor	:	Dr. Fesseha Kassahun

Work experience

2004 - 2006	Lecturer at the department of Physics, College of Natural and Computational Sciences, Mekelle University, Ethiopia.
2001 - 2002	Graduate assistant at the department of Physics, College of Natural and Computational Sciences, Mekelle University, Ethiopia.

Responsibilities

2005 - 2006	Academic Programing and Scheduling officer, Mekelle University, Ethiopia.
2004 - 2005	Head of physics department, College of Natural and Computational Sciences, Mekelle University, Ethiopia.

List of Publications

1. M. Scherer, B. Lucke, G. Gebreyesus, O. Topič, F. Deuretzbacher, W. Ertmer, L. Santos, J. J. Arlt, and C. Klempt, *Spontaneous Breaking of Spatial and Spin Symmetry in Spinor Condensates*, Phys. Rev. Lett. **105** 135302 (2010).

2. F. Deuretzbacher, G. Gebreyesus, O. Topič, M. Scherer, B. Lücke, W. Ertmer, J. Arlt, C. Klempt, and L. Santos, *Parametric amplification of matter waves in dipolar spinor Bose-Einstein condensates*, accepted in Phys. Rev. A (2010), arXiv:1005.2011

3. C. Klempt, O. Topič, G. Gebreyesus, M. Scherer, T. Henninger, P. Hyllus, W. Ertmer, L. Santos and J. J. Arlt, *Parametric amplification of vacuum fluctuations in a spinor condensate*, Phys. Rev. Lett. **104**, 195303 (2010).

4. O. Topič, G. Gebreyesus, M. Scherer, T. Henninger, P. Hyllus, C. Klempt, W. Ertmer, L. Santos und J. J. Arlt, *Multi-Resonant Amplification of Quantum Fluctuations in a Spinor Gas*, Las. Phys., **20**, 1-7 (2010)

5. C. Klempt, O. Topič, G. Gebreyesus, M. Scherer, T. Henninger, P. Hyllus, W. Ertmer, L. Santos and J. Arlt, *Multiresonant Spinor Dynamics in a Bose-Einstein Condensate*, Phys. Rev. Lett., **103**, 195302 (2009).